OROGENY-MODIFIED LITHOSPHERE

A Dissertation

presented to

the Faculty of the Graduate School

at the University of Missouri Columbia

In Partial Fulfillment

of the Requirements for the Degree

Doctor of Philosophy

---

by

ASHRAF GAFEER

May 2021

The undersigned, appointed by the dean of the Graduate School, have examined the dissertation entitled

OROGENY-MODIFIED LITHOSPHERE

presented by Ashraf Gafeer,

a candidate for the degree of [doctor of philosophy, and hereby certify that, in their opinion, it is worthy of acceptance.

Professor Martin Appold

Professor Alan Whittington

Professor Hector Lamadrid

Professor Eric Sandvol

Professor Jeff Ferguson

ACKNOWLEDGEMENTS

I would like to thank Dr. Gomez for giving me this opportunity to finish my higher education at the University of Missouri. Also, thanks are extended to my committee chair and members, Martin Appold, Alan Whittington, Hector Lamadrid, Eric Sandvol and for their valuable input, that has greatly enriched and improved this manuscript.

TABLE OF CONTENTS

LIST OF FIGURES

LIST OF TABLES

ABSTRACT

One of the major mantle reservoirs on Earth is the continental lithospheric mantle. Our understanding of the early continental lithosphere sometimes is limited by its subsequent complex history. Continental tracts can be involved in collisional processes that coalesce them into larger masses and obscure their original composition and structure. Depending on the intensity of collisional processes, the continental interiors can be modified by far-field stresses that lead to hot ductile belts and crustal magmatism. The lithospheric mantle according to orogenic peridotites exposed at the surface has primary (peridotites) and cumulated assemblages (pyroxenites). The relationship among the mantle assemblages is detected in subsequent mantle-derived lavas that have interacted with (e.g., plume-induced lavas) or were generated in the lithosphere (e.g., extension-induced lavas) by carrying signatures of mineralogic and isotopic changes from the time of lithosphere modification.

This study examines extruded lavas surrounded by orogenic terrains and the entrained mantle assemblages (xenoliths). The first part shows that asthenospheric derived melt is feasible if the lithosphere has an irregular configuration. The second part of this study examines the temporal changes of the SCLM (sub-continental lithospheric mantle) using mantle xenoliths. New xenolith analyses from the Sahara Craton yield one of the most precise bulk-rock Re-Os isochrons yet reported in peridotitic assemblages. Yielding an exact age in SCLM primary lithology reveals a thermal adjustment event in the SCLM that was synchronized with the cessation of Pan African collisions. The last part of this study presents evidence from five different continents showing that mantle plumes or extensional stresses in the Cenozoic time can trigger or cause the melting of

secondary lithologies of SCLM (Cumulate assemblages, such as pyroxenites). The young lavas convey Re-Os orogenic ages that show that SCLM modifications are syn-orogenic.

INTRODUCTION

The most extensive occurrence of t induced melt is at the Earth's oceanic spreading centers. Whether in the present or the past, to maintain the Earth's shape, continuous melt supply from a mantle acting in a convective system since establishing the plate tectonic system is inevitable. As the ocean floor is continually being created along spreading centers, the equivalent volume is destroyed at subduction zones. At present, the modern oceans make up approximately 65% of the Earth's surface with a maximum age that does not exceed ~200 Ma (Müller et al., 2008). Chronologically, opening and closing ancient oceans is the mechanism for the Earth's continental amalgamations and breakups, where the records are preserved within the orogenic belts and suture zones. The remnants of the Earth's earliest continents are found today on cratons. They are currently distributed across the Earth. As such, Archean-Proterozoic ages are commonly recorded in crustal rocks from cratonic settings. However, due to rheological properties, the subcrustal mantle is completely isolated from the convection effects with refractory and barren characteristics (depleted and buoyant mantle). As an integral part of the continental lithosphere, constraining the lithosphere's stabilization timing and, hence, forming the Earth's earliest subcontinental lithospheric mantle (SCLM) is challenging due to the subsequent thermal-tectonic events imposed through time. Opening oceans and drifting continents where collisional processes coalesce small continents into larger masses (e.g., supercontinent cycles) obscure their original composition and structure. Considering the modifications imposed on the SCLM through time are the key to advancing our knowledge of how the lithosphere has evolved to its

present configuration and fully explain the isotopic signatures measured from the modern-day lithosphere.

Dissertation outlines:

The dissertation highlights the lithospheric mantle assemblages' perspective on the petrogenesis of postorogenic basaltic lavas, linking the time-integrated growth of isotopes measured in mantle assemblages with those sampled by post-orogenic induced melt. The first part (chapter 1) is a case study of Cenozoic lavas in the Sahara Craton, N Africa. The young volcanism's geochemistry shows two distinctive mantle sources. One of which is consistent with SCLM cumulate assemblages (pyroxenites). The other source is consistent with spreading centers induced melt. The second part (chapter 2) addresses the melt removal (depletion) of the SCLM primary assemblages (peridotites) compositionally and chronologically, and the effects of post-depletion enrichment on the time-integrated growth of isotopes. The post-depletion enrichment is evidenced in the future model ages measured from Os isotopic ratios. Peridotitic assemblages from two different cratons reveal evidence of depletion events synchronized with the cessation of continental collisions (orogenies) surrounding the studied samples. The last part (chapter 3) demonstrates the difference between the SCLM primary and secondary assemblages and the time of thermal equilibration among the assemblage-forming minerals. Given the secondary nature of pyroxenites observed in orogenic peridotites, Os derived by postorogenic lavas from five different continents is consistent with pyroxenites-Os systematics. Bounded by the law of radioactivity, the isotopic ratios measured in these young lavas reveal time-integrated growth that corresponds to continental amalgamations (orogenies) surrounding the samples locations.

References

Müller, R.D., Sdrolias, M., Gaina, C., and Roest, W.R., 2008, Age, spreading rates, and spreading asymmetry of the world's ocean crust: Geochemistry, Geophysics, Geosystems, doi:10.1029/2007GC001743.

CHAPTER 1

Petrogenesis of Cenozoic Volcanics in the Sahara Craton from two distinct upper-mantle sources

1.1 Introduction

Volcanic fields that stretch from the Mediterranean coast of Libya to Chad represent the most voluminous outpourings of lava in northern Africa. The most significant volcanic fields, Gharyan, Al Hasawinah, As Sawda, Al Haruj, Waw Namus, Nuqay, and Tibesti (Figure 1.1).

Despite several previous studies (Farahat et al., 2006; Cvetković et al., 2010; Lustrino et al., 2012; Radivojević et al., 2015), there is still a debate about the sources of the lavas and the cause of volcanism. Keppie et al. (2011) suggested that volcanism in the Tibesti-Al Haruj area is caused by a stationary 250 km deep plume that has later fed the Hoggar and Aïr massifs in Algeria through a western corridor at the lithospheric level. Similarly, Gourgaud and Vincent (2004) concluded that lavas in the Tibesti field are most likely derived from a deep-seated plume. On the other hand, an upper mantle source was suggested by Farahat et al. (2006), based on petrographic and mineral compositional data from Al Haruj basaltic rocks. They ascribed the origin of the tholeiitic basalts to a shallow asthenosphere and the origin of alkaline basalts to a deeper asthenosphere that was modified by the Afar mantle plume.

The difficulty in defining the physical identity of the mantle source of the voluminous volcanism in Libya and Chad may be related to the configuration and tectonic history of the Sahara Craton (also known as Sahara Metacraton or Ghost Craton; Black and Liegeois, 1993; Abdelsalam et al., 2002). This chapter demonstrates that the

Sahara Volcanic Line (SVL, Figure 1.1), which includes the Gharyan, Al Hasawinah, As Sawda, Nuqay, and Tibesti fields, and the geochemically distinct Al Haruj field amid this line, originated from two discrete sources, including an enriched lithospheric mantle for the SVL volcanism and asthenosphere for the Al Haruj volcanism. Literature and new geochemical data for these fields provide an opportunity to add new insights on the "bottom topography" of the continental lithosphere and its role in localizing the volcanism in the Cenozoic time.

1.2 Field and age relations

Cenozoic fields of Libya and Chad were generated by episodic outpourings of tholeiitic and alkalic basalts and minor phonolites. Each volcanic field is a geographic entity with various modes of occurrences (plateau lavas, volcanic centers, and plugs; Figure 1.2). Published K/Ar whole-rock ages suggest that the peak in eruptive activity within the SVL and the Al Haruj field was between 8 and 1 Ma ago (Figure 1.3). Without any systematics or correlations with the location, overall, the K/Ar and $^{40}Ar/^{39}Ar$ dates show an overlap in the age of eruption episodes from the NW to the SE Gharyan field (55 to <1 Ma).

1.2.1 Gharyan field (55 to <1 Ma)

The Gharyan field has the oldest lavas, with volcanism lasting more than 50 Ma. Following the eruption of the first plateau lavas and the later volcanic centers, the Gharyan field experienced a younger volcanic episode that has taken place after the establishment of the drainage system in the area. These youngest flows are very distinctive in the field and are described in the literature as "valley basalts" and "young lava series" (Almond et al., 1974); Busrewil and Wadsworth, 1996; Piccoli, 1971). The

age range of this youngest phase, 3 to <1 Ma, is constrained by radiometric dating and by their overlay of Quaternary valley deposits.

1.2.2 Al Hasawinah and As Sawda fields (25 to 10 Ma)

The area occupied by the Al Hasawinah range is dominated by exposures of the Pan-African reworked basement and phonolite ring intrusions (Busrewil and Oun, 1991; Jurak, 1978). The lava flows geographically appear to be an extension of the As Sawda volcanic field rather than forming a separate volcanic center. The As Sawda volcanic field is almost twice the Gharyan field's size, with similar effusive forms of lava flows superimposed by volcanic edifices. The latter are alkalic in composition, while the plateau lavas flows are dominated by tholeiitic basalts (Busrewil and Oun, 1991). However, there is no defined interval in K/Ar ages between them.

1.2.3 Al Haruj and Waw Namus fields (6 to <1 Ma)

Waw Namus is considered to be an active shield volcano. It is located about 100 km south of the main Al Haruj field. The K/Ar ages obtained on two samples from the volcano are 0.200 ± 0.009 Ma and 5.10 ± 0.11 (Bardintzeff et al., 2012). The Al Haruj field is by far the largest in the Sahara Craton, approaching 45,000 km^2 (Klitzsch, 1968). Radiometric age data show that Al Haruj volcanism occurred between 6 and 0.2 Ma, with most flows being younger than 2 Ma. Twenty-two samples from the eastern part of Al Haruj dated with the K/Ar method reveal an age range between 5.4 Ma and 0.5 Ma (Cvetković et al., 2010). Only one sample shows a considerably older age of 11.8 Ma and may be related to older volcanic activities than the main Al Haruj volcanic event (Cvetković et al., 2010). An older volcanic episode within the Al Haruj field is also

supported by an 8.11 ± 0.22 Ma K/Ar age of a lava flow in Waw Namus (Bardintzeff et al., 2012).

1.2.4 Nuqay field (17 to < 1 Ma)

Radivojević et al. (2015) reported forty-four K/Ar ages for the Nuqay field. The age spectrum is very continuous from 17.2 ± 3.0 Ma to 0.97 ±0 .68 Ma without a significant correlation with composition, except that the late central eruption field (referred to as the third phase) is distinctively the most primitive and youngest in the suite with radiometric ages between 3.1 ± 1.1 Ma and 0.97 ± 0.68 Ma.

1.2.5 Tibesti field (~20 to <1 Ma)

The Tibesti field is least known in terms of petrology, and geochemical data for this volcanic field is scarce. However, it also has early flood lavas that are overlain by composite volcanoes. Stratigraphic estimates suggest that the earliest flood basalts erupted in the Early Miocene (Vincent, 1995). Gourgaud and Vincent (2004) provided 1.40 and 1.32 Ma $^{40}Ar/^{39}Ar$ dates for interbedded ignimbrites within large composite volcanoes, which suggest that the last volcanic activity has occurred in the Quaternary period.

1.3 Petrography

Petrographic inspection of the collected samples was primarily done to determine their mineralogy and to determine if there are differences accompanying their modes of occurrence in the field (e.g., plateau lavas vs. shield edifices). The petrographic examination revealed three main mineral assemblages, regardless of the differences in their modes of occurrence (Figure 1.4).

The basalts display variable amounts of olivine, clinopyroxene, plagioclase, and oxides. The olivine vitrophyric texture is the dominant feature. Tiny plagioclase crystallites and glass comprise ~50% of the examined samples. The groundmass shows some gradation into a sub-ophitic texture (pyroxenes that partially envelop plagioclase) and has a large amount of interstitial glass. Plagioclase and pyroxene crystals have subequal sizes. Although clinopyroxene is not a significant phenocryst phase, pale-brown and faintly pleochroic microphenocrysts of clinopyroxene are sporadically found in the slides, while some have relatively large augite crystals.

The phenocryst size variation in the basalts can be depicted from their aphyric to phyric textures. In olivine-phyric basalts, euhedral to subhedral olivine phenocrysts, ranging from 0.5 to 3 mm in diameter and are usually associated with another generation of microphenocrysts ranging from 0.2 to 0.5 mm. Most olivine crystals are completely or partially altered to iddingsite. Plagioclase is the dominant phase in the groundmass with lath-shaped microlites ranging in size from 0.1 to 2 mm. Plagioclase microphenocrysts also occur. They are slightly zoned anhedral crystals.

In correlation with the magmatic series, thin sections from alkalic and tholeiitic lavas show a diversity of textures mainly due to the difference in groundmass relationships. The alkalic lavas tend to have vitrophyric and glassy patches in the groundmass, indicating fast cooling rates. Tholeiites have more developed matrix crystals, mainly laths of plagioclase. There are no nepheline phenocrysts in the studied thin sections but they are reported as a matrix constituent in the most alkali-rich lavas with high MgO 12-14 wt.% (Radivojević et al., 2015).

1.4 Analytical methods

Petrologic and geochemical analyses of the Sahara Cenozoic volcanics have been published in local papers and explanatory booklets sponsored by the Libyan Industrial Research Center. New major and trace elements analyses of samples from the major fields of Gharyan, As Sawda, and Waw Namus, and Al Haruj fields are added, and the results are presented in Table 1.1.

The major and trace element concentrations were obtained by dissolving 100 mg of each sample in trace metal grade HF and HNO_3 acids, 2 ml of each, on a hot plate. After the dissolved samples cooled down, 25 ml of oxalic acid and 15 ml of boric acid were added. Major element abundances were measured using ICP-OES (inductively coupled plasma optical emission spectrometry) at the Department of Geological Sciences, University of Missouri. Trace element and REE concentrations were analyzed by ICP-MS (inductively coupled plasma mass spectrometry) at the University of Missouri Research Reactor.

1.5 Results

Major and trace element compositions of the lavas (compiled from the new and published data) are grouped by fields from the northwest to the southeast in Figures 1.5, 1.6. and 1.7. Nearly all basalts are somewhat undersaturated with respect to SiO_2, but compositions vary widely from nepheline-normative and basanites, mostly in the samples from volcanic centers, to hypersthene and quartz-normative tholeiites in the plateau lavas (Table 1.1), and transitional basalts in the exceptionally large Al Haruj field.

The new and compiled data show that the bulk of SVL lavas has SiO_2 and MgO contents within the ranges 39-52 wt.% and 3-16 wt.%, respectively. Lavas with alkaline

and tholeiitic affinities exist in most of the volcanic fields, displaying almost horizontal trends that cross the alkaline-tholeiitic boundary in total alkalis vs SiO_2 diagrams (Figure 1.5). Lavas from the Al Haruj field fall along the boundary. The Al Haruj lavas have silica contents ranging from 43 to 53 wt.% SiO_2, high $Fe_2O_3^{tot}$ (mostly >12 wt.%), MgO (4-11.4 wt.%), CaO (mostly above 10 wt.%) and TiO_2 (3 wt.%) contents. K_2O is moderately high, reaching values up to 1.9 wt.%. These characteristics are typical for mildly alkaline or transitional basalts.

In general, the SVL alkalic basalts tend to have higher contents of compatible trace elements than tholeiitic basalts. The concentration of Ni in alkaline and tholeiite mixing line ranges between 9–482 ppm. Tholeiites have lower concentrations of incompatible elements (e.g., Rb <10 ppm, Th <2.5 ppm, Nb <21 ppm, La <16 ppm) in comparison with the alkalic basalts that mostly show ranges as follows: Rb=10–81 ppm, Th=2.5–8.4 ppm, Nb=21–89 ppm, and La = 16–66 ppm. On the other hand, trace elements in Al Haruj lavas are relatively uniform with Rb, Th, and La mostly between 5–20 ppm, 1–5 ppm, and 5–18 ppm, respectively. Ratios of La/Yb exhibit a more restricted range in Al Haruj basalts compared to SVL lavas. The La/Yb ratio in the latter is up to 34.

1.6 Discussion

1.6.1 Geochemical characteristics of SVL and Al Haruj lavas

The SVL volcanic fields show enrichment of Rb, Th, Nb, Ta and light REE's over heavy REE's, and Zr in alkalic lavas over tholeiitic lavas (Figures 1.5, 1.6, and 1.7). However, Al Haruj lavas display more elevated, subparallel trend of Zr and Y with other HFS elements relative to SVL lavas, whereas other HFS elements show the same trends

(Figure 1.8). The subparallel trends for SVL and Al Haruj lavas can be linked to retention of Zr and Y by garnet, as the principal Al-bearing mineral in the SVL source, whereas there is less retention by spinel in the Al Haruj source. The partition coefficient (K_d) values of Zr and Y between garnet and melt are three to four orders of magnitudes higher than between spinel and melt (Green et al., 1989; Staudigel et al., 1998; Salters and Longhi, 1999; Klemme et al., 2006; Elkins et al., 2008). Consequently, the subparallel trends suggest that most of the Al Haruj lavas have equilibrated with the mantle at shallower depths than the SVL lavas.

1.6.2 Fractional crystallization

Within each lava series exists ranges in major and trace element compositions (Figures 1.5, 1.6, 1.7, and 1.8) that suggest fractional crystallization has occurred during an ascent of the lavas from sources and after the eruption. Using the most primitive SVL and Al Haruj lavas, fractional crystallization calculations for lithospheric pressure ranges were carried out by the computer program MELTS and for runs at high pressures by pMELTS, as recommended by Ghiorso and Sack (1995) and Ghiorso et al. (2002), respectively. The results are presented in Figure 1.9 and Figure 1.10 for the SVL and Al Haruj suites, respectively.

Fractional crystallization of SVL

Calculated fractionation trajectories that match the observed major element trends of the alkalic and tholeiitic lavas are plotted in Figure 1.9. From the most SVL primitive composition with Mg# [Mg/(Mg+FeO)*100] = 74, the observed major element trends are reproduced by isobaric fractional crystallization at 2 and 8 kbar (and pressures in between) and polybaric crystallization starting at 20 kbar with dP/dT 25 bar/°C. At high P

(20 kbar), clinopyroxene is the liquidus phase. Its crystallization causes the CaO/Al_2O_3 ratio to decrease early in the liquid-line-of-descent. When olivine begins to crystallize, the residual liquid starts to be also depleted in MgO. At isobaric pressures of 2 to 8 kbar, these trends are effectively switched because olivine is the first phase to crystallize, followed by clinopyroxene and plagioclase.

Although the calculated fractionation trajectories for major oxides reproduce well the overall alkaline-tholeiite compositional trends, fractional crystallization is inconsistent with trends of HFS and LIL trace elements of the lavas. These incompatible elements show an overall positive correlation with MgO (Figure 1.9). Lowest Zr, Nd and Ce concentrations on the low-MgO end of the lavas are inconsistent with fractional crystallization, as fractional crystallization should instead lead to elevated concentrations of incompatible elements in residual, low-MgO liquids. Thus, the positive correlations of incompatible trace elements with MgO suggest the production of the lavas from compositionally distinct mantle sources.

Fractional crystallization of Al Haruj field

Samples from Al Haruj exhibit a wide MgO range (4.0 –11.4 wt.%) but relatively limited CaO (8.8–11.9 wt.%) and Al_2O_3 (13.0–16.1 wt.%) ranges, resulting in a CaO/Al_2O_3 range of 0.55 to 0.86 (Figure 1.10). The nearly flat trend of CaO/Al_2O_3 vs. MgO is consistent with fractional crystallization of olivine. The amount of olivine crystallization was, however, not enough to cause significant enrichments in incompatible trace elements that would be expected with more extensive fractional crystallization of olivine

The compositional trends of Al Haruj lavas (Figure 1.10) are best explained by polybaric fractionation of olivine. The early crystallizing phases in pMELTS runs are olivine and clinopyroxene, and the effect of the latter is readily apparent on the CaO/Al_2O_3 ratio (Figure 1.10). The dP/dT trajectory of melt during ascent plays a significant role in determining the liquidus phase. Clinopyroxene is the dominant phase when the dP/dT is relatively low (<55 bar/°C), whereas olivine is the only phase present when dP/dT exceeds 60 bar/°C. The steep gradient required for sole crystallization of olivine over a large depth range is consistent with phase-relation experiments on primitive peridotites by Jaques and Green (1980). The liquidi of clinopyroxene and orthopyroxene above 10 kbar are almost parallel in P-T space with dP/dT gradient of ~60 bar/°C, which explains the lack of clinopyroxene in pMELTS runs with dP/dT > 60 bar/°C. The initial pressure must be at least 30 kbar to reduce MgO from a starting composition having Mg# 69.9 (MgO = 11.4 wt.%; Figure 1.10) by ~7 wt.%. Reduction of MgO from 11.4 to 4 wt.% can only be achieved by fractionation of ~20% of olivine, which requires a dP/dT trajectory of 75 bar/°C and an initial pressure of 30-35 kbar.

These results imply that Al Haruj lavas ascended rapidly with high thermal budgets and without significant cooling. A pMELTS run with dP/dT = 75 bar/°C and 35 kbar initial pressure demonstrates that Al Haruj magmas could have been extracted to the surface from a shallow depth (8.8 kbar pressure domain; Figure 1.10). However, this pressure does not necessarily represent the depth where melting has occurred or the pressure at which the melt last equilibrated with the mantle. It is the minimum pressure that produces 20% fractional crystallization of olivine leaving a liquid with MgO = 3.9 wt.%. Using lower initial pressure values (< 30 kbar) reduces the temperature of the

liquidus and consequently decreases the amount of fractionated olivine. Therefore, Al Haruj lavas could be derived from an upwelling mantle by decompression-melting starting at a pressure of 35 kbar or less. The extracted melt must follow a dP/dT trajectory that is at least 75 bar/°C to prevent the crystallization of clinopyroxene. This trajectory is steeper than the dP/dT trajectory of the upwelling mantle.

1.6.3 Constraining the nature and composition of the mantle sources

The polybaric olivine fractionation trend (Figure 1.10) and relatively elevated Zr and Y (Figure 1.8) imply that the generated melt beneath the Al Haruj field equilibrated with mantle mostly within the spinel stability field, whereas the SVL lavas equilibrated with mantle in the garnet-stability field. This difference is reflected in the REE patterns where lavas generated in the garnet stability field have higher La/Yb ratios. To constrain the composition of the mantle beneath Al Haruj and SVL fields, a quantitative approach is adopted using the equilibrium melting equation of Schilling (1966). During equilibrium batch melting, trace element partitions into melt according to:

$$C_l/C_o = 1/[F + D_r(1 - F)] , \qquad [1]$$

where C_l= element concentration in the partial melt, C_o= initial concentration of the bulk source, D_r= bulk residue-melt distribution coefficient according to the fraction of each of the minerals in the solid residue, and F= weight fraction of melt. Assuming that chemical equilibrium is achieved at the time of removing the melt, the calculated compositions of partial melts are shown in Figure 1.11. The trajectories of the melt compositions are expressed in the ratios of Dy/Yb and La/Yb. The calculated ratios are sensitive to initial concentrations of these elements in the bulk source, since C_o is the denominator in Eq.

[1]. It is important to define the initial trace element concentrations in the bulk source, C_o. For instance, the La/Yb ratio of the Continental Lithospheric Mantle (CLM) of McDonough (1990) is almost ten times that of the Primitive Mantle (PM) of McDonough and Sun (1995, Table 1.2). Because of the contrast of HREE Kd's for garnet relative to spinel, Dy/Yb ratios can be used as indicators of uppermost mantle domains that include spinel and garnet as pressure-dependent phases. On the other hand, La is the most incompatible REE and has the lowest Kd in spinel and garnet (**Error! Reference source not found.**). Thus, both phases have less influence on C_l^{La} .

The assumed source of both for ends of the SVL compositional trend is the Lithospheric Mantle of McDonough (1990). However, the range and values of La/Yb and Dy/Yb ratios of the majority of SVL lavas are too high to be replicated with realistic degrees of melting using the Lithospheric Mantle composition. For the alkalic endmember, the data demand for La to be as high as 4.2 ppm (Figure 1.11a). The tholeiites are best modeled by an increased amount of residual clinopyroxene (> 5%) in the spinel field. Conversely, the alkalic lavas are best modeled by a residue with <5% clinopyroxene within the garnet field. The applied residue modes in Figure 1.11a are consistent with average and median modes of spinel and garnet peridotites reported by McDonough (1990). However, the maximum coverage of REE's of the alkalic lavas occur when the mantle source has a La budget that exceeds that of the Lithospheric Mantle, and vice-versa for the mantle source of the tholeiites.

Although in Al Haruj lavas Dy/Yb ratios are lower than in the SVL lavas (Figure 1.11b), this does not preclude the possibility that the initial stages of partial melting occurred within the garnet stability field, as suggested by pMELTS modeling. The lower

ratios are most likely due to the nature of the mantle beneath the Al Haruj field. Calculations show that the maximum coverage of the ratios can only be attained when the source composition is the Primitive Mantle of McDonough and Sun (1995). It has a subtle contrast between LREE's and HREE's compared to the lithospheric mantle (Table 1.2). For a single pyrolitic residue and considering melting within the upwelling mantle, the model suggests up to 20% melting with decreasing garnet/spinel ratio in the residue.

1.6.4 Primitive and heterogeneous source lithology

The models have several implications for the nature of the Sahara Craton's mantle. First, the SVL mixing end-members suggest a mantle with two different trace element budgets. Second, the CLM peridotitic lithologies (harzburgites <5% cpx and lherzolites >5% cpx) by McDonough (1990) do not justify La concentration measured in the SVL alkalic-tholeiitic mixing line. Lastly, the mantle beneath the Al Haruj field is more homogenous and primitive compared to the SVL source.

Despite the apparently low clinopyroxene modes in the residue of the alkaline end-members of the SVL lavas, the LREE budget of their source must be greater than that of the peridotites of McDonough (1990). Similarly, the average and median modes of high clinopyroxene lherzolites (12%, **Error! Reference source not found.**) cannot explain the La/Yb ratios of the SVL-tholeiites. From this perspective, it can be argued that the mantle cumulates such as pyroxenites played a significant role in their petrogenesis (Yang and Zhou, 2013). As the CLM composition of McDonough (1990) does not account for accumulated assemblages, pyroxenites with an alumina-bearing phase (spinel and garnet) are a common mantle assemblage of the sub-continental lithospheric mantle (Downes, 2007). They occur as layers or dikes within tectonically-

emplaced massifs and also as an integral mantle assemblage brought to the surface among peridotite xenoliths.

Although the origin of pyroxenites in the lithosphere is poorly understood, many studies considered pyroxenites emplacement by crystal precipitation from asthenosphere-derived silicate magmas passing through the lithosphere (e.g., Wilshire and Shervais, 1975; Frey, 1980; Irving, 1980). The contrast in incompatible elements between the SVL sources and the primitive mantle source beneath the Al Haruj field sets apart two different sources that apparently responded differently in terms of melt fractions to the thermal perturbation triggered in the Cenozoic time by extension. The REE systematics of the SVL lavas are in agreement with those in many other extension-related lavas in the circum-Mediterranean region (Figure 1.12; López-Ruiz et al., 1993; Jung and Masberg, 1998; Beccaluva et al., 2007; Bosch et al., 2014). On the other hand, the best example of mantle upwelling where partial melts have equilibrated at shallow depths with the mantle source is oceanic spreading centers (MORB's) where the asthenosphere is considered the source region. The variations of La/Yb and Dy/Yb ratios in Al Haruj lavas are consistent with the ratios in MORB's (Figure 1.12). The Dy/Yb ratio discriminates Al Haruj and MORB's from the SVL lavas and further demonstrates the primitive nature of the Al Haruj source.

From a compositional perspective, pyroxenitic and peridotitic mantle lithologies generally have <30 wt.% and >30 wt.% MgO, respectively (Yang and Zhou, 2013). Although both peridotites and pyroxenites can experimentally produce basaltic magmas, their compositional characteristics are different. Figure 1.13 presents melting experiments on a variety of peridotite and pyroxenite assemblages within a pressure range between

1.5 to 6.0 GPa. The major element parameterization of peridotite melts cannot explain the counterpart values of the SVL and Al Haruj lavas. Particularly, melts produced from pyroxenites have lower MgO contents, higher Al_2O_3 contents, and higher SiO_2/MgO ratios than melts produced from peridotites. The compositions of experimental melts produced from pyroxenites correspond to compositions of the SVL volcanics.

1.7 Conclusion

Amid the SVL line, the exceptionally large Al Haruj field has lava flows that are morphologically different from the other volcanic fields. It could be owed to the fluidity of high-temperature lavas generated by convective upwelling of the asthenospheric mantle below a very thin lithosphere. The range of lava compositions in the field can be described by the high-pressure fractionation of olivine as the partial melts ascended in the upwelling asthenosphere. The petrogenesis of the SVL lavas might suggest the involvement of mantle cumulates of secondary nature such as pyroxenites. Given the tectonic nature of the Sahara Craton, the presence of two distinctive source lithologies within the same Cenozoic time frame could be related to the lithospheric configuration and/or modification during the Pan African Orogeny.

References

A. Brown, W., I. Doser, D., Keller, R., 2003. An Integrated Geophysical study of the Lithospheric Structure Beneath Libya, AGU Fall Meeting Abstracts.

Abdelsalam, M.G., Liégeois, J.P., Stern, R.J., 2002. The Saharan Metacraton. J. African Earth Sci. 34, 119–136. https://doi.org/10.1016/S0899-5362(02)00013-1

Almond, D.C., Busrewil, M.T., Wadsworth, W.J., 1974. The Gharian Tertiary volcanic province of Tripoltania, Libya. Geol. J. 9, 17–28.

Arevalo, R., McDonough, W.F., 2010. Chemical variations and regional diversity observed in MORB. Chem. Geol. 271, 70–85. https://doi.org/10.1016/j.chemgeo.2009.12.013

Bardintzeff, J.M., Deniel, C., Guillou, H., Platevoet, B., Télouk, P., Oun, K.M., 2012. Miocene to recent alkaline volcanism between Al Haruj and Waw an Namous (southern Libya). Int. J. Earth Sci. 101, 1047–1063. https://doi.org/10.1007/s00531-011-0708-5

Beccaluva, L., Bianchini, G., Bonadiman, C., Coltorti, M., Milani, L., Salvini, L., Siena, F., Tassinari, R., 2007. Intraplate lithospheric and sublithospheric components in the Adriatic domain: Nephelinite to tholeiite magma generation in the Paleogene Veneto volcanic province, southern Alps, in: Beccaluva, L., Bianchini, G., Wilson, M. (Eds.), Cenozoic Volcanism in the Mediterranean Area. pp. 131–152. https://doi.org/10.1130/2007.2418(07)

Beccaluva, L., Bianchini, G., Ellam, R.M., Marzola, M., Oun, K.M., Siena, F., Stuart, F.M., 2008. The role of HIMU metasomatic components in the North African lithospheric mantle: petrological evidence from the Gharyan lherzolite xenoliths, NW Libya. Geol. Soc. London, Spec. Publ. 293, 253–277. https://doi.org/10.1144/SP293.12

Black, R., Liegeois, J.-P., 1993. Cratons, mobile belts, alkaline rocks and continental lithospheric mantle: the Pan-African testimony. J. Geol. Soc. London. 150, 89–98. https://doi.org/10.1144/gsjgs.150.1.0088

Bosch, D., Maury, R.C., El Azzouzi, M., Bollinger, C., Bellon, H., Verdoux, P., 2014. Lithospheric origin for Neogene-Quaternary Middle Atlas lavas (Morocco): Clues from trace elements and Sr-Nd-Pb-Hf isotopes. Lithos 205, 247–265. https://doi.org/10.1016/j.lithos.2014.07.009

Busrewil, M.., Oun, K.M., 1991. Geochemistry of the Tertiary alkaline rocks of jabal al Hasawinah, west central Libya. Geol. Libya VII, 2587–2598.

Busrewil, M.., Wadsworth, W.J., 1996. Tertiary-Quaternary alkaline-subalkaline magmatism in Gharyan area-Field aspects and petrography. Acad. Press PRJ 8, 13–23.

Busrewil, M.T., Esson, J., 1991. Chronology and composition of the igneous rocks of Jabal as Sawda. Geol. Libya 7, 2599–2603.

Cvetković, V., Toljić, M., Ammar, N.A., Rundić, L., Trish, K.B., 2010. Petrogenesis of the eastern part of the Al Haruj basalts (Libya). J. African Earth Sci. 58, 37–50. https://doi.org/10.1016/j.jafrearsci.2010.01.006

Davis, F.A., Hirschmann, M.M., Humayun, M., 2011. The composition of the incipient partial melt of garnet peridotite at 3GPa and the origin of OIB. Earth Planet. Sci. Lett. https://doi.org/10.1016/j.epsl.2011.06.008

Downes, H., 2007. Origin and significance of spinel and garnet pyroxenites in the shallow lithospheric mantle: Ultramafic massifs in orogenic belts in Western Europe and NW Africa. Lithos. https://doi.org/10.1016/j.lithos.2007.05.006

Elkins, L.J., Gaetani, G.A., Sims, K.W.W., 2008. Partitioning of U and Th during garnet pyroxenite partial melting: Constraints on the source of alkaline ocean island basalts. Earth Planet. Sci. Lett. 265, 270–286. https://doi.org/10.1016/j.epsl.2007.10.034

Emry, E.L., Shen, Y., Nyblade, A.A., Flinders, A., Bao, X., 2019. Upper Mantle Earth Structure in Africa From Full-Wave Ambient Noise Tomography. Geochemistry, Geophys. Geosystems 20, 120–147.

Falloon, T.J., Danyushevsky, L. V, 2000. Melting of Refractory Mantle at 1·5, 2 and 2·5 GPa under Anhydrous and H2O-undersaturated Conditions: Implications for the Petrogenesis of High-Ca Boninites and the Influence of Subduction Components on Mantle Melting. J. Petrol. 41, 257–283. https://doi.org/10.1093/petrology/41.2.257

Falloon, T.J., Green, D.H., Hatton, C.J., Harris, K.L., 1988. Anhydrous partial melting of a fertile and depleted peridotite from 2 to 30 kb and application to basalt petrogenesis. J. Petrol. https://doi.org/10.1093/petrology/29.6.1257

Farahat, E.S., Ghani, M.S.A., Aboazom, A.S., Asran, A.M.H., 2006. Mineral chemistry of Al Haruj low-volcanicity rift basalts, Libya: Implications for petrogenetic and geotectonic evolution. J. African Earth Sci. 45, 198–212. https://doi.org/10.1016/j.jafrearsci.2006.02.007

Frey, F., 1980. The origin of pyroxenites and garnet pyroxenites from Salt Lake Crater, Oahu, Hawaii: trace element evidence. Am. J. Sci.

Ghiorso, M.S., Hirschmann, M.M., Reiners, P.W., Kress, V.C., 2002. The pMELTS: A revision of MELTS for improved calculation of phase relations and major element partitioning related to partial melting of the mantle to 3 GPa. Geochemistry Geophys. Geosystems 3, 36. https://doi.org/10.1029/2001gc000217

Ghiorso, M.S., Sack, R.O., 1995. Chemical mass transfer in magmatic processes IV. A revised and internally consistent thermodynamic model for the interpolation and extrapolation of liquid-solid equilibria in magmatic systems at elevated temperatures and pressures. Contrib. to Mineral. Petrol. 119, 197–212. https://doi.org/10.1007/BF00307281

Goudarzi, G.H., Smith, J.P., 1978. Preliminary structure-contour map of the Libyan Arab Republic and adjacent areas.

Gourgaud, A., Vincent, P.M., 2004. Petrology of two continental alkaline intraplate series at Emi Koussi volcano, Tibesti, Chad. J. Volcanol. Geotherm. Res. 129, 261–290. https://doi.org/10.1016/S0377-0273(03)00277-4

Green, T.H., Blundy, J.D., Adam, J., Yaxley, G.M., 2000. SIMS determination of trace element partition coefficients between garnet, clinopyroxene and hydrous basaltic liquids at 2-7.5 GPa and 1080-1200°C. Lithos 53, 165–187. https://doi.org/10.1016/S0024-4937(00)00023-2

Green, T.H., Sie, S.H., Ryan, C.G., Cousens, D.R., 1989. Proton microprobe-determined partitioning of Nb, Ta, Zr, Sr and Y between garnet, clinopyroxene and basaltic magma at high pressure and temperature. Chem. Geol. 74, 201–216. https://doi.org/10.1016/0009-2541(89)90032-6

Irvine, T.N., Baragar, W.R. a., 1971. A Guide to the Chemical Classification of the Common Volcanic Rocks. Can. J. Earth Sci. 8, 523–548. https://doi.org/10.1139/e71-055

Irving, A., 1980. Petrology and geochemistry of composite ultramafic xenoliths in alkalic basalts and implications for magmatic processes within the mantle. Am. J. Sci.

Jaques, A.L., Green, D.H., 1980. Anhydrous melting of peridotite at 0-15 Kb pressure and the genesis of tholeiitic basalts. Contrib. to Mineral. Petrol. 73, 287–310. https://doi.org/10.1007/BF00381447

Jung, S., Masberg, P., 1998. Major- and trace-element systematics and isotope geochemistry of Cenozoic mafic volcanic rocks from the Vogelsberg (central Germany). J. Volcanol. Geotherm. Res. 86, 151–177. https://doi.org/10.1016/S0377-0273(98)00087-0

Jurak, I., 1978. Sheet Jabal al Hasawna NH 33-14, Geological Map of Libya, scale 1: 250000, Explanatory Booklet. Ind. Res. Center, Triboli.

Keppie, J.D., Dostal, J., Murphy, J.B., 2011. Complex geometry of the Cenozoic magma plumbing system in the central Sahara, NW Africa. Int. Geol. Rev. 53, 1576–1592. https://doi.org/10.1080/00206814.2010.496211

Klemme, S., Günther, D., Hametner, K., Prowatke, S., Zack, T., 2006. The partitioning of trace elements between ilmenite, ulvospinel, armalcolite and silicate melts with implications for the early differentiation of the moon. Chem. Geol. 234, 251–263. https://doi.org/10.1016/j.chemgeo.2006.05.005

Klitzsch, E., 1968. Der Basaltvulkanismus des Djebel Haroudj Ostfezzan/Libyen. Geol. Rundschau 57, 585–601. https://doi.org/10.1007/BF01821263

Kogiso, T., Hirose, K., Takahashi, E., 1998. Melting experiments on homogeneous mixtures of peridotite and basalt: Application to the genesis of ocean island basalts. Earth Planet. Sci. Lett. https://doi.org/10.1016/S0012-821X(98)00156-3

Lambart, S., Laporte, D., Provost, A., Schiano, P., 2012. Fate of pyroxenite-derived melts in the peridotitic mantle: Thermodynamic and experimental constraints. J. Petrol. https://doi.org/10.1093/petrology/egr068

Lambart, S., Laporte, D., Schiano, P., 2013. Markers of the pyroxenite contribution in the major-element compositions of oceanic basalts: Review of the experimental constraints. Lithos. https://doi.org/10.1016/j.lithos.2012.11.018

Lambart, S., Laporte, D., Schiano, P., 2009. An experimental study of pyroxenite partial melts at 1 and 1.5 GPa: Implications for the major-element composition of Mid-Ocean Ridge Basalts. Earth Planet. Sci. Lett. https://doi.org/10.1016/j.epsl.2009.09.038

Le Heron, D.P., Howard, J., 2010. Evidence for Late Ordovician glaciation of Al Kufrah Basin, Libya. J. African Earth Sci. 58, 354–364. https://doi.org/10.1016/j.jafrearsci.2010.04.001

Leighton, M.W., Eidel, J.J., Kolata, D.R., Oltz, D.F., 1990. Geology of interior cratonic sag basins. AAPG Bull. (American Assoc. Pet. Geol. 74.

López-Ruiz, J., Cebriá, J.M., Doblas, M., Oyarzun, R., Hoyos, M., Martín, C., 1993. Cenozoic intra-plate volcanism related to extensional tectonics at Calatrava, central Iberia: Geological Society of London Journal, v. 150. doi 10, 915–922.

Lüning, S., Craig, J., Fitches, B., Mayouf, J., Busrewil, A., Dieb, M. El, Gammudi, A., Loydell, D., McIlroy, D., 1999. Re-evaluation of the petroleum potential of the Kufra Basin (SE Libya, ne Chad): does the source rock barrier fall? Mar. Pet. Geol. 16, 693–718. https://doi.org/10.1016/S0264-8172(99)00013-6

Lustrino, M., Cucciniello, C., Melluso, L., Tassinari, C.C.G., dè Gennaro, R., Serracino, M., 2012. Petrogenesis of Cenozoic volcanic rocks in the NW sector of the Gharyan volcanic field, Libya. Lithos 155, 218–235. https://doi.org/10.1016/j.lithos.2012.09.003

Lustrino, M., Melluso, L., Morra, V., 2002. The transition from alkaline to tholeiitic magmas: A case study from the Orosei-Dorgali Pliocene volcanic district (NE Sardinia, Italy). Lithos 63, 83–113. https://doi.org/10.1016/S0024-4937(02)00113-5

Macgregor, D.S., 1996. The hydrocarbon systems of North Africa. Mar. Pet. Geol. 13, 329–340. https://doi.org/10.1016/0264-8172(95)00068-2

Mayer, B., Jung, S., Romer, R.L., Stracke, A., Haase, K.M., Garbe-Schönberg, C.D., 2013. Petrogenesis of tertiary hornblende-bearing lavas in the rhön, germany. J. Petrol. 54, 2095–2123. https://doi.org/10.1093/petrology/egt042

McDonough, W.F., 1990. Constraints on the composition of the continental lithospheric mantle. Earth Planet. Sci. Lett. 101, 1–18. https://doi.org/10.1016/0012-821X(90)90119-I

McDonough, W.F., Sun, S. s., 1995. The composition of the Earth. Chem. Geol. 120, 223–253. https://doi.org/10.1016/0009-2541(94)00140-4

Mckenzie, D., O'nions, R.K., 1991. Partial melt distributions from inversion of rare earth element concentrations. J. Petrol. 32, 1021–1091. https://doi.org/10.1093/petrology/32.5.1021

Miller, C., Zanetti, A., Thöni, M., Konzett, J., Klötzli, U., 2012. Mafic and silica-rich glasses in mantle xenoliths from Wau-en-Namus, Libya: Textural and geochemical evidence for peridotite-melt reactions. Lithos 128–131, 11–26. https://doi.org/10.1016/j.lithos.2011.11.004

Piccoli, G., 1971. Outlines of volcanism in northern Tripolitania, in: Gray, C. (Ed.), First Symposium on Geology of Libya, Faculty of Science, University of Libya. Tripoli, pp. 323–332.

Radivojević, M., Toljić, M., Turki, S.M., Bojić, Z., Šarić, K., Cvetković, V., 2015. Neogene to Quaternary basalts of the Jabal Eghei (Nuqay) area (south Libya): Two distinct volcanic events or continuous volcanism with gradual shift in magma composition? J. Volcanol. Geotherm. Res. 293, 57–74. https://doi.org/10.1016/j.jvolgeores.2015.02.003

Salters, V.J.M., Longhi, J., 1999. Trace element partitioning during the initial stages of melting beneath mid-ocean ridges. Earth Planet. Sci. Lett. 166, 15–30. https://doi.org/10.1016/S0012-821X(98)00271-4

Schandelmeier, H., 1988. Pre-Cretaceous intraplate basins of NE Africa. Episodes 11, 270–274.

Schilling, J.-G.E., 1966. Rare earth fractionation in Hawaiian volcanic rocks.

Schult, A., Soffel, H., 1973. Palaeomagnetism of Tertiary Basalts from Libya. Geophys. J. Int. 32, 373–380. https://doi.org/10.1111/j.1365-246X.1973.tb05837.x

Staudigel, H., Albarède, F., Blichert-Toft, J., Edmond, J., McDonough, B., Jacobsen, S.B., Keeling, R., Langmuir, C.H., Nielsen, R.L., Plank, T., Rudnick, R., Shaw, H.F., Shirey, S., Veizer, J., White, W., 1998. Geochemical Earth Reference Model (GERM): description of the initiative. Chem. Geol. 145, 153–159. https://doi.org/10.1016/S0009-2541(97)00141-1

Underdown, R., Redfern, J., 2008. Petroleum generation and migration in the Ghadames Basin, north Africa: A two-dimensional basin-modeling study. Am. Assoc. Pet. Geol. Bull. 92, 53–76. https://doi.org/10.1306/08130706032

Vincent, P.., 1995. Volcanisme tertiaire et quaternaire, in: Beauvilain, A. (Ed.), Géologie, Ressources Minérales et Ressources En Eau Du Tchad, 2 Éme Édition Par Kusnir I, Collab. Schneider, J.L. et Vincent, P.M. CNAR, N'Djaména, pp. 67–80.

Walter, M.J., 1998. Melting of garnet peridotite and the origin of komatiite and depleted lithosphere. J. Petrol. 39, 29–60. https://doi.org/10.1093/petrology/39.1.29

Wilshire, H.G., Shervais, J.W., 1975. Al-augite and Cr-diopside ultramafic xenoliths in basaltic rocks from western United States. Phys. Chem. Earth. https://doi.org/10.1016/0079-1946(75)90021-X

Yang, Z.F., Zhou, J.H., 2013. Can we identify source lithology of basalt? Sci. Rep. 3. https://doi.org/10.1038/srep01856

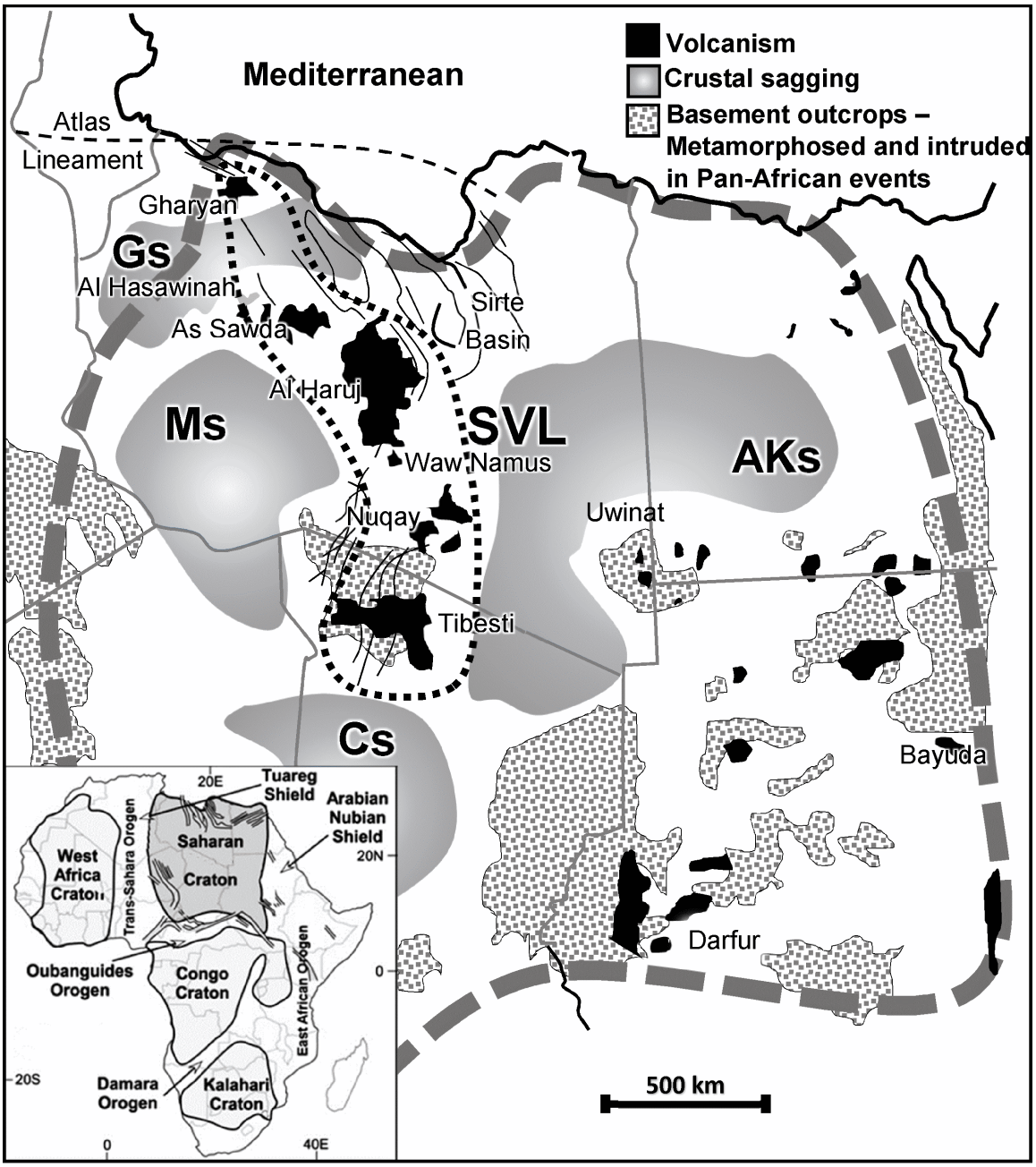

Figure 1.1 Schematic map showing the Sahara major volcanic fields surrounded by sag sedimentary basins and basement outcrops. The thick stippled line outlines the volcanism in Libya and Chad discussed in this chapter. Abbreviations are as follows: SVL= Sahara Volcanic Line. AKs: Al Kufrah sag basin. Cs: Chad sag basin. Gs: Ghadamis sag basin. Ms: Murzuq sag basin.

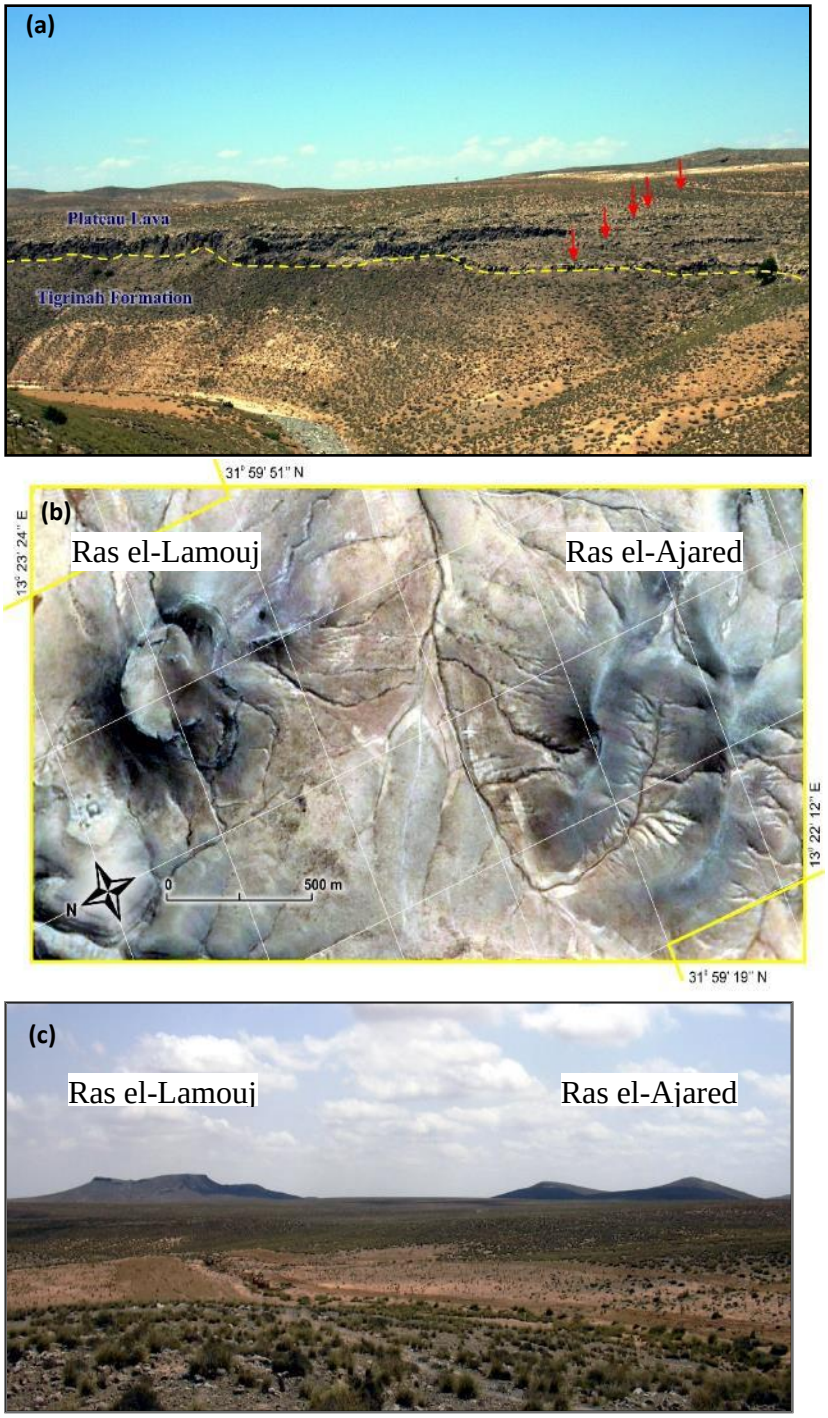

Figure 1.2 Morphology of the Sahara volcanic fields. **a)** General view of a stack of basaltic lava flows unconformably overlying the Mesozoic sedimentary rocks in the Gharyan field. **b-c)** Shield style of basaltic lava with a pit or fissure-crater effusion in the Gharyan field.

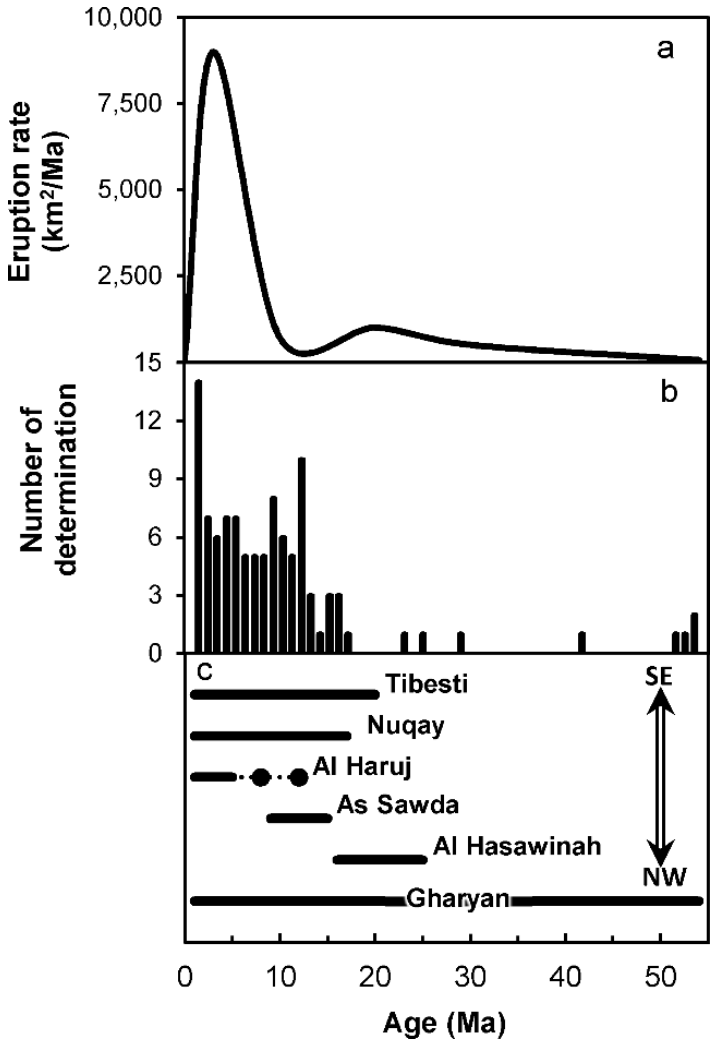

Figure 1.3 Age distribution for Sahara volcanic fields. **a)** Time-averaged eruption rate of SVL and Al Haruj basalts as a function of time. **b)** A histogram showing the age distribution of basaltic rocks with ages <55 Ma. **c)** Measured ages for individual fields from Schult and Soffel (1973), Jurak (1978), Busrewil and Esson (1991), Busrewil and Wadsworth (1996), Cvetković et al. (2010), Bardintzeff et al. (2012), Radivojević et al. (2015).

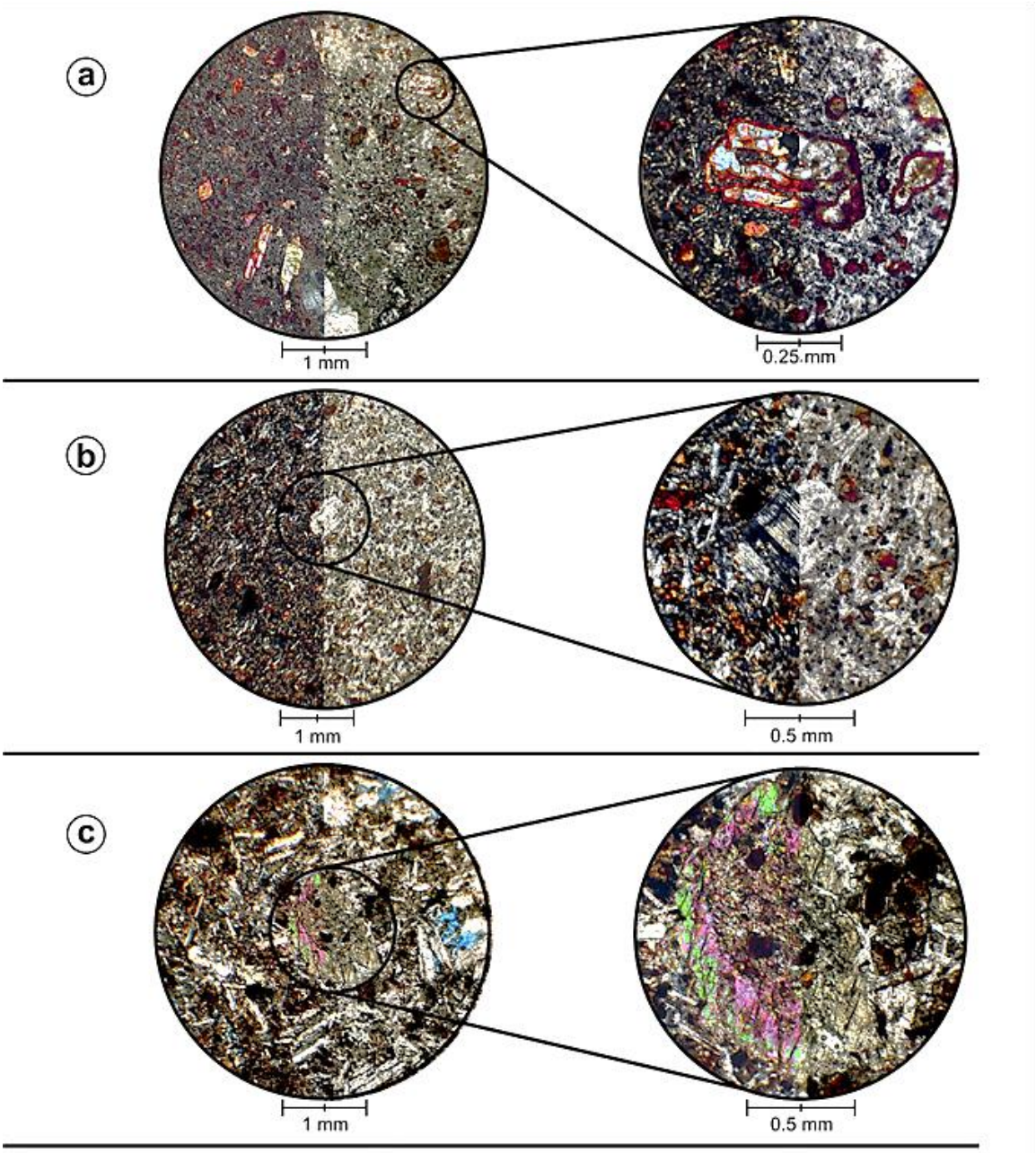

Figure 1.4 Photomicrographs of the SVL basalts with the fields of view split into two halves, left half in XPL and right half in PPL: **a)** Olivine basalt with partly iddingsite alteration of olivine phenocrysts and a calcitic amygdule at the bottom. Magnified inset shows a skeletal olivine microphenocryst trapping the melt indicating rapid growth. **b)** Olivine basalt with two generations of plagioclase, interstitial laths and microphenocrysts. Magnified inset shows zoned plagioclase crystal twinned on Carlsbad law. **c)** Olivine basalt with sub-ophitic texture. The pale brown-green clinopyroxene partly enveloping plagioclase laths. Magnified inset shows a clinopyroxene crystal. The innermost zone encloses small crystals (probably an earlier generation of clinopyroxene) and some lath-shaped plagioclase, and the outermost zone of the crystal has a composition zoning as shown by the difference in the interference colors between the main part of the crystal and the rims.

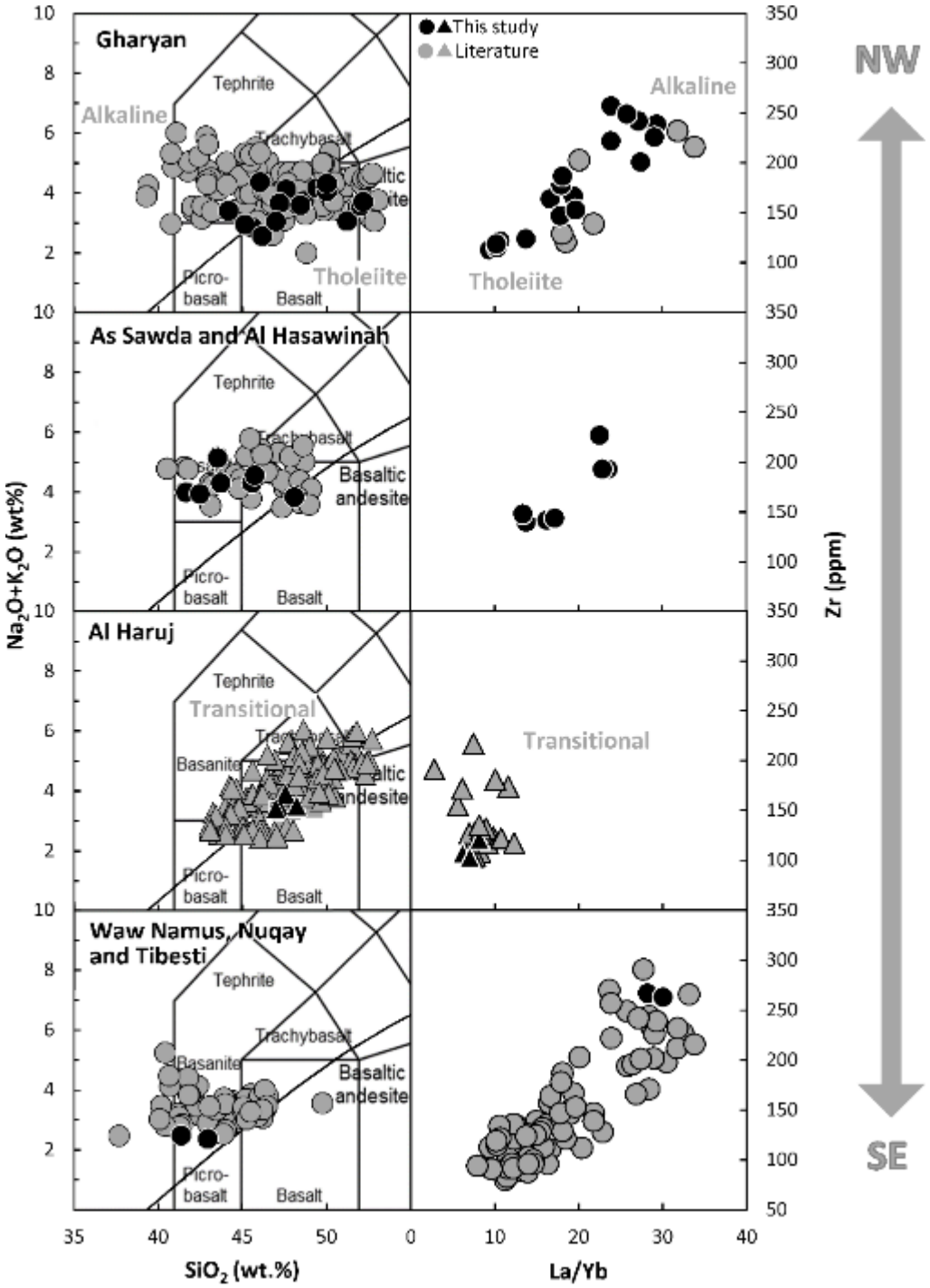

Figure 1.5 Major and trace element geochemistry of volcanic fields in Libya and Chad. Data collected for the present study are shown by black symbols. Additional basaltic data from recent studies are also included (Gourgaud and Vincent, 2004; Beccaluva et al., 2008; Cvetković et al., 2010; Bardintzeff et al., 2012; Lustrino et al., 2012; Radivojević et al., 2015). The dividing line between alkaline and tholeiitic compositions is from Irvine and Baragar (1971).

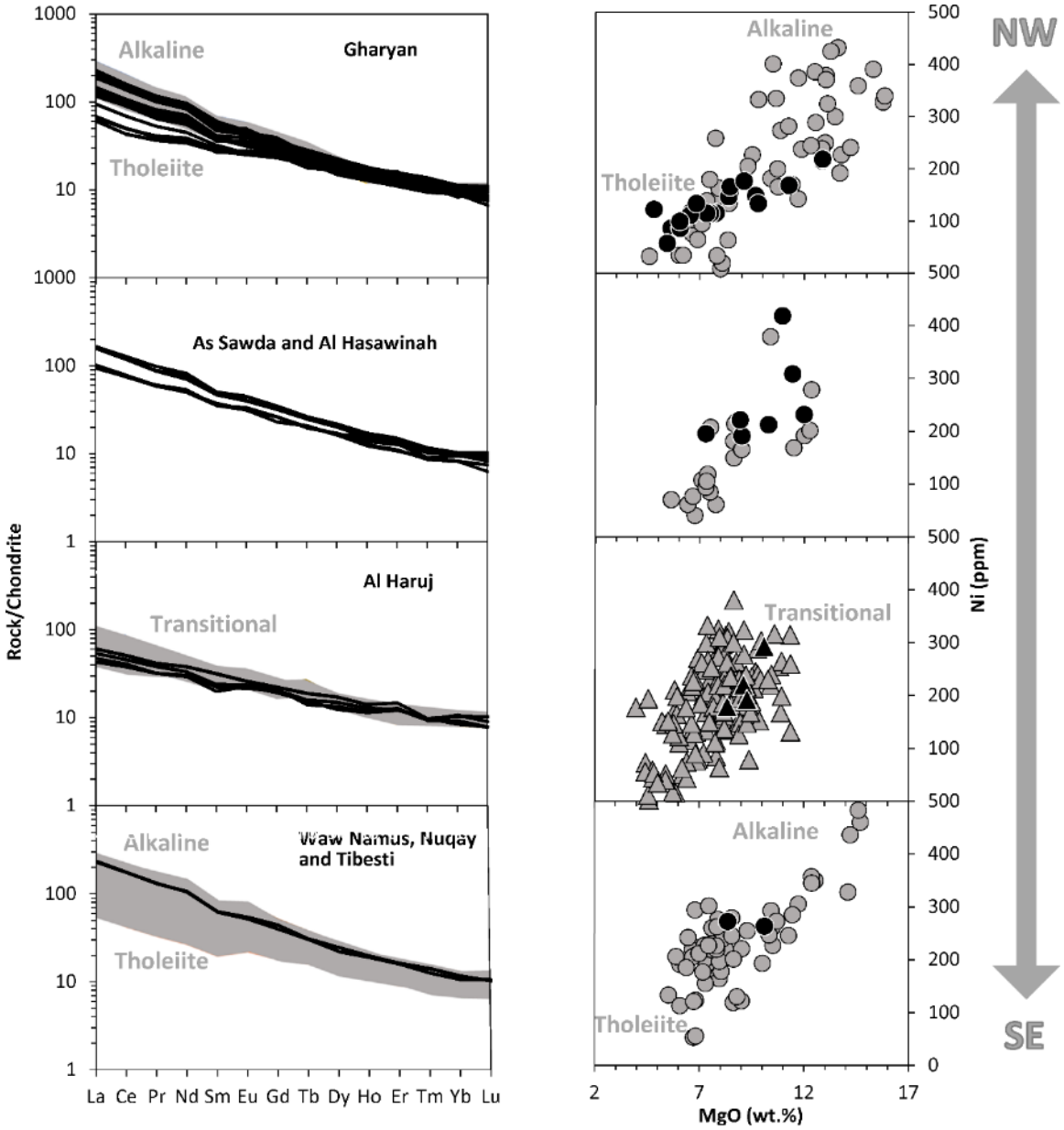

Figure 1.6 Chondrite-normalized basalts REE (coefficients of normalization after McDonough and Sun, 1995) and MgO (wt.%) vs. Ni (ppm) diagrams of volcanic fields in Libya and Chad. Data and symbols as in Figure 1.5.

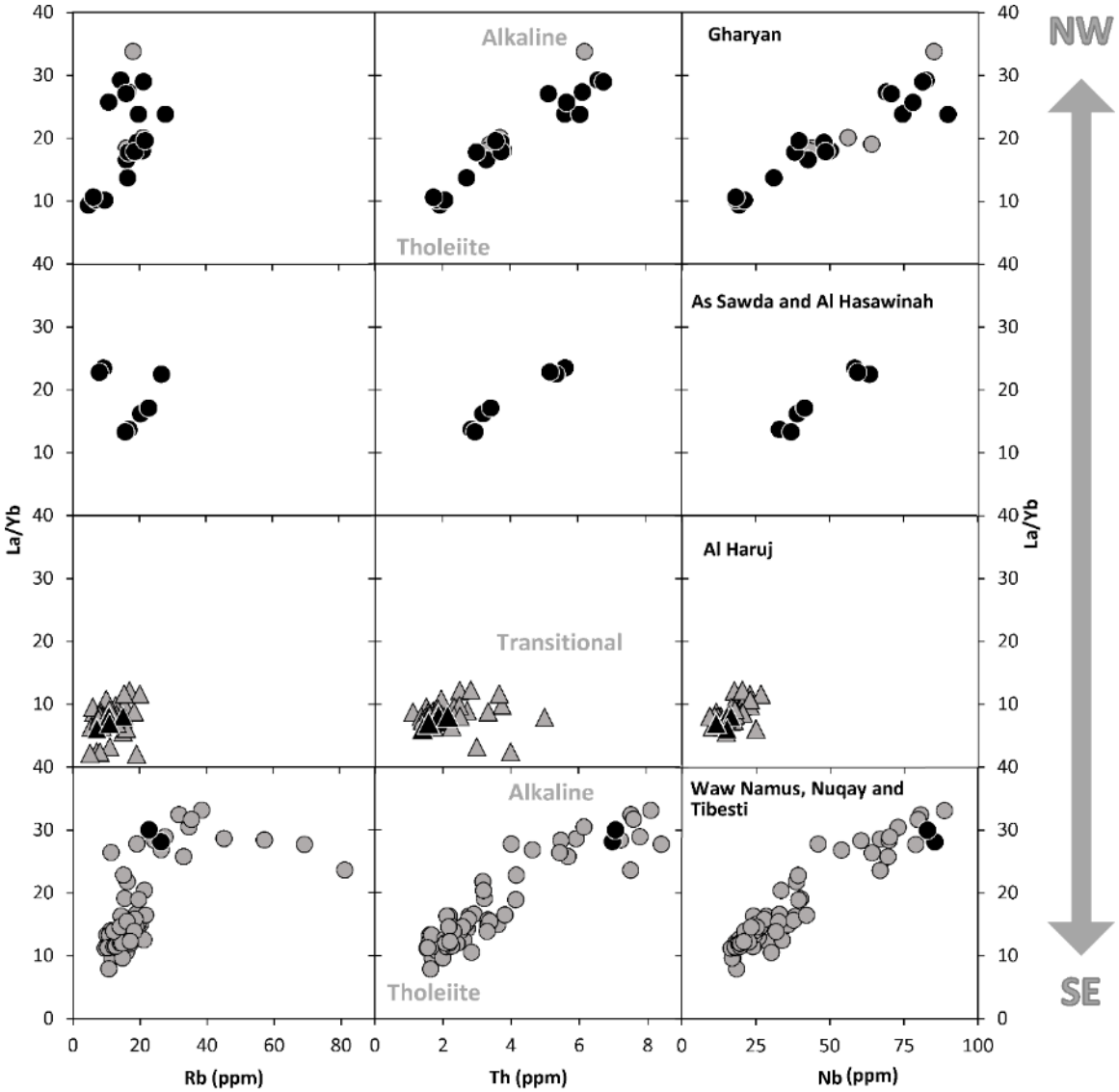

Figure 1.7 Light-Heavy REE ratio vs incompatible elements concentration diagrams of volcanic fields in Libya and Chad. Data and symbols as in Figure 1.5.

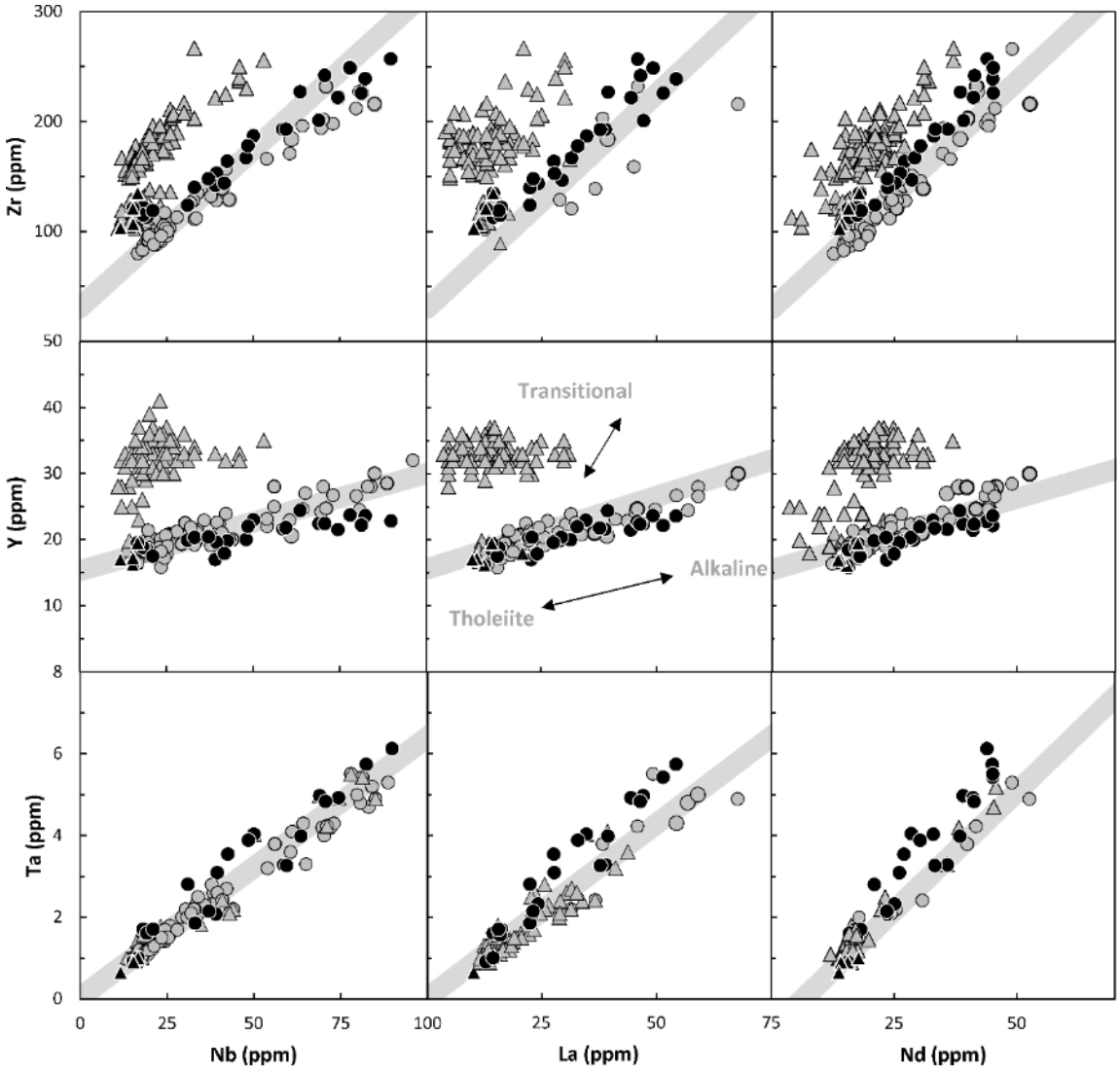

Figure 1.8 Diagrams showing correlation trends of key high field-strength (HFS) elements in SVL and Al Haruj lavas.

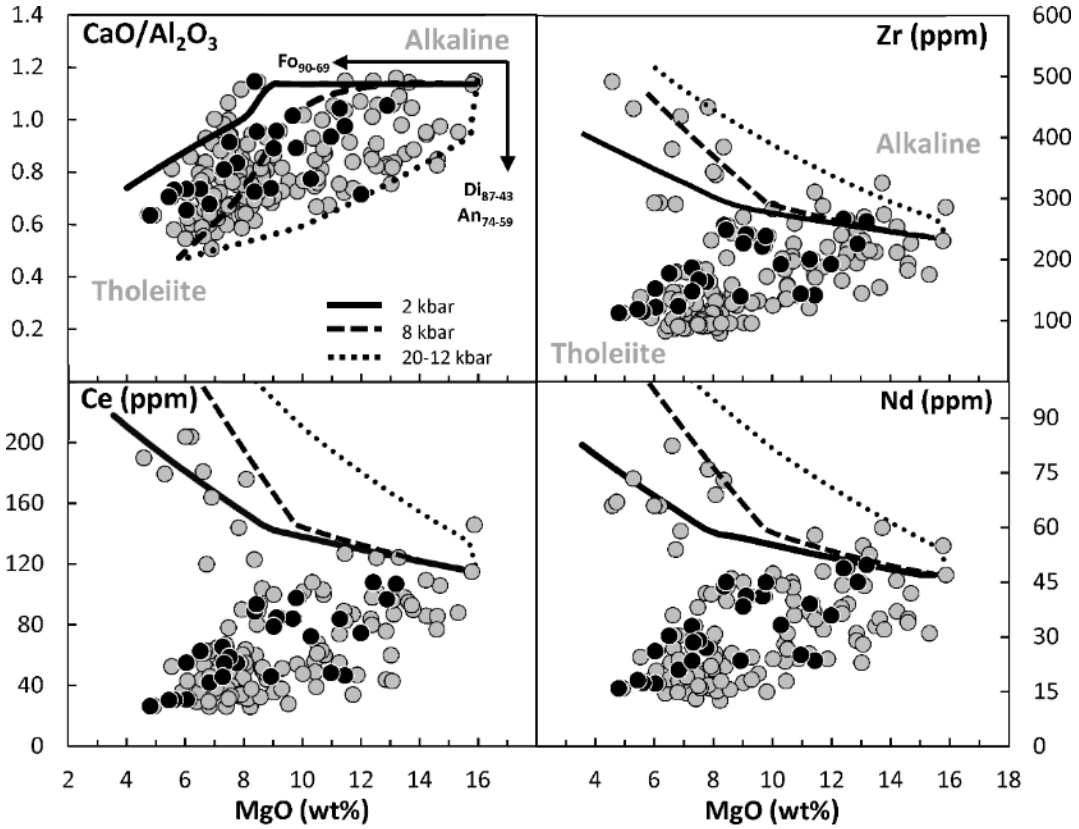

Figure 1.9 Plots of CaO/Al_2O_3 (wt.% ratio) and trace elements vs MgO trends in SVL lavas. Lines show model fractional crystallization trends as computed by the program MELTS. The different trends are controlled by pressure effects on the sequence of mineral crystallization. At low isobaric pressures (2 and 8 kbar), the sequence is olivine (Fo_{90-69})-clinopyroxene (Di_{87-79})-plagioclase (An_{74-59}) and at high polybaric pressures (20-12 kbar) the sequence is clinopyroxene (Di_{52-43})-olivine (Fo_{86-83}). Trace elements partition coefficients for the fractionating phases are from McKenzie and O'Nions (1991). The figure shows that although some major element trends are consistent fractional crystallization, trace element trends of the tholeiites are not.

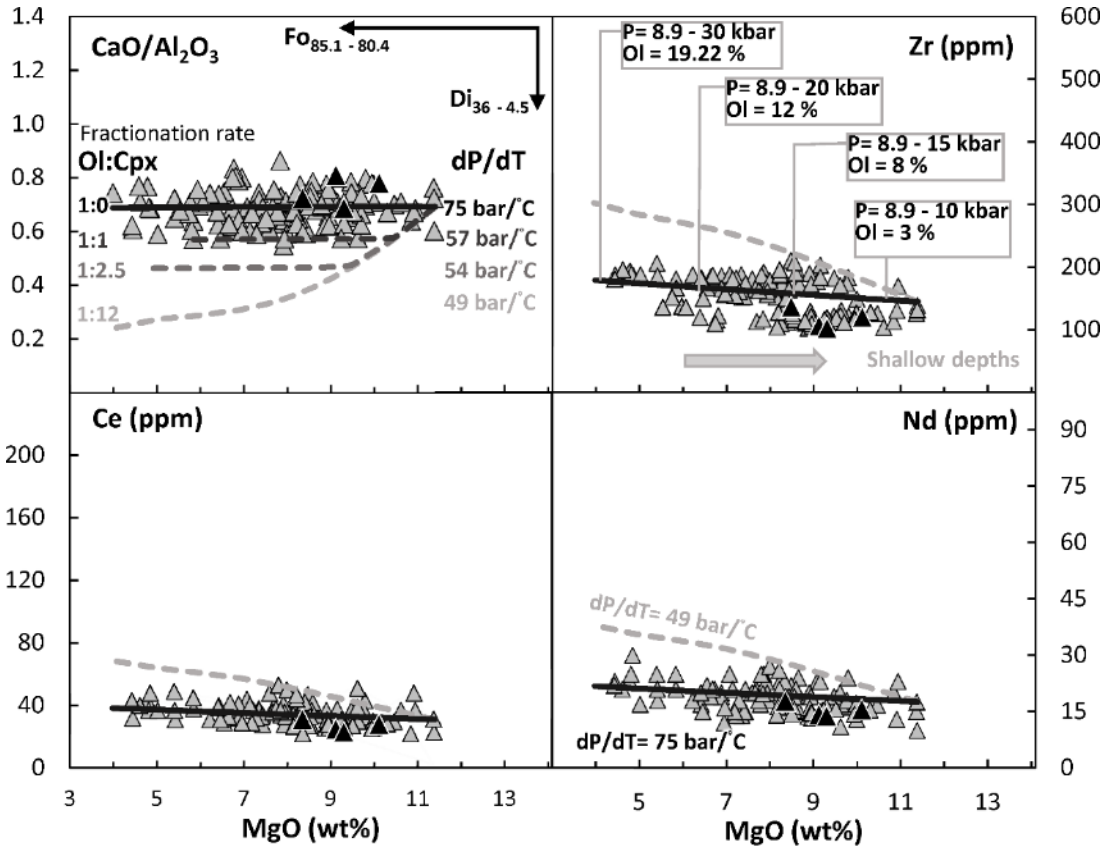

Figure 1.10 Plots of CaO/Al_2O_3 (wt.% ratio) and trace elements vs MgO trends in Al Haruj lavas. Lines show model fractional crystallization trends as computed by the program pMELTS. As explained in the text, the most evolved, low MgO compositions require polybaric crystallization of olivine at high dP/dT trajectories. High MgO lavas require lower initial pressure to account for less olivine fractionation.

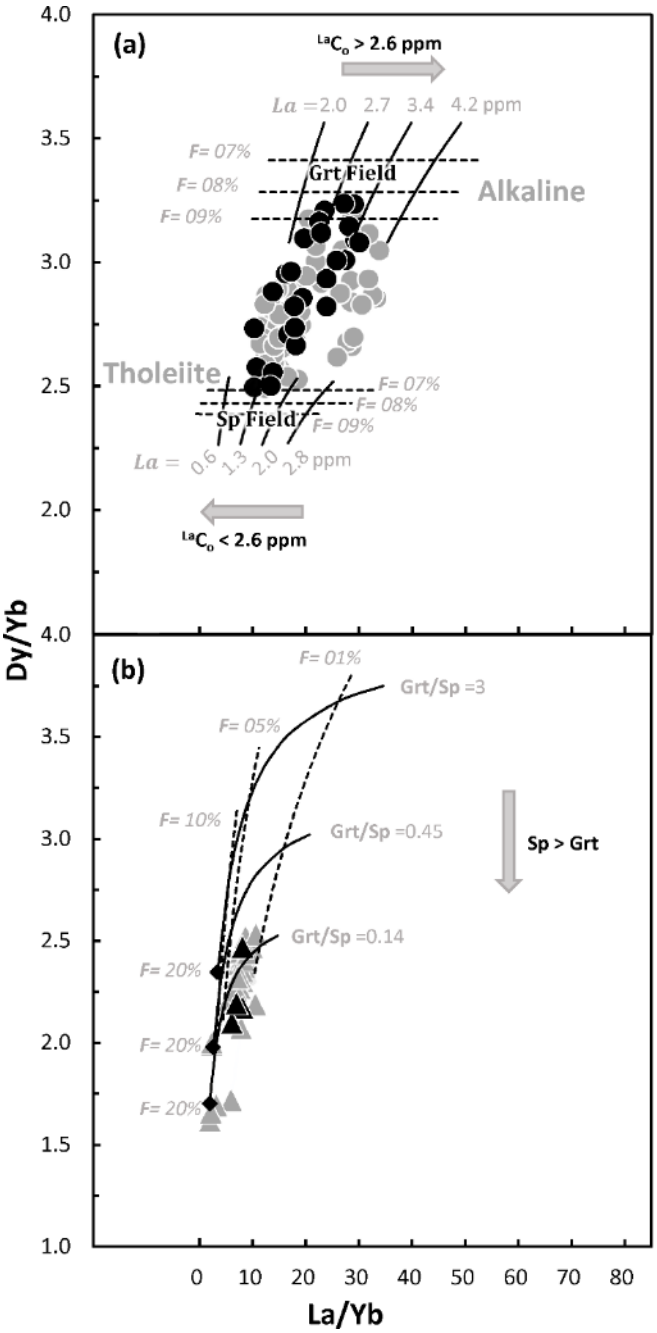

Figure 1.11 Plots of La/Yb vs Dy/Yb for SVL and Al Haruj lavas. **a)** Melt trajectories in garnet- and spinel-stability fields calculated using Eq. [1] for two residue modes, Ol_{74} + Opx_{22} + Cpx_2 + Grt_2, and Ol_{67} + Opx_{22} + Cpx_9 + Sp_2, respectively. **b)** Melt trajectories calculated using Eq. [1] for a residue mode of Ol_{50} +Opx_{26} + Cpx_{16} + Alumina $Phase_8$. The applied Kd's are given in Table 1.2.

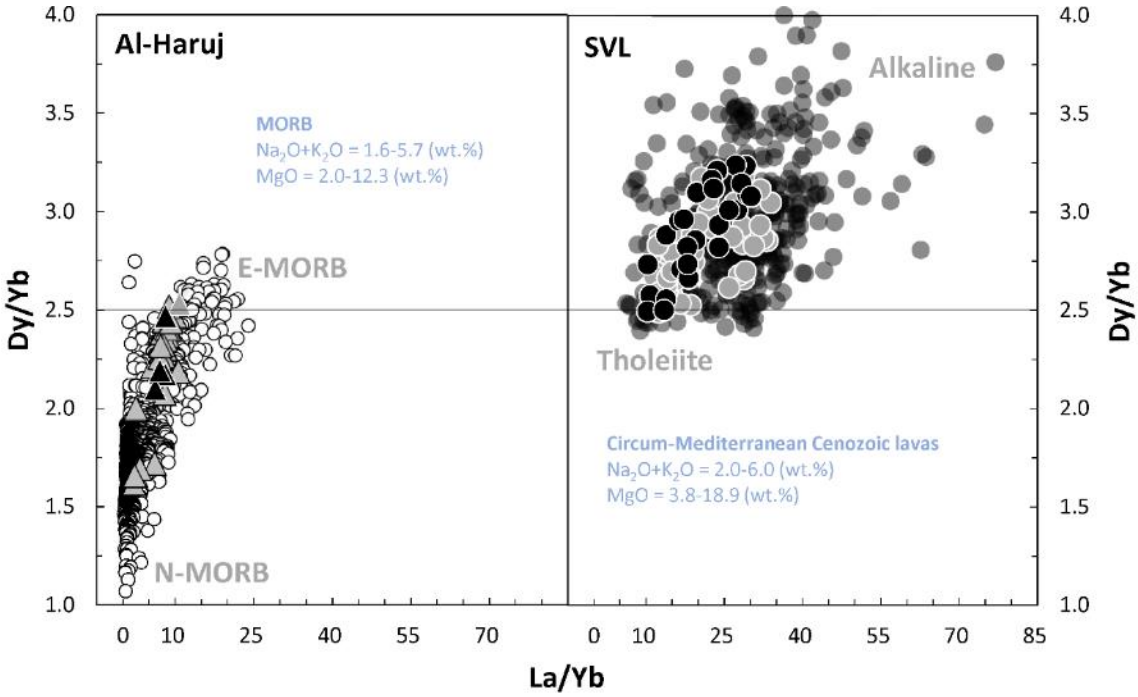

Figure 1.12 Dy/Yb vs La/Yb for the SVL and Al Haruj lavas. The alkaline-tholeiite intraplate lavas (dark grey circles) are from *N Italy-Veneto*: Beccaluva et al., 2007; Middle Atlas: Bosch et al., 2014; Germany: Jung and Masberg, 1998; Mayer et al., 2013; Central Iberia: López-Ruiz et al., 1993 and references therein. The MORB data (white circles) are from Arevalo and McDonough (2010) and the Petrological Database (PetDB).

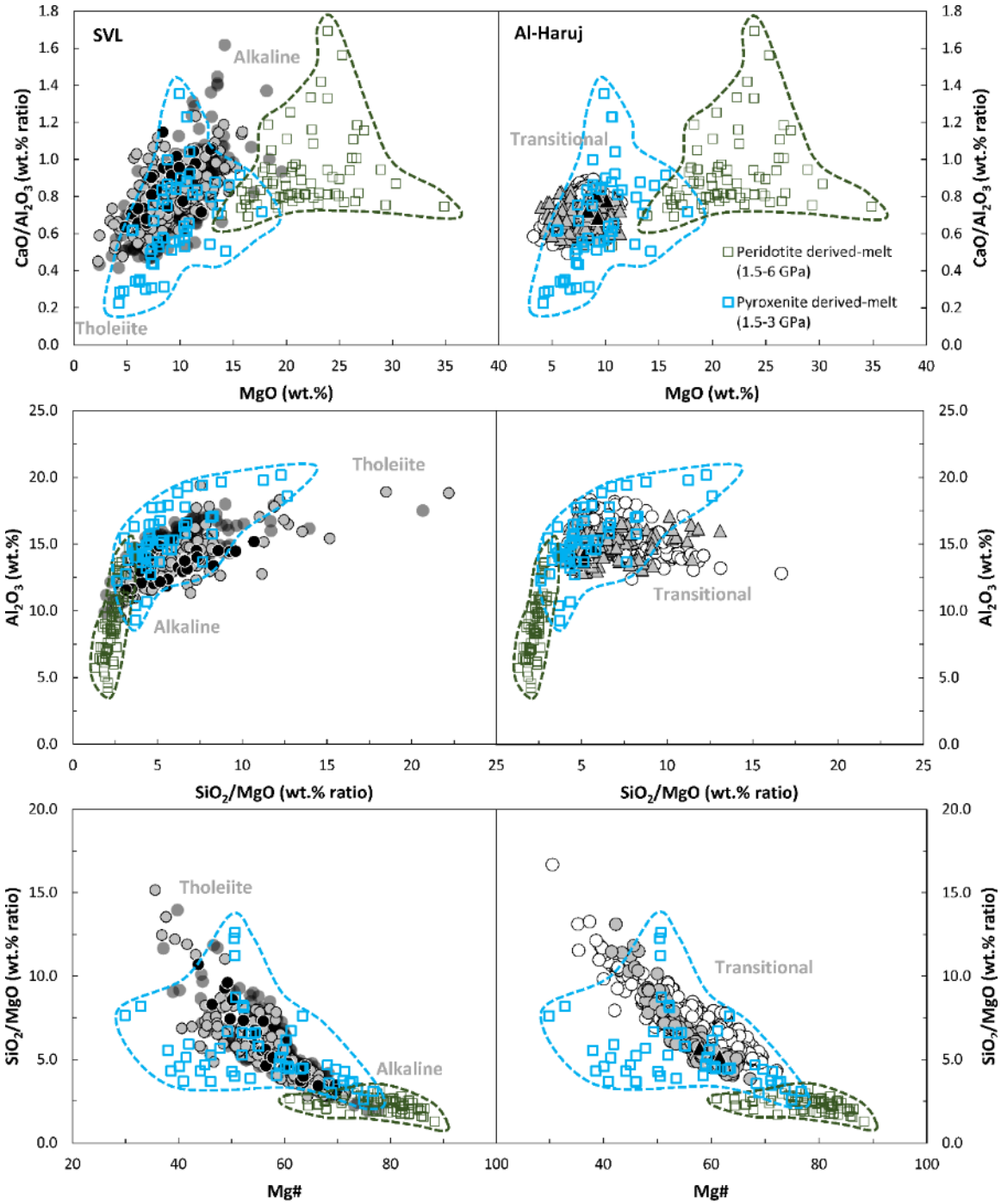

Figure 1.13 Major element characteristics of the experimental used peridotite and pyroxenite, and potential source lithology. (Experimental peridotite- and pyroxenite-derived melts: Davis et al., 2011; Falloon et al., 1988; Falloon and Danyushevsky, 2000; Kogiso et al., 1998; Lambart et al., 2013, 2012, 2009; Walter, 1998). Mg#=100MgO/(MgO+FeOT) (Molar ratio). Data symbols as in Figure 1.12.

Table 1.1 Analysis of major and trace elements of the SVL and Al Haruj lavas including standards.

Locality	Gharyan	Gharyan	Gharyan	Gharyan	Gharyan	Gharyan	Gharyan	Gharyan
Sample	A3	A5	A16	B26	B22	B23	C21	C31
Occurrence	Shield	Shield	Shield	Volcanic feeder	Volcanic feeder	Volcanic feeder	Plateau lava	Plateau lava
Major elements (wt%)								
SiO_2	48.27	47.61	45.59	46.04	45.16	44.18	51.22	52.03
TiO_2	2.06	2.16	2.32	2.72	2.88	2.7	1.94	1.89
Al_2O_3	13.24	13.79	12.08	12.03	13.29	11.31	15.18	14.44
$Fe_2O_{3\ tot}$	12.95	12.68	12.64	12.41	13.01	12.95	12.22	11.68
MnO	0.18	0.18	0.2	0.19	0.2	0.2	0.15	0.15
MgO	7.76	7.27	11.27	9.66	9.78	12.88	4.79	5.61
CaO	11.07	11.15	12.61	12.22	11.87	11.94	9.65	10.58
Na_2O	2.63	2.98	1.87	3.54	2.27	2.49	2.7	3.02
K_2O	0.99	1	0.98	0.82	0.69	0.92	0.37	0.55
P_2O_5	0.65	0.74	1.01	1	1.29	1.08	0.34	0.36
C.I.P.W.Norms								
Q	0.00	0.00	0.00	0.00	0.00	0.00	5.28	2.37
Ne	0.00	0.74	1.00	7.96	0.00	6.00	0.00	0.00
Hy	5.87	0.00	0.00	0.00	0.92	0.00	18.10	15.84
Ol	11.49	14.55	20.08	14.91	18.66	22.57	0.00	0.00
Trace Elements (ppm)								
Ni	116	116	169	149	134	219	123	87
Rb	16	20.8	16.4	27.7	14.2	21.1	4.55	6.83
Ba	383	433	679	545	574	578	357	763
Th	3.3	3.8	6.14	5.62	6.6	6.76	1.92	1.84
U	0.79	1.16	1.48	1.45	1.81	1.68	0.62	0.46
Nb	42.5	50	68.9	74.4	82.3	81.2	19.2	18.2
Ta	3.55	4.04	4.98	4.93	5.75	5.43	1.61	1.57
La	27.6	34.7	47.1	44.4	54.2	51.4	14.4	15.9
Ce	55	65.6	84	84.2	97.8	96.9	26.5	30.5
Pr	6.45	7.75	9.58	9.73	11.1	10.9	3.49	3.76
Sr	622	624	749	798	1010	913	441	417
Nd	27	33	39.1	41.1	45	45.1	15.9	17.4
Zr	164	187	201	222	239	226	113	115
Hf	4.08	4.19	4.3	4.96	5.61	5.46	3.18	3.25
Sm	5.79	6.32	7.26	8.16	8.13	7.97	4.18	4.13
Eu	1.96	2.26	2.47	2.36	2.6	2.86	1.59	1.62
Gd	5.68	6.42	6.72	7.35	8.09	7.12	5.23	5.09
Tb	0.83	0.91	0.91	0.98	0.99	1.05	0.76	0.67
Dy	4.5	5.12	5.18	5.46	5.72	5.73	4.31	4.24
Y	19.8	23	22.4	21.5	23.6	22.2	18.5	18.8
Ho	0.85	0.87	0.84	0.88	1.03	1	0.74	0.76
Er	2.08	2.62	2.37	2.28	2.47	2.42	2.09	2.01
Tm	0.25	0.31	0.32	0.29	0.29	0.28	0.27	0.26
Yb	1.66	1.92	1.72	1.86	1.85	1.77	1.53	1.55
Lu	0.21	0.25	0.25	0.25	0.27	0.24	0.21	0.19

Ol= olivine, Q= Quartz, Hy= Hypersthene, and Ne= Nepheline

* Duplicates

Table 1.1 *continued*

Gharyan C32	Gharyan B11b	Gharyan A1	Gharyan A2	Gharyan A30*	Gharyan A30*	Gharyan A9	Gharyan A13	Gharyan A27
Plateau lava	Plateau lava	Plateau lava	Plateau lava	Plateau lava	Plateau lava	Plateau lava	Plateau lava	Plateau lava
52.18	46.17	48.67	49.42	51.85	50.08	48.45	47.21	50.01
1.82	3.11	2.29	2.00	1.82	1.82	2.28	2.72	1.91
14.47	11.84	12.94	13.14	14.50	14.50	13.88	12.35	13.99
11.09	13.17	12.48	12.18	11.88	10.69	13.03	12.91	12.35
0.15	0.19	0.17	0.17	0.16	0.14	0.18	0.19	0.20
5.43	8.36	7.50	7.32	6.04	6.87	6.51	8.43	6.82
10.22	13.58	11.84	10.64	9.51	9.51	10.23	11.79	9.51
3.07	2.08	2.47	3.05	3.02	2.40	2.43	2.92	3.01
0.64	0.49	1.28	1.12	0.52	0.40	1.17	0.73	1.06
0.38	1.01	0.71	0.66	0.37	0.37	0.74	0.98	0.47
2.98	0.00	0.00	0.00	2.62	3.86	0.00	0.00	0.00
0.00	0.00	0.00	0.00	0.00	0.00	0.00	0.74	0.00
15.49	4.34	4.55	4.93	19.78	22.32	17.50	0.00	14.28
0.00	9.78	9.88	10.59	0.00	0.00	2.63	14.85	5.28
58	147	115	116	87		112	167	134
9.48	19.6	19.3	16.6	6.01		18.5	10.6	16.3
887	615	463	453	332		432	634	463
2.06	6.06	3.73	3	1.73		3.73	5.67	2.71
0.63	1.6	0.99	0.74	0.32		1.04	1.6	0.48
21	89.7	47.9	38	18.1		48.4	77.9	31
1.71	6.13	4.97	4.05	1.71		3.89	5.51	2.81
15.6	45.8	31.4	29.4	16.2		32.8	49.2	22.4
30.4	88.8	58.8	54.7	30.9		62.8	93.6	42.2
3.89	10.7	7.18	6.68	3.84		7.3	10.8	5.03
445	942	597	517	361		536	949	405
18.2	43.9	29.1	28.5	17.2		30.3	45.1	21
119	257	167	147	122		178	249	124
3.09	5.95	4.35	3.67	3.38		4.09	5.49	3.04
4.53	8.64	5.51	5.91	4.22		5.99	9.26	4.91
1.58	2.55	2.05	1.82	1.47		1.92	2.73	1.51
5.03	6.93	5.62	5.35	4.8		6.26	7.35	5.17
0.77	0.99	0.87	0.9	0.73		0.94	1.06	0.75
3.82	5.42	4.63	4.66	3.92		5.01	5.75	4.7
17.5	22.8	20	20.4	18.1		22	23.7	19.9
0.73	0.91	0.87	0.82	0.77		0.82	1.01	0.74
1.84	2.68	2.25	2.3	1.85		2.38	2.6	2.15
0.24	0.29	0.27	0.29	0.25		0.31	0.35	0.28
1.53	1.92	1.62	1.65	1.52		1.83	1.91	1.63
0.22	0.28	0.2	0.22	0.17		0.25	0.24	0.22

Table 1.1 *continued*

Gharyan A28	Gharyan A29	As Sawda A JS-1	As Sawda A JS-20	As Sawda A JS-20*	As Sawda A JS-3	As Sawda A JS-9	As Sawda B JS-1A	As Sawda A JS-7
Plateau lava	Plateau lava	Shield	Shield	Plateau lava	Plateau lava	Shield	Shield	Shield
46.98	50.02	43.53	41.63	41.22	42.46	45.55	45.72	43.7
2.63	2.31	2.24	2.61	2.57	2.09	2.01	2.13	2.04
12.16	13.37	13.87	13.82	13.96	13.65	14.83	13.24	12.96
13.48	13.84	13.62	13.74	12.22	13.3	12.9	11.98	12.44
0.19	0.17	0.22	0.22	0.21	0.2	0.24	0.2	0.21
9.11	6.03	11.99	9.01	9.20	11.44	8.92	10.28	10.96
11.65	9.83	9.93	12.33	12.76	13.33	10.96	10.26	12.13
2.36	2.99	3.61	2.74	3.45	2.63	3.29	3.49	2.96
0.70	1.33	1.53	1.26	1.46	1.31	1.03	1.08	1.35
1.01	0.59	-	-	-	-	-	-	-
0.00	0.00	0.00	0.00	0.00	0.00	0.00	0.00	0.00
0.00	0.00	15.89	13.09	16.50	12.17	8.86	9.17	13.69
7.23	12.06	0.00	0.00	0.00	0.00	0.00	0.00	0.00
12.38	5.14	23.07	15.65	14.71	20.35	17.33	18.47	17.77
177	100	232	192		309	222	213	419
15.9	21.6	9.16	26.6		20.3	16.8	7.92	22.7
572	331	453	2020		871	747	570	2920
5.13	3.57	5.61	5.34		3.18	2.84	5.17	3.41
1.37	1.13	1.67	1.44		0.77	0.84	1.68	0.89
70.6	39.4	58.5	63.5		39	33	59.4	41.6
4.84	3.1	3.29	3.99		2.08	1.86	3.27	2.33
46.4	27.7	38.8	39.4		22.9	22.4	37.7	24.2
84.8	55.1	74.7	79		46.6	46.1	72.5	48.3
10.2	6.15	8.44	9.37		5.66	5.56	8.28	5.74
873	487	863	966		691	602	817	762
41.3	26.1	35.9	38.4		23.6	23.6	33.3	25.1
242	153	193	227		142	140	193	144
5.52	3.99	4.37	5.34		3.53	3.28	4.46	3.55
7.97	5.6	7.66	7.68		5.74	5.59	7.2	5.47
2.61	2.05	2.58	2.61		1.83	1.86	2.33	1.94
7.02	5.96	7.05	7.24		4.75	5.42	6.55	5.4
0.94	0.87	0.93	0.99		0.78	0.76	0.93	0.76
5.54	4.37	5.3	5.54		4.17	4.17	5.15	4.18
22.4	19.6	21.6	24.4		17	20.3	21.8	17.9
0.92	0.81	0.83	0.97		0.7	0.92	0.88	0.72
2.31	2.03	2.28	2.5		1.8	2.16	2.3	1.84
0.31	0.28	0.28	0.3		0.23	0.23	0.27	0.22
1.71	1.41	1.65	1.75		1.41	1.63	1.65	1.41
0.26	0.25	0.23	0.26		0.19	0.22	0.21	0.16

Table 1.1 *continued*

As Sawda A JS-8*	As Sawda B JS-6	Al Haruj AHA-18	Al Haruj AHA-17	Al Haruj AHA-2	Al Haruj AHA-9	Waw Namus B AH-15	Waw Namus B AH-16
Shield	Shield	Plateau lava	Plateau lava	Plateau lava	Plateau lava	Shield	Shield
45.50	48.07	47.19	47.56	46.98	48.22	42.95	41.36
1.96	2.02	1.63	1.79	1.59	1.48	2.95	3.05
12.67	13.73	13.53	14.79	13.73	14.28	11.62	11.57
11.10	11.94	12.44	12.05	11.91	11.52	10.75	11.27
0.19	0.19	0.17	0.17	0.17	0.17	0.18	0.19
9.91	7.28	10.11	8.35	9.12	9.3	12.41	13.19
12.12	12.4	10.56	10.74	11.13	9.82	14.14	14.24
2.90	2.79	2.76	3.05	2.82	2.9	1.77	1.93
1.30	1.05	0.71	0.87	0.59	0.6	0.6	0.55
-	-	-	-	-	-	-	-
0.00	0.00	0.00	0.00	0.00	0.00	0.00	0.00
9.44	3.28	1.98	3.06	2.24	0.00	7.51	9.20
0.00	0.00	0.00	0.00	0.00	3.08	0.00	0.00
14.68	10.94	20.09	16.43	17.33	17.39	16.29	19.19
	196	294	180	221	193	264	273
	15.7	10.7	15	7.13	10.9	26.1	22.6
	1320	251	187	225	426	542	542
	2.94	1.88	2.15	1.4	1.58	6.96	7.05
	0.86	0.69	0.45	0.48	0.59	1.82	1.88
	37	15.2	16.6	15.3	11.6	85.4	82.8
	2.15	0.91	1.01	0.91	0.66	5.04	4.79
	23.1	12.8	14.4	11.2	10.2	55.8	54.7
	45.8	28.1	31.4	25	23.3	108	107
	5.74	3.66	3.96	3.03	3.05	12.6	12.4
	972	495	378	480	374	823	791
	23.5	15.6	17.8	14.2	13.8	48.8	49.8
	148	121	135	107	103	267	263
	3.61	3.33	3.62	2.65	2.75	6.31	5.99
	5.46	3.68	4.84	3.43	3.05	9.59	9.5
	1.84	1.36	1.51	1.25	1.32	3.13	3.03
	5.4	4.38	4.6	4.27	3.99	9.03	8.15
	0.74	0.53	0.71	0.6	0.58	1.15	1.13
	4.33	3.41	4.37	3.82	3.18	6.23	5.61
	20.4	16.2	19.5	17.2	17	26.1	25.8
	0.79	0.66	0.8	0.73	0.65	1.11	1.08
	2.11	2.13	2.44	2.06	2.02	2.68	2.64
	0.26	0.24	0.25	0.24	0.25	0.36	0.32
	1.73	1.57	1.77	1.82	1.45	1.98	1.82
	0.25	0.2	0.26	0.23	0.2	0.26	0.27

Table 1.1 *continued*

	Analysis			Literature values		
	USGS GSP-1	USGS G-2	USGS DNC-1	USGS GSP-1 Mean	USGS G-2 Mean	USGS DNC-1 Mean
Si	32.34		22.05	31.46		22.04
Ti	0.39		0.29	0.39		0.29
Al	8.01		9.73	8.02		9.71
Fe	2.98		7.03	3.01		6.97
Mn	0.03		0.11	0.03		0.12
Mg	0.58		6.28	0.60		6.11
Ca	1.43		8.39	1.46		8.21
Na	1.96		1.43	2.08		1.40
K	4.53		0.19	4.57		0.19
P	0.15		0.03	0.12		0.03
Ni		27.4	241		4.9	247
Rb		163	3.16		170	4.5
Ba		1930	106		1880	118
Th		25	0.245		24.6	0.2
U		2.04	0.0738		2.04	0.1
Nb		12	1.59		13	3
Ta		0.786	0.101		0.88	0.098
La		88.9	3.7		86	3.6
Ce		164	8		159	10.6
Pr		16.5	1.1		19	1.3
Sr		476	140		478	144
Nd		54.3	5.09		53	5.2
Zr		330.0	35.1		300	38
Hf		8.09	1.08		7.9	1.01
Sm		6.94	1.26		7.2	1.38
Eu		1.49	0.584		1.41	0.59
Gd		4.12	1.79		4.1	2
Tb		0.454	0.462		0.48	0.41
Dy		2.2	2.88		2.5	2.7
Y		9.3	16.4		11.4	18
Ho		0.374	0.657		0.37	0.62
Er		0.957	2.21		1.2	2
Tm		0.119	0.28		0.17	0.33
Yb		0.709	2.1		0.78	2
Lu		0.112	0.314		0.113	0.32

Table 1.2 Average compositions of mantle peridotites and partition coefficients (Kd's) used in modeling.

	Lithospheric Mantle† of McDonough (1990)		Primitive Mantle† of McDonough &Sun (1995)		K_d's*				
					ol	opx	cpx	sp	grt
La	2.6		0.648		0.0004	0.0008	0.054	0.01	0.01
Dy	0.51		0.674		0.0017	0.077	0.33	0.01	1.06
Yb	0.26		0.441		0.0015	0.22	0.28	0.01	4.03
ol	62	65	56	57					
opx	24	28	22	16					
cpx	12	3	19	14					
sp	2	-	3	-					
grt	-	4	-	13					

ol= olivine, opx= orthopyroxene, cpx= clinopyroxene, sp= spinel, grt= garnet

† REE Concentrations are in ppm and peridotite modes are in %.

* Partition coefficients are from McKenzie and O'Nions (1991), except for opx, which is from Green et al. (2000).

CHAPTER 2

Orogeny-Modified lithosphere: Insights from Re-Os systematics in peridotitic assemblages

2.1 Introduction

The isotopic and geochemical composition of the lithospheric mantle is usually discerned from xenoliths or directly from the mantle segments (orogenic peridotites) obducted into orogenic belts (e.g., Bohemian Massif: Ackerman et al., 2016; Totalp massif: van Acken et al., 2010; Lherz Massif: Mukasa et al., 1991; Horoman Massif: Yoshikawa and Nakamura, 2000). Xenoliths are pieces of the mantle exhumed by volcanism. They are usually collected from basaltic lava flows in intraplate and rift settings (e.g., circum-Mediterranean: Beccaluva et al., 2008, 2007; Miller et al., 2012; Wittig et al., 2010; Cannatelli, 2012; Puziewicz et al., 2015; WittEickschen et al., 1997; Australia: Matsumoto et al., 2002, 2000; North China Craton and the South China Block: Chen et al., 2007; Choi et al., 2005; Ying et al., 2006). The predominant lithology of xenoliths is peridotite, but cumulates such as pyroxenites and dunite are also frequent (e.g., Dobosi et al., 2003; Rudnick et al., 2004; Witt-Eickschen and Kramm, 1998; Xu, 2002).

The most prevalent view of the subcontinental lithospheric mantle (SCLM) is that it is depleted regarding major elements (has high Mg-number, reflecting residual minerals) due to its old isolation from the homogenizing effects of convection and the segregation of the crust from the mantle. The extensive database of isotopic model ages, measured in SCLM primary lithologies (e.g., lherzolites and harzburgites), has shown long-term isolation since the Archaean and early Proterozoic eras. However, post-

depletion enrichment in peridotites by a metasomatizing process is pervasive in the mantle peridotites. It is a process that leads to subordinate textural and compositional changes in the peridotite assemblages. It has been the subject of many studies concerning the nature of the SCLM (e.g., circum-Mediterranean: Beccaluva et al., 2008, 2007, 2001; Bianchini et al., 2007; Natali et al., 2013; Colorado Plateau: Lee, 2005; Li et al., 2008; North China craton: Ying et al., 2006; Zheng et al., 2001). The enrichment observed in the xenoliths has different expressions, ranging from cryptic, reflected in the chemistry of the peridotite forming-minerals such as clinopyroxene (e.g., Bianchini et al., 2007) to modal changes such as the presence of hydrous silicates (amphibole or phlogopite, e.g., Alard et al., 2011; Witt-Eickschen et al., 2003). The hydrous phases occur in veins or metasomatic selvages around the veins, as observed in orogenic peridotites (Bodinier et al., 1990; Downes, 2002; McPherson et al., 1996). Spongy texture, also called sieved texture, is another sign of enrichment. It is a petrographic feature found mainly in clinopyroxene and spinel (Beccaluva et al., 2008; Carpenter et al., 2002; Miller et al., 2012; Su et al., 2011). The spongy texture in peridotites is commonly interpreted as the result of alterations or interactions with a metasomatic fluid or melt before xenolith entrainment in the host lava (Bonadiman et al., 2005; Carpenter et al., 2002; Ionov et al., 1994).

Two prominent issues regarding SCLM enrichment or metasomatism are still ongoing. First is the ages of metasomatic events. Second is the origin of the metasomatic agents. Compositionally, the agents are identified as volatile-rich silicate melts or carbonatitic melts (Bodinier et al., 2004; Frezzotti et al., 2002; Miller et al., 2012; Natali et al., 2013). Others have specified kimberlite-like melt as a metasomatic agent

(Bonadiman et al., 2005; Kamenetsky et al., 2004), suggesting a lithospheric source. Given the ancient depletion history of SCLM and the enrichment overprints, SCLM is not a closed system. It is due to the tectonic history of the continents as a result of the amalgamation of supercontinents, opening and closing ancient oceans. However, the lithophile isotopic systems (e.g., Rb-Sr, Sm-Nd, and Lu-Hf) have provided opportunities to define the origin of the reactants or their timing. In fact, the diversity of Sr, Nd, and Pb isotopes of peridotites (Downes, 2002; Mukasa et al., 1991; Witt-Eickschen et al., 1997; Wittig et al., 2007) encompass the entire spectrum measured in intraplate volcanics, whether sampled by young volcanics erupted on continents (Lustrino and Wilson, 2007) or in ocean island basalts (Stracke et al., 2005). On the other hand, isochrons of mantle lithologies have been only reported in cumulate assemblages such as pyroxenites (Sm-Nd system: Ackerman et al., 2009; Borghini et al., 2013; Medaris et al., 1995; Santos et al., 2002; Lu-Hf system: Ackerman et al., 2016; Re-Os system: Ackerman et al., 2013; Meisel et al., 2001a). The ages generally correspond to the orogenic ages recorded in the surrounding crustal blocks.

The SCLM peridotites characteristically show signs of ancient melt extractions. Residual trends in the peridotites have records of melt extractions up to 40% (Arai, 1994). These features are reflected in the mineralogy of residual peridotites and their bulk compositions (e.g., many are harzburgites with < 5% clinopyroxene). Some siderophile elements, including Os, preferentially enter the residue during peridotite melting. Thus, Os abundance in peridotites is an excellent indicator of the refractory nature of portions of the SCLM. Os isotopes are capable of providing information on the SCLM depletion ages and isotopic evolution through time.

This study examines the time residence of SCLM depletion and post-depletion enrichment, using Re-Os systematics measured in peridotitic assemblages. New Re-Os bulk and isotopic analysis carried out on xenoliths entrained in Cenozoic lavas in the Sahara Craton yield one of the most precise bulk-rock Re-Os isochrons yet reported in peridotitic assemblages, revealing that parts of the Sahara SCLM depletion were coeval with the Pan-African orogeny.

2.2 Geologic background

Examples of well-documented cratonic areas surrounded by orogenic silicic magmatism and metamorphism are the North China Craton (Tans-Central orogeny; Zhao et al., 2000), Colorado Plateau (Yavapai orogeny; Karlstrom and Daniel, 1993), and SE Australia (Delamerian orogeny, Foden et al., 2008). The Sahara Craton is not different. Geochronological and isotopic data indicate that the Sahara crust is heterogeneous, particularly in contrast with the juvenile crust of the Arabian-Nubian terranes to the east (Neoproterozoic) and the Archean continental crust of the Congo and West African Cratons in the south and west, respectively (Abdelsalam et al., 2002; Liégeois et al., 2013 and references therein). The Sahara lithosphere changed not only on its margins but also within its interior. The abundant presence of ~ 600 Ma anorogenic granitoids demonstrates that the Pan-African tectonic-thermal events are recorded (Figures 2.1 and 2.2). Protoliths and model ages of the crustal rocks are Paleoproterozoic and Archean. Together with the pristine Archean terranes of the Uweinat-Kamil inlier at the core of the craton (3.0–3.2 Ga; Bea et al., 2011), and the lack of suture lines and calc-alkaline volcanics within the craton limits, which would indicate plate subduction, the pre-Neoproterozoic features suggest that the Sahara Craton behaved as a single block during

the Phanerozoic. The fact that the Sahara lithosphere was subjected at the end of the Neoproterozoic to collisional events along all its margins against the Tuareg Shield (with the West African craton behind) in the west, against the Congo craton and intervening Pan-African belts to the south, against the Arabian-Nubian Shield to the east, and an unknown continent to the north (Abdelsalam et al., 2002) is a feature of " no-escape" tectonics.

The spatial distribution of the postorogenic volcanism within the Sahara is delineated by the boundaries of intracratonic sag basins (Figure 2.1). Sagging of a basement is commonly attributed to an intensely heated lithosphere and subsequent cooling (Leighton et al., 1990; Macgregor, 1996; Schandelmeier, 1988). Recent seismic tomography of North Africa revealed a possibility of multiple cratonic roots beneath Chad, Murzuq, and Al-Kufrah basins within the larger Sahara Craton (Emry et al., 2019). The study suggests that the high and low anomalies in wave velocities could be related to the downward lithospheric roots and metasomatism during the Pan-African collisions. Overall, the Sahara Craton does not possess a standard configuration that would be expected for a craton. Its lithospheric mantle could have been affected by Pan-African collisions that are reflected in coeval crustal magmatism and metamorphism.

2.3 Petrography of the Sahara xenoliths

The xenoliths were collected from Gharyan and As Swada volcanic fields (Figure 2.1). They are up to 10 cm in diameter. Petrographic inspection shows evidence of metasomatic reactions similar to the peridotite xenoliths reported by Beccaluva et al. (2008) and Miller et al. (2012) from Gharyan and Waw Namus volcanic fields, respectively (Figure 2.3). They possess spongy or reaction patches of microcrysts of

clinopyroxene and probably olivine, as well. There is no preferential development of the spongy patches observed along the ' 'xenolith's margins with the host basalt, suggesting that magma at the time of entrainment had no role in their formation. Re-equilibration of xenolith minerals with host lavas is also unlikely due to the vitric groundmass of the host olivine basalt that suggests fast cooling, hence a lack of opportunity for thermal equilibration.

The studied peridotites are characterized by a four-phase mineral assemblage of olivine + orthopyroxene + clinopyroxene + spinel with protogranular (sinuous mineral boundaries) to granular textures. The grain size ranges between 1 and 2 mm. Sulfide grains were found within spinel crystals. Some xenoliths show reddish-brown stains due to oxidation, which is microscopically evident along peripheries and in olivine's internal fractures. Kink bands and subgrain boundaries are frequent in olivine and clinopyroxene, but no foliation or layering is observed. Hydrous phases (amphibole or phlogopite) as constituents of the mineral assemblage were not found.

2.4 Analytical methods

2.4.1 Bulk-rock and mineral analyses of the xenoliths

Bulk-rock major element abundances of seven xenoliths (Gharyan locality: GH-9, GH-12, GH-26, A-4, and GH-13, As Sawda locality: JS-14 and JS-10) were measured using Inductively Coupled Plasma Optical Emission Spectrometry at the University of Missouri. The results are presented in Table 2.1. Three out of six mantle xenoliths were selected for a detailed quantitative analysis of minerals. Analyses carried out using the JEOL-JXA 8200 microprobe at the Earth and Planetary Sciences Microanalysis Facility of Washington University in St. Louis. The analyses were done using 15 kV acceleration

voltage, 25 µA specimen current, 5 µm beam size, and 40 s net acquisition time. Synthetic and natural minerals were used as standards. Based on core and rim analyses in each mineral, large crystals are homogenous and, thus, average and representative compositions are reported in Tables 2.2-6.

2.4.2 Re-Os isotopic analyses

The sample preparation and analytical procedures to measure Re and Os isotopes followed those detailed in Carlson et al. (1999) and were performed at the Department of Terrestrial Magnetism (DTM), Washington, DC. The sample preparation procedure included Carius tube digestions of 1 g of xenolith, using ^{185}Re-^{190}Os spikes with $^{185}Re/^{190}Os = 6$ for the lavas and 0.6 for the xenoliths. The digestions were followed by Os extraction and Re purification on anion exchange columns. Osmium was loaded onto Pt filaments with $Ba(NO_3)_2$ as an activator and analyzed as negative ions using a Thermo-Fisher Triton thermal ionization mass spectrometer (TIMS). Re fractions were analyzed using a Nu-Plasma ICP- mass spectrometer.

All runs were corrected for their oxide compositions and mass fractionation using the $^{192}Os/^{188}Os$ ratio of 3.083. As part of the analysis and between each sample batch, runs from the in-house Os isotope reference material "J-M Os" yielded $^{187}Os/^{188}Os$ ratio 0.17383 ± 0.0002 (2σ std. dev., n=4). This value characterizes the external precision of the sample analysis within 0.9 ‰ of the recommended value (0.17399). In-run precision for $^{187}Re/^{185}Re$ was better than 0.2%. Correction for blank Os contribution in the bulk-xenoliths Os was 0.11 to 0.29%. Re concentrations were corrected using a Re blank of 2 pg. The average proportions of Re in the blank to Re in the xenoliths were 2%.

2.5 Results

2.5.1 Mineral and bulk-rock composition

Spinel is the Al-bearing phase in all the studied xenoliths. It is the least abundant phase. Compositionally, it is fairly uniform with Cr_2O_3 between 7.7 and 10.4 wt. %, Mg-number [Mg/(Fe^{2+}+Mg)] 0.7–0.8 and Cr-number [Cr/(Cr+Al)] 0.08–0.11 (Figure 2.4a). The compositions are projected onto the basal plane of the spinel prism. Clino- and orthopyroxenes are both magnesian (Figure 2.4b). Orthopyroxene composition varies in the following ranges: $Wo_{1.0–1.7}En_{87.7–89.4}Fs_{9.1–10.6}$, with Mg-number from 0.88 to 0.9 and Cr-number from 0.03 to 0.05. Al_2O_3 and Cr_2O_3 contents have broader compositional ranges from 2.5 to 5.5 wt. % and from 0.2 to 0.36 wt. %, respectively. Clinopyroxene shows a compositional variation in relation to its textural position. Large equilibrated diopside crystals are $Wo_{45.1–48.5}En_{48.5–49.7}Fs_{5.6–7.6}$, with Mg-number 0.88–0.93, Cr-number 0.05–0.08, Na_2O 1.7–1.8 wt. % and TiO_2 0.4–0.6 wt. %. Reaction patches and microcrysts that overprint some clinopyroxene and orthopyroxene crystals have lower Na_2O concentration, down to 0.4 wt. %. Large kinked crystals of olivine (up to 1 mm) are Fo_{89-90} (Figure 2.4c). Modal analyses and major element mass-balance calculations show that all the samples are lherzolites, with the following modal abundance: ol 59–77%, opx 12–34%, cpx 8–17%, sp 1–3% (Table 2.1).

2.5.2 Re-Os systematics

Bulk-rock analyses of Re and Os were performed on six xenoliths, and the results are shown in Table 2.7. Bulk Os concentrations vary from 844 to 1737 ppt, whereas bulk-Re concentrations fall into the range of 54 to 121 ppt. The concentrations are within the limits of bulk-rock analyses measured in peridotite assemblages (Figure 2.5).

As with other isotope systems and assuming that the Re/Os of a sample is representative of its longstanding history in the mantle, the age-dependent depletion in $^{187}Re/^{188}Os$ ratio can be denoted by T_{MA} and T_{RD}:

$$T_{MA} = \frac{1}{\lambda}\ln\left[1 + \frac{\left(\frac{^{187}Os}{^{188}Os}\right)_{PUM\ 0r\ CHON} - \left(\frac{^{187}Os}{^{188}Os}\right)_{Sample}}{\left(\frac{^{187}Re}{^{188}Os}\right)_{PUM\ or\ CHON} - \left(\frac{^{187}Re}{^{188}Os}\right)_{Sample}}\right]$$

$$T_{RD} = \frac{1}{\lambda}\ln\left[1 + \frac{\left(\frac{^{187}Os}{^{188}Os}\right)_{PUM\ or\ CHON} - \left(\frac{^{187}Os}{^{188}Os}\right)_{Sample}}{\left(\frac{^{187}Re}{^{188}Os}\right)_{PUM\ or\ CHON}}\right]$$

where PUM and CHON are the present-day averages of the primitive upper mantle and chondritic composition, respectively, and λ is the decay constant for the Re-Os system (λ = $1.666x10^{-11}$, Smoliar et al., 1996).

These are model ages that account for the time since the separation or deviation from a mantle that had a primitive or chondritic isotopic evolution. In the T_{MA} calculation, the measured $^{187}Re/^{188}Os$ ratio is used, assuming not all of the Re was removed from the sample. In the T_{RD} ages, it is assumed that all of the Re was removed and the $^{187}Os/^{188}Os$ ratio has not changed since the depletion event. The present-day isotopic ratio of the primitive upper mantle (PUM, Meisel et al., 2001b) is adopted here for calculating the model ages because it is an estimate based on the global compilation of bulk-rock analysis of primitive peridotites. Using values of $^{187}Os/^{188}Os$ =0.1296 and $^{187}Re/^{188}Os$=0.433, the model T_{MA} and T_{RD} ages of the analyzed xenoliths are 1433-1846 Ma and 268-841 Ma, respectively, except for sample GH-26 with T_{MA}= 46 Ma and future T_{RD}= -15 Ma (Table 2.7). The trajectories of calculated T_{MA} and T_{RD} for all analyzed

samples are shown in Figure 2.6. The TRD ages are more useful by assuming the entire removal of Re in the sample.

2.6 Discussion

2.6.1 The Sahara peridotites and residue trends

All the reported peridotites within the limit of the Sahara Craton are spinel-facies peridotites with the modal proportion of clinopyroxene and spinel in 3-18% and 1-3%, respectively (Beccaluva et al., 2008; Lucassen et al., 2008; Miller et al., 2012). Collectively, to evaluate the stance of the Gharyan and As Sawda peridotites with respect to depletion as indicated from their model ages (Table 2.7), the bulk major element compositions and mineral chemistry are compared with references to the primitive mantle (Figures 2.7 and 2.8).

The data shows that only the Gharyan xenoliths may have been enriched after a depletion event. All others from the Sahara, including As Sawda xenoliths, are either primitive or depleted. The alumina and silica contents in the analyzed suite are the lowest in the As Sawda xenoliths (Al_2O_3 =2.27-2.61 wt.%, SiO_2 =44.08-44.96 wt.%, Figure 2.7). Also, the modal analyses of clinopyroxene are relatively lower in the assemblage with respect to Gharyan peridotites (cpx 9-12%, Table 2.1). The contents of Al_2O_3 and SiO_2 in two samples from Gharyan xenoliths are similar or slightly higher than the average of the primitive mantle, probably because of their high modal proportions in spinel and clinopyroxene (Figure 2.3). In general, the Sahara peridotites follow the depletion trend that results from progressive partial melting (Niu, 1997). Spinel composition is a good indicator for distinguishing melt removal from melt-rock interaction (Arai, 1994; J. A. Pearce et al., 2000; Zhou et al., 1996). The Cr-number of

spinel and Mg-number of olivine of the Gharyan peridotites resemble those in a primitive mantle with no or less than 3% of melt extraction. Most Sahara xenoliths show up to 30% melt extraction (Figure 2.8).

2.6.2 The Os systematics in sulfides and silicates

Given the siderophile nature of Os, mantle residue is expected to become enriched in Os as melting proceeds, while Re becomes extracted by partial melts. Thus, the Re/Os ratio of the primordial mantle decreases when partial melting occurs. Subsequently, the growth trajectory of the $^{187}Os/^{188}Os$ ratio to the present day is different. The bulk $^{187}Os/^{188}Os$ ratio of refractory peridotites is usually below the present-day estimate of primitive peridotites (PUM= 0.1296; Meisel et al., 2001b) or the present-day ratio of carbonaceous chondrites (0.1270, Luck and Allègre, 1983; Walker and Morgan, 1989), ordinary chondrites (0.1289 ± 0.0022, Meisel et al., 1996), and enstatite chondrites (0.1281 ± 0.0004, Walker et al., 2002). For instance, in kimberlite-derived peridotites, the bulk $^{187}Os/^{188}Os$ ratio can be as low as 0.106 (Pearson et al., 1995).

The xenoliths from the Gharyan Province possess bulk $^{187}Os/^{188}Os$ ratios between 0.12971 and 0.12689, which are comparable with the average chondritic composition and the estimate for primitive peridotites. The Os isotopic composition of xenoliths from the As Swada Province is lower with an average of 0.12373±0.00024, as can be inferred from their relatively depleted $^{187}Re/^{188}Os$ ratios (Table 2.7). In an analysis of bulk rocks, however, the dispersion of Os among minerals often suffers from a " nugget" effect, particularly in nonsilicates (e.g., sulfides, oxides, and alloys). The high $K_d^{Os}{}_{Sulfide/Silicate}$, for instance, imposes Os bias toward sulfides (Harvey et al., 2016). Analyses show that sulfides can contain 1000's of ppm or % levels of Os (Aulbach et al., 2016; Griffin et al.,

2004). On the contrary, the Os concentrations measured in silicates are 1000's times less than in sulfides, often at sub-ppb levels (Burton et al., 2000; Harvey et al., 2011, 2010). Although sulfides have very low modal abundances, they have diverse Os concentrations (Alard et al., 2011; Burton et al., 2002; Harvey et al., 2011).

Sulfides being the primary Os host in the mantle, it is pointed out that determining the paragenesis of sulfides in peridotite assemblages within the lithospheric mantle that has experienced multiple thermal-tectonic events or mineralogical modifications is difficult (Harvey et al., 2016). Therefore, Os concentrations and isotopic ratios of sulfides obtained by direct analysis in peridotite assemblages are compiled and presented in Figure 2.9. The Os systematics in sulfides are defined according to the assemblage refractoriness, using the bulk Al_2O_3/SiO_2 wt.% ratio as a depletion index. The ratio can be used as an indicator for melt removal, which reduces the Al content in the residual mantle. Absolute concentrations and isotopic ratios of bulk-Os are also plotted for comparison, including this study's xenoliths.

The data displayed in Figure 2.9a show unequal distribution of Os either within the single sample for sulfides or within the entire residue trend for the bulk-rock. Notably, the Os range in sulfides becomes higher in more refractory compositions, as measured by decreasing Al_2O_3/SiO_2 ratios. Similarly, peridotite compositions with low Al_2O_3/SiO_2 ratios have a larger Os concentration range, from 10^{-3} to 10^{-2} ppm, than more primitive peridotites. The exclusive occurrences of high Os-sulfides in refractory assemblages are consistent with Os compatibility nature. In situ analyses show that sulfide-bearing silicates tend to be higher in Os content than sulfide-free silicates (Burton

et al., 2000, 1999), suggesting that in residual rocks with elevated Os concentrations, sulfides remain armored and in equilibrium with refractory silicates.

As shown by compiled data in Figure 2.9b, many sulfides have isotopic ratios that are subchondritic or below the estimate of primitive peridotites. However, radiogenic Os is also frequent, giving future T_{RD} model ages. The most radiogenic Os occurs in the depleted assemblages, contradicting that the SCLM is an ancient refractory mantle. These radiogenic values occur within relatively low-Os sulfides and are commonly ascribed as a population introduced by metasomatism (Alard et al., 2011; Griffin et al., 2004; Harvey et al., 2010; Wang et al., 2009). On the other hand, the isotopic composition of the bulk-Os does not reproduce the radiogenic values along the residue trend. On the contrary, the most refractory assemblages have old T_{RD} ages suggesting that the whole-rock $^{187}Os/^{188}Os$ ratio does not account for the post-depletion enrichment of the Os isotopic ratios, which suggests that enrichment in the refractory sulfides is fairly cryptic.

2.6.3 Depletion and Re-Os model ages of the Sahara peridotites

The model ages of Gharyan and As Sawda xenoliths document the presence of an ancient lithosphere beneath the Sahara Craton during the outpouring of basaltic lavas in the Cenozoic time (Figure 2.6). The T_{MA} ages are Proterozoic, with both Gharyan and As Sawda xenoliths having depletion ages greater than 1400 Ma. One sample from Gharyan xenoliths (GH-26, Table 2.7), however, has a T_{MA} age of 45 Ma and $^{187}Re/^{188}Os$ ratio being the highest in the suite.

In contrast to T_{MA} ages, the T_{RD} ages for Gharyan and As Sawda xenoliths are younger (Figure 2.6). Although T_{RD} age calculation will only yield a minimum age by assuming a complete removal of Re, it is only useful if the Re concentration is very low.

The T_{RD} ages of As Sawda xenoliths yield older ages (775-841 Ma) than the T_{RD} ages of the Gharyan xenoliths (268-326 Ma). Again, the Gharyan sample GH-26 yields a meaningless T_{RD} age in the future (-15 Ma), because it exceeds the present time $^{187}Os/^{188}O$ ratio of PUM by a fraction of 0.0001. Overall, the contrast of T_{RD} ages between As Sawda and Gharyan xenoliths agrees with their major element's systematics. In contrast, the As Sawda xenoliths and most others from the Sahara show long-term depletion of the SCLM, and the Gharyan xenoliths might have experienced a latter post-depletion enrichment (Figure 2.7).

2.6.4 Coeval Pan-African age

In the Gharyan xenoliths, the bulk $^{187}Os/^{188}Os$ and $^{187}Re/^{188}Os$ ratios create an isochronous relationship with an MSWD value of 1.3 and an age of 653±150 Ma (Figure 2.10). Within analytical uncertainty, the isochron has an age in agreement with the age of the Pan-African Orogeny (Figure 2.2). Preservation of a Pan-African age demonstrates that a thermal event associated with the collision was imposed on parts of the SCLM that have effectively reset the $^{187}Os/^{188}Os$ ratios on the scale sampled by the xenoliths.

The samples from As Sawda locality deviate from the isochronous relation. This may be due to their Re depletion levels with respect to Gharyan xenoliths. The Al_2O_3/SiO_2 and Re/Os ratios of As Sawada xenoliths are the lowest in the suite, suggesting that they have experienced a high amount of melt removal in past, but were not subsequently enriched again (Figure 2.9). As a result, the low Re/Os ratios in As Sawda xenoliths must have led to a lower growth trajectory of $^{187}Os/^{188}Os$ ratios since the thermal event, or the xenoliths were not thermally reset. On the other hand, the bulk and

mineral compositions of the isochron-forming peridotites from the Gharyan locality preclude the removal of significant amounts of melt (Figures 2.7 and 2.8).

2.6.5 Comparison with North China Craton

In principle, isochron-forming components must be thermally equilibrated at the time given by the isochron age. In most cases worldwide, there is an absence of meaningful Re-Os isochrons, except for the reported case of North China Craton (Figure 2.11, Gao et al., 2002). The isochronous relationship comprises a subset of data points from Hannuoba peridotites. When forced through the average of the primitive peridotites $(^{187}Os/^{188}Os)_{PUM}$= 0.1296, the isochron yields an age around 1900 Ma, which corresponds to the age of the North China collisional orogeny (1800-2000 Ma, Gao et al., 2002; Li et al., 2001, 2000).

The SCLM beneath the Gharyan volcanics and of the North China Craton shows thermal resetting during continent-continent collisions. The initial ratios of both isochrons resemble the isotopic compositions of the primitive or chondritic-like mantle at the time of the orogeny (Figure 2.12). However, the Gharyan isochron is below the PM average, which indicates that the SCLM sampled by the Gharyan xenoliths must have undergone some depletion in the past. The range in Re/Os ratios in the xenoliths suggests that the thermal resetting was accompanied by an addition of Re at the orogeny time. The addition of Re to some parts of the Sahara SCLM is suggested by one of the isochron-forming peridotites as its Re/Os ratio exceeds that of the PUM average (Figure 2.10).

2.7 Conclusion

The bulk Re-Os systematics of the peridotites within distinct parts of the Sahara Craton has a record of a lengthy depletion of the SCLM. The time-integrated depletion is

reflected on growth trajectories of the measured Os isotopic ratios. Although most Saharan xenoliths suggest that the SCLM has undergone a partial melting event in the Neoproterozoic time, xenoliths from the Gharyan province yield an isochronous relationship with the age of 653 Ma. The age is interpreted to be the elapsed time since their last thermal adjustment, which was instigated by an interfering heat source without reaching the solidus. The heterogeneity in Re-Os isotope systematics of the Sahara SCLM, as recorded by the xenoliths, suggests that the irregular structure of the Sahara lithosphere could be the result of continental collisions associated with the Pan-African orogeny.

References

Abdelsalam, M.G., Liégeois, J.P., Stern, R.J., 2002. The Saharan Metacraton. J. African Earth Sci. 34, 119–136. https://doi.org/10.1016/S0899-5362(02)00013-1

Ackerman, L., Bizimis, M., Haluzová, E., Sláma, J., Svojtka, M., Hirajima, T., Erban, V., 2016. Re-Os and Lu-Hf isotopic constraints on the formation and age of mantle pyroxenites from the Bohemian Massif. Lithos 256–257, 197–210. https://doi.org/10.1016/j.lithos.2016.03.023

Ackerman, L., Jelínek, E., Medaris, G., Ježek, J., Siebel, W., Strnad, L., 2009. Geochemistry of Fe-rich peridotites and associated pyroxenites from Horní Bory, Bohemian Massif: Insights into subduction-related melt-rock reactions. Chem. Geol. 259, 152–167. https://doi.org/10.1016/j.chemgeo.2008.10.042

Ackerman, L., Pitcher, L., Strnad, L., Puchtel, I.S., Jelínek, E., Walker, R.J., Rohovec, J., 2013. Highly siderophile element geochemistry of peridotites and pyroxenites from Horní Bory, Bohemian Massif: Implications for HSE behaviour in subduction-related upper mantle. Geochim. Cosmochim. Acta. https://doi.org/10.1016/j.gca.2012.09.050

Alard, O., Lorand, J.P., Reisberg, L., Bodinier, J.L., Dautria, J.M., O'reilly, S.Y., 2011. Volatile-rich metasomatism in montferrier xenoliths (Southern France): Implications for the abundances of chalcophile and highly siderophile elements in the subcontinental mantle. J. Petrol. https://doi.org/10.1093/petrology/egr038

Arai, S., 1994. Characterization of spinel peridotites by olivine-spinel compositional relationships: review and interpretation. Chem. Geol. 113, 191–204.

Aulbach, S., Mungall, J.E., Pearson, D.G.G., 2016. Distribution and Processing of Highly Siderophile Elements in Cratonic Mantle Lithosphere. Rev. Mineral. Geochemistry 81, 239–304. https://doi.org/10.2138/rmg.2016.81.5

Beccaluva, L., Azzouni-Sekkal, A., Benhallou, A., Bianchini, G., Ellam, R.M., Marzola, M., Siena, F., Stuart, F.M., 2007. Intracratonic asthenosphere upwelling and lithosphere rejuvenation beneath the Hoggar swell (Algeria): Evidence from HIMU metasomatised lherzolite mantle xenoliths. Earth Planet. Sci. Lett. https://doi.org/10.1016/j.epsl.2007.05.047

Beccaluva, L., Bianchini, G., Ellam, R.M., Marzola, M., Oun, K.M., Siena, F., Stuart, F.M., 2008. The role of HIMU metasomatic components in the North African lithospheric mantle: petrological evidence from the Gharyan lherzolite xenoliths, NW Libya. Geol. Soc. London, Spec. Publ. 293, 253–277. https://doi.org/10.1144/SP293.12

Beccaluva, L., Bonadiman, C., Coltorti, M., Salvini, L., Siena, F., 2001. Depletion events, nature of metasomatizing agent and timing of enrichment processes in lithospheric mantle xenoliths from the Veneto Volcanic Province. J. Petrol. 42, 173–188.

Bianchini, G., Beccaluva, L., Bonadiman, C., Nowell, G., Pearson, G., Siena, F., Wilson, M., 2007. Evidence of diverse depletion and metasomatic events in harzburgite–lherzolite mantle xenoliths from the Iberian plate (Olot, NE Spain): Implications for lithosphere accretionary processes. Lithos 94, 25–45. https://doi.org/10.1016/j.lithos.2006.06.008

Bodinier, J.L., Menzies, M.A., Shimizu, N., Frey, F.A., McPherson, E., 2004. Silicate, Hydrous and Carbonate Metasomatism at Lherz, France: Contemporaneous Derivatives of Silicate Melt-Harzburgite Reaction. J. Petrol. 45, 299–320. https://doi.org/10.1093/petrology/egg107

Bodinier, J.L., Vasseur, G., Vernieres, J., Dupuy, C., Fabries, J., 1990. Mechanisms of mantle metasomatism: Geochemical evidence from the lherz orogenic peridotite. J. Petrol. 31, 597–628. https://doi.org/10.1093/petrology/31.3.597

Bonadiman, C., Beccaluva, L., Coltorti, M., Siena, F., 2005. Kimberlite-like metasomatism and "garnet signature" in spinel-peridotite xenoliths from Sal, Cape Verde Archipelago: Relics of a subcontinental mantle domain within the Atlantic oceanic lithosphere? J. Petrol. https://doi.org/10.1093/petrology/egi061

Borghini, G., Rampone, E., Zanetti, A., Class, C., Cipriani, A., Hofmann, A.W., Goldstein, S.L., 2013. Meter-scale Nd isotopic heterogeneity in pyroxenite-bearing ligurian peridotites encompasses global-scale upper mantle variability. Geology 41, 1055–1058. https://doi.org/10.1130/G34438.1

Bragagni, A., Luguet, A., Fonseca, R.O.C., Pearson, D.G., Lorand, J.P., Nowell, G.M., Kjarsgaard, B.A., 2017. The geological record of base metal sulfides in the cratonic mantle: A microscale 187Os/188Os study of peridotite xenoliths from Somerset Island, Rae Craton (Canada). Geochim. Cosmochim. Acta. https://doi.org/10.1016/j.gca.2017.04.015

Burton, K.W., Gannoun, A., Birck, J.-L., Allègre, C.J., Schiano, P., Clocchiatti, R., Alard, O., 2002. The compatibility of rhenium and osmium in natural olivine and their behaviour during mantle melting and basalt genesis. Earth Planet. Sci. Lett. 198, 63–76. https://doi.org/10.1016/S0012-821X(02)00518-6

Burton, K.W., Schiano, P., Birck, J.-L., Allègre, C.J., 1999. Osmium isotope disequilibrium between mantle minerals in a spinel-lherzolite. Earth Planet. Sci. Lett. 172, 311–322. https://doi.org/10.1016/S0012-821X(99)00207-1

Burton, K.W., Schiano, P., Birck, J.L., Allègre, C.J., Rehkämper, M., Halliday, A.N., Dawson, J.B., 2000. The distribution and behaviour of rhenium and osmium amongst mantle minerals and the age of the lithospheric mantle beneath Tanzania. Earth Planet. Sci. Lett. 183, 93–106. https://doi.org/10.1016/S0012-821X(00)00259-4

Cannatelli, C., 2012. Multi-stage metasomatism in the lithosphere beneath the Veneto Volcanic Province (VVP, Northern Italy). Mineral. Petrol. 104, 177–195. https://doi.org/10.1007/s00710-011-0185-3

Carlson, R.W., Pearson, D.G., Boyd, F.R., Shirey, S.B., Irvine, G., Menzies, A.H., Gurney, J.J., 1999. Re–Os systematics of lithospheric peridotites: implications for

lithosphere formation and preservation, in: Proceedings of the 7th International Kimberlite Conference. Red Roof Design Cape Town, pp. 99–108.

Carpenter, R.L., Edgar, A.D., Thibault, Y., 2002. Origin of spongy textures in clinopyroxene and spinel from mantle xenoliths, Hessian Depression, Germany. Mineral. Petrol. 74, 149–162. https://doi.org/10.1007/s007100200002

Chen, Y., Zhang, Y., Graham, D., Su, S., Deng, J., 2007. Geochemistry of Cenozoic basalts and mantle xenoliths in Northeast China. Lithos. https://doi.org/10.1016/j.lithos.2006.09.015

Choi, S.H., Kwon, S.T., Mukasa, S.B., Sagong, H., 2005. Sr-Nd-Pb isotope and trace element systematics of mantle xenoliths from Late Cenozoic alkaline lavas, South Korea. Chem. Geol. https://doi.org/10.1016/j.chemgeo.2005.04.008

Dobosi, G., Downes, H., Embey-Isztin, A., Jenner, G.A., 2003. Origin of megacrysts and pyroxenite xenoliths from the Pliocene alkali basalts of the Pannonian Basin (Hungary). Neues Jahrb. für Mineral. - Abhandlungen. https://doi.org/10.1127/0077-7757/2003/0178-0217

Downes, H., 2002. Formation and Modification of the Shallow Sub-continental Lithospheric Mantle: a Review of Geochemical Evidence from Ultramafic Xenolith Suites and Tectonically Emplaced Ultramafic Massifs of Western and Central Europe. J. Petrol. https://doi.org/10.1093/petrology/42.1.233

Emry, E.L., Shen, Y., Nyblade, A.A., Flinders, A., Bao, X., 2019. Upper Mantle Earth Structure in Africa From Full-Wave Ambient Noise Tomography. Geochemistry, Geophys. Geosystems 20, 120–147.

Fabriès, J., Lorand, J.P., Guiraund, M., 2001. Petrogenesis of the amphibole-rich veins from the Lherz orogenic Iherzolite Massif (Eastern Pyrenees, France): A case study for the origin of orthopyroxene-bearing amphibole pyroxenites in the lithospheric mantle. Contrib. to Mineral. Petrol. 140, 383–403. https://doi.org/10.1007/s004100000132

Foden, J.D., Elburg, M.A., Turner, S.P., Sandiford, M., O'Callaghan, J., Mitchell, S., 2008. Granite production in the Delamerian Orogen, South Australia. J. Geol. Soc. London. https://doi.org/10.1144/0016-764901-099

Frezzotti, M.L., Andersen, T., Neumann, E.R., Simonsen, S.L., 2002. Carbonatite melt-CO2 fluid inclusions in mantle xenoliths from Tenerife, Canary Islands: A story of trapping, immiscibility and fluid-rock interaction in the upper mantle. Lithos. https://doi.org/10.1016/S0024-4937(02)00178-0

Gao, S., Rudnick, R.L., Carlson, R.W., McDonough, W.F., Liu, Y.S., 2002. Re-Os evidence for replacement of ancient mantle lithosphere beneath the North China craton. Earth Planet. Sci. Lett. https://doi.org/10.1016/S0012-821X(02)00489-2

Griffin, W.L., Graham, S., O'Reilly, S.Y., Pearson, N.J., 2004. Lithosphere evolution beneath the Kaapvaal Craton: Re-Os systematics of sulfides in mantle-derived peridotites, in: Chemical Geology. https://doi.org/10.1016/j.chemgeo.2004.04.007

Harvey, J., Dale, C.W., Gannoun, A., Burton, K.W., 2011. Osmium mass balance in peridotite and the effects of mantle-derived sulphides on basalt petrogenesis. Geochim. Cosmochim. Acta. https://doi.org/10.1016/j.gca.2011.07.001

Harvey, J., Gannoun, A., Burton, K.W., Schiano, P., Rogers, N.W., Alard, O., 2010. Unravelling the effects of melt depletion and secondary infiltration on mantle Re-Os isotopes beneath the French Massif Central. Geochim. Cosmochim. Acta 74, 293–320. https://doi.org/10.1016/j.gca.2009.09.031

Harvey, J., Warren, J.M., Shirey, S.B., 2016. Mantle Sulfides and their Role in Re–Os and Pb Isotope Geochronology. Rev. Mineral. Geochemistry 81, 579–649. https://doi.org/10.2138/rmg.2016.81.10

Hofmann, A.W., 1988. Chemical differentiation of the Earth: the relationship between mantle, continental crust, and oceanic crust. Earth Planet. Sci. Lett. 90, 297–314. https://doi.org/10.1016/0012-821X(88)90132-X

Ionov, D.A., Hofmann, A.W., Shimizu, N., 1994. Metasomatism-induced melting in mantle xenoliths from Mongolia. J. Petrol. https://doi.org/10.1093/petrology/35.3.753

Irvine, G.J., Pearson, D.G., Kjarsgaard, B.A., Carlson, R.W., Kopylova, M.G., Dreibus, G., 2003. A Re–Os isotope and PGE study of kimberlite-derived peridotite xenoliths from Somerset Island and a comparison to the Slave and Kaapvaal cratons. Lithos. https://doi.org/10.1016/S0024-4937(03)00126-9

Kamenetsky, M.B., Sobolev, A. V., Kamenetsky, V.S., Maas, R., Danyushevsky, L. V., Thomas, R., Pokhilenko, N.P., Sobolev, N. V., 2004. Kimberlite melts rich in alkali chlorides and carbonates: A potent metasomatic agent in the mantle. Geology. https://doi.org/10.1130/G20821.1

Karlstrom, K.E., Daniel, C.G., 1993. Restoration of Laramide right-lateral strike slip in northern New Mexico by using Proterozoic piercing points: tectonic implications from the Proterozoic to the Cenozoic. Geology. https://doi.org/10.1130/0091-7613(1993)021<1139:ROLRLS>2.3.CO;2

Lee, C.A., 2005. Trace Element Evidence for Hydrous Metasomatism at the Base of the North American Lithosphere and Possible Association with Laramide Low-Angle Subduction. J. Geol. https://doi.org/10.1086/449327

Leighton, M.W., Eidel, J.J., Kolata, D.R., Oltz, D.F., 1990. Geology of interior cratonic sag basins. AAPG Bull. (American Assoc. Pet. Geol. 74.

Li, J., Hou, G., Huang, X.N., Zhang, Z.Q., Qian, X.L., 2001. The constraint for the supercontinental cycles: Evidence from precambrian geology of North China Block, Acta Petrologica Sinica.

Li, J., Qian, X.L., Huang, X.N., Liu, S., 2000. Tectonic framework of North China Block and its cratonization in the early Precambrian, Acta Petrologica Sinica. https://doi.org/10.1515/9783110800715.1

Li, Z.X.A., Lee, C.T.A., Peslier, A.H., Lenardic, A., Mackwell, S.J., 2008. Water contents in mantle xenoliths from the Colorado Plateau and vicinity: Implications

for the mantle rheology and hydration-induced thinning of continental lithosphere. J. Geophys. Res. Solid Earth. https://doi.org/10.1029/2007JB005540

Liégeois, J.P., Abdelsalam, M.G., Ennih, N., Ouabadi, A., 2013. Metacraton: Nature, genesis and behavior. Gondwana Res. https://doi.org/10.1016/j.gr.2012.02.016

Lucassen, F., Franz, G., Romer, R.L., Dulski, P., 2008. Late Cenozoic xenoliths as a guide to the chemical isotopic composition and thermal state of the upper mantle under northeast Africa. Eur. J. Mineral. https://doi.org/10.1127/0935-1221/2008/0020-1855

Luck, J.M., Allègre, C.J., 1983. 187Re-187Os systematics in meteorites and cosmochemical consequences. Nature. https://doi.org/10.1038/302130a0

Lustrino, M., Wilson, M., 2007. The circum-Mediterranean anorogenic Cenozoic igneous province. Earth-Science Rev. 81, 1–65. https://doi.org/10.1016/j.earscirev.2006.09.002

Macgregor, D.S., 1996. The hydrocarbon systems of North Africa. Mar. Pet. Geol. 13, 329–340. https://doi.org/10.1016/0264-8172(95)00068-2

Marchesi, C., Griffin, W.L., Garrido, C.J., Bodinier, J.L., O'Reilly, S.Y., Pearson, N.J., 2010. Persistence of mantle lithospheric Re-Os signature during asthenospherization of the subcontinental lithospheric mantle: Insights from in situ isotopic analysis of sulfides from the Ronda peridotite (Southern Spain). Contrib. to Mineral. Petrol. https://doi.org/10.1007/s00410-009-0429-y

Matsumoto, T., Honda, M., McDougall, I., O'Reilly, S.Y., Norman, M., Yaxley, G., 2000. Noble gases in pyroxenites and metasomatised peridotites from the Newer Volcanics, southeastern Australia: Implications for mantle metasomatism. Chem. Geol. https://doi.org/10.1016/S0009-2541(00)00181-9

Matsumoto, T., Pinti, D.L., Matsuda, J.I., Umino, S., 2002. Recycled noble gas and nitrogen in the subcontinental lithospheric mantle: Implications from N-He-Ar in fluid inclusions of SE Australian xenoliths. Geochem. J. https://doi.org/10.2343/geochemj.36.209

McDonough, W.F., and Sun, S.-S., 1995, The composition of the Earth: Chemical geology, v. 120, p. 223–253.

McPherson, E., Thirlwall, M.F., Parkinson, I.J., Menzies, M. a., Bodinier, J.L., Woodland, A., Bussod, G., 1996. Geochemistry of metasomatism adjacent to amphibole-bearing veins in the Lherz peridotite massif. Chem. Geol. 134, 135–157. https://doi.org/10.1016/S0009-2541(96)00084-8

Medaris, L.G., Beard, B.L., Johnson, C.M., Valley, J.W., Spicuzza, M.J., Jelínek, E., Mísâr, Z., 1995. Garnet pyroxenite and eclogite in the Bohemian Massif: geochemical evidence for Variscan recycling of subducted lithosphere. Geol. Rundschau. https://doi.org/10.1007/BF00284516

Meisel, T., Moser, J., Wegscheider, W., 2001a. Recognizing heterogeneous distribution of platinum group elements (PGE) in geological materials by means of the Re-Os

isotope system. Fresenius. J. Anal. Chem. 370, 566–572. https://doi.org/10.1007/s002160100791

Meisel, T., Walker, R.J., Irving, A.J., Lorand, J.P., 2001b. Osmium isotopic compositions of mantle xenoliths: A global perspective. Geochim. Cosmochim. Acta. https://doi.org/10.1016/S0016-7037(00)00566-4

Meisel, T., Walker, R.J., Morgan, J.W., 1996. The osmium isotopic composition of the Earth's primitive upper mantle. Nature. https://doi.org/10.1038/383517a0

Miller, C., Zanetti, A., Thöni, M., Konzett, J., Klötzli, U., 2012. Mafic and silica-rich glasses in mantle xenoliths from Wau-en-Namus, Libya: Textural and geochemical evidence for peridotite-melt reactions. Lithos 128–131, 11–26. https://doi.org/10.1016/j.lithos.2011.11.004

Mukasa, S.B., Shervais, J.W., Wilshire, H.G., Nielson, J.E., 1991. Intrinsic Nd, Pb, and Sr Isotopic Heterogeneities Exhibited by the Lherz Alpine Peridotite Massif, French Pyrenees. J. Petrol. Special_Vo, 117–134. https://doi.org/10.1093/petrology/Special_Volume.2.117

Natali, C., Beccaluva, L., Bianchini, G., Ellam, R.M., Siena, F., Stuart, F.M., 2013. Carbonated alkali-silicate metasomatism in the North Africa lithosphere: Evidence from Middle Atlas spinel-lherzolites, Morocco. J. South Am. Earth Sci. https://doi.org/10.1016/j.jsames.2012.06.014

Niu, Y.L., 1997. Mantle melting and melt extraction processes beneath ocean ridges: Evidence from abyssal peridotites. J. Petrol. 38, 1047–1074. https://doi.org/10.1093/petrology/38.8.1047

Pearce, J. A., Barker, P.F., Edwards, S.J., Parkinson, I.J., Leat, P.T., 2000. Geochemistry and tectonic significance of peridotites from the South Sandwich arc-basin system, South Atlantic. Contrib. to Mineral. Petrol. https://doi.org/10.1007/s004100050572

Pearce, John A, Robinson, R.B., Subramanian, R., 2000. Strategic management: Formulation, implementation, and control. Irwin/McGraw-Hill Columbus, OH.

Pearson, D.G., Carlson, R.W., Shirey, S.B., Boyd, F.R., Nixon, P.H., 1995. Stabilisation of Archaean lithospheric mantle: A Re{single bond}Os isotope study of peridotite xenoliths from the Kaapvaal craton. Earth Planet. Sci. Lett. https://doi.org/10.1016/0012-821X(95)00125-V

Pearson, D.G., Irvine, G.J., Ionov, D.A., Boyd, F.R., Dreibus, G.E., 2004. Re-Os isotope systematics and platinum group element fractionation during mantle melt extraction: A study of massif and xenolith peridotite suites, in: Chemical Geology. https://doi.org/10.1016/j.chemgeo.2004.04.005

Puziewicz, J., Matusiak-Małek, M., Ntaflos, T., Grégoire, M., Kukuła, A., 2015. Subcontinental lithospheric mantle beneath Central Europe. Int. J. Earth Sci. 104, 1913–1924.

Rudnick, R.L., Gao, S., Ling, W.L., Liu, Y.S., McDonough, W.F., 2004. Petrology and geochemistry of spinel peridotite xenoliths from Hannuoba and Qixia, North China craton. Lithos. https://doi.org/10.1016/j.lithos.2004.03.033

Santos, J.F., Schärer, U., Ibarguchi, J.I.G., Girardeau, J., 2002. Genesis of pyroxenite-rich peridotite at Cabo Ortegal (NW Spain): Geochemical and Pb-Sr-Nd isotope data. J. Petrol. 43, 17–43. https://doi.org/10.1093/petrology/43.1.17

Schandelmeier, H., 1988. Pre-Cretaceous intraplate basins of NE Africa. Episodes 11, 270–274.

Shirey, S.B., Walker, R.J., 1998. The Re-Os isotope system in cosmochemistry and high-temperature geochemistry. Annu. Rev. Earth Planet. Sci. 26, 423–500. https://doi.org/10.1146/annurev.earth.26.1.423

Smoliar, M.I., Walker, R.J., Morgan, J.W., 1996. Re-Os ages of group IIA, IIIA, IVA, and IVB iron meteorites. Science (80-.). 271, 1099–1102. https://doi.org/10.1126/science.271.5252.1099

Stracke, A., Hofmann, A.W., Hart, S.R., 2005. FOZO, HIMU, and the rest of the mantle zoo. Geochemistry, Geophys. Geosystems 6, n/a-n/a. https://doi.org/10.1029/2004GC000824

Su, B.X., Zhang, H.F., Sakyi, P.A., Yang, Y.H., Ying, J.F., Tang, Y.J., Qin, K.Z., Xiao, Y., Zhao, X.M., Mao, Q., Ma, Y.G., 2011. The origin of spongy texture in minerals of mantle xenoliths from the Western Qinling, central China. Contrib. to Mineral. Petrol. https://doi.org/10.1007/s00410-010-0543-x

van Acken, D., Becker, H., Walker, R.J., McDonough, W.F., Wombacher, F., Ash, R.D., Piccoli, P.M., 2010. Formation of pyroxenite layers in the Totalp ultramafic massif (Swiss Alps) – Insights from highly siderophile elements and Os isotopes. Geochim. Cosmochim. Acta 74, 661–683. https://doi.org/10.1016/j.gca.2009.10.007

Wainwright, A., 2015. Dating Early Archean partial melting events: insights from Re-Os dating of micrometric Os-minerals from Kalahari Craton mantle xenoliths.

Walker, R.J., Horan, M.F., Morgan, J.W., Becker, H., Grossman, J.N., Rubin, A.E., 2002. Comparative 187Re-187Os systematics of chondrites: Implications regarding early solar system processes. Geochim. Cosmochim. Acta. https://doi.org/10.1016/S0016-7037(02)01003-7

Walker, R.J., Morgan, J.W., 1989. Rhenium-osmium isotope systematics of carbonaceous chondrites. Science (80-.). https://doi.org/10.1126/science.243.4890.519

Wang, K.L., O'Reilly, S.Y., Griffin, W.L., Pearson, N.J., Zhang, M., 2009. Sulfides in mantle peridotites from Penghu Islands, Taiwan: Melt percolation, PGE fractionation, and the lithospheric evolution of the South China block. Geochim. Cosmochim. Acta. https://doi.org/10.1016/j.gca.2009.04.030

Witt-Eickschen, G., Kramm, U., 1998. Evidence for the multiple stage evolution of the subcontinental lithospheric mantle beneath the Eifel (Germany) from pyroxenite

and composite pyroxenite/peridotite xenoliths. Contrib. to Mineral. Petrol. 131, 258–272.

Witt-Eickschen, G., Seck, H. a., Mezger, K., Eggins, S.M., Altherr, R., 2003. Lithospheric Mantle Evolution beneath the Eifel (Germany): Constraints from Sr-Nd-Pb Isotopes and Trace Element Abundances in Spinel Peridotite and Pyroxenite Xenoliths. J. Petrol. 44, 1077–1095. https://doi.org/10.1093/petrology/44.6.1077

WittEickschen, G., Kramm, U., Witt-Eickschen, G., Kramm, U., 1997. Mantle upwelling and metasomatism beneath Central Europe: geochemical and isotopic constraints from mantle xenoliths from the Rhön (Germany). Journal of Petrology . J. Petrol. 38 SRC-, 479–493. https://doi.org/10.1093/petrology/38.4.479

Wittig, N., Baker, J.A., Downes, H., 2007. U-Th-Pb and Lu-Hf isotopic constraints on the evolution of sub-continental lithospheric mantle, French Massif Central. Geochim. Cosmochim. Acta. https://doi.org/10.1016/j.gca.2006.11.025

Wittig, N., Pearson, D.G., Baker, J.A., Duggen, S., Hoernle, K., 2010. A major element, PGE and Re-Os isotope study of Middle Atlas (Morocco) peridotite xenoliths: evidence for coupled introduction of metasomatic sulphides and clinopyroxene. Lithos 115 SRC-, 15–26.

Xu, Y., 2002. Evidence for crustal components in the mantle and constraints on crustal recycling mechanisms: Pyroxenite xenoliths from Hannuoba, North China. Chem. Geol. https://doi.org/10.1016/S0009-2541(01)00300-X

Ying, J., Zhang, H., Kita, N., Morishita, Y., Shimoda, G., 2006. Nature and evolution of Late Cretaceous lithospheric mantle beneath the eastern North China Craton: Constraints from petrology and geochemistry of peridotitic xenoliths from Jünan, Shandong Province, China. Earth Planet. Sci. Lett. https://doi.org/10.1016/j.epsl.2006.02.023

Yoshikawa, M., Nakamura, E., 2000. Geochemical evolution of the Horoman peridotite complex: Implications for melt extraction, metasomatism, and compositional layering in the mantle. J. Geophys. Res. 105, 2879. https://doi.org/10.1029/1999JB900344

Zhao, G., Cawood, P.A., Wilde, S.A., Sun, M., Lu, L., 2000. Metamorphism of basement rocks in the Central Zone of the North China Craton: implications for Paleoproterozoic tectonic evolution. Precambrian Res. 103 SRC-, 55–88.

Zheng, J., O'Reilly, S.Y., Griffin, W.L., Lu, F., Zhang, M., Pearson, N.J., 2001. Relict refractory mantle beneath the eastern North China block: Significance for lithosphere evolution. Lithos. https://doi.org/10.1016/S0024-4937(00)00073-6

Zhou, M., Robinson, P., Malpas, J., Li, Z., 1996. Podiform chromitites in the Loubusa ophiolite (Southern Tibet): Implications for melt-rock interaction and chromite segregation in the upper mantle. J. Petrol. v 37 SRC-, 3–21.

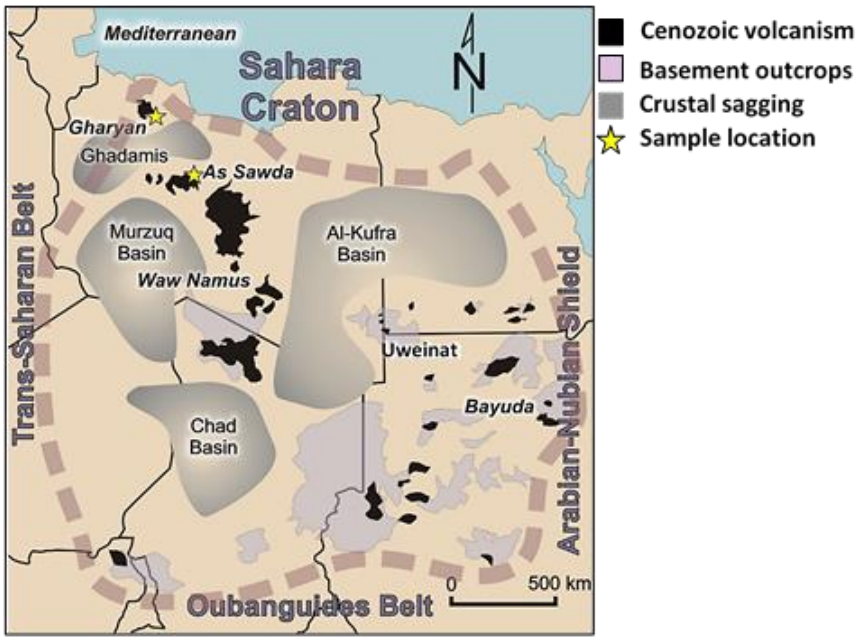

Figure 2.1 Map showing the major Cenozoic volcanic fields, crustal rocks reworked and intruded during the Pan-African collisions, and the major sag basins within the Sahara Craton.

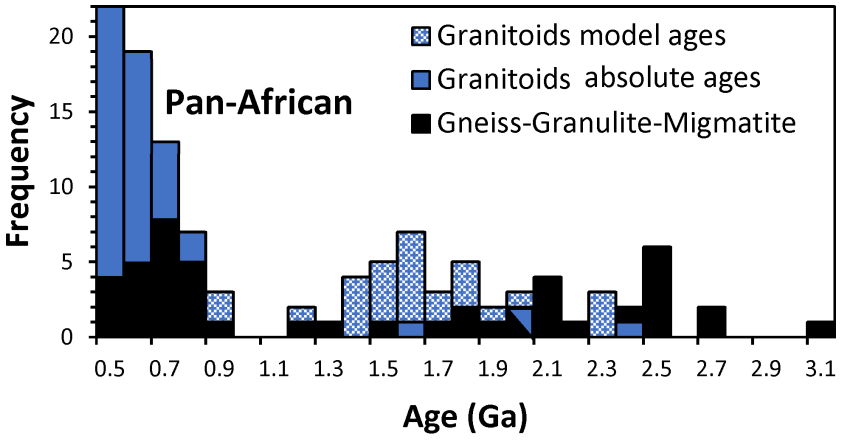

Figure 2.2 Histogram representation of crustal rock ages in the Sahara, N. Africa (Rb/Sr, Sm/Nd, and Zircon U/Pb ages). Data from Abdelsalam et al. (2002) and references therein.

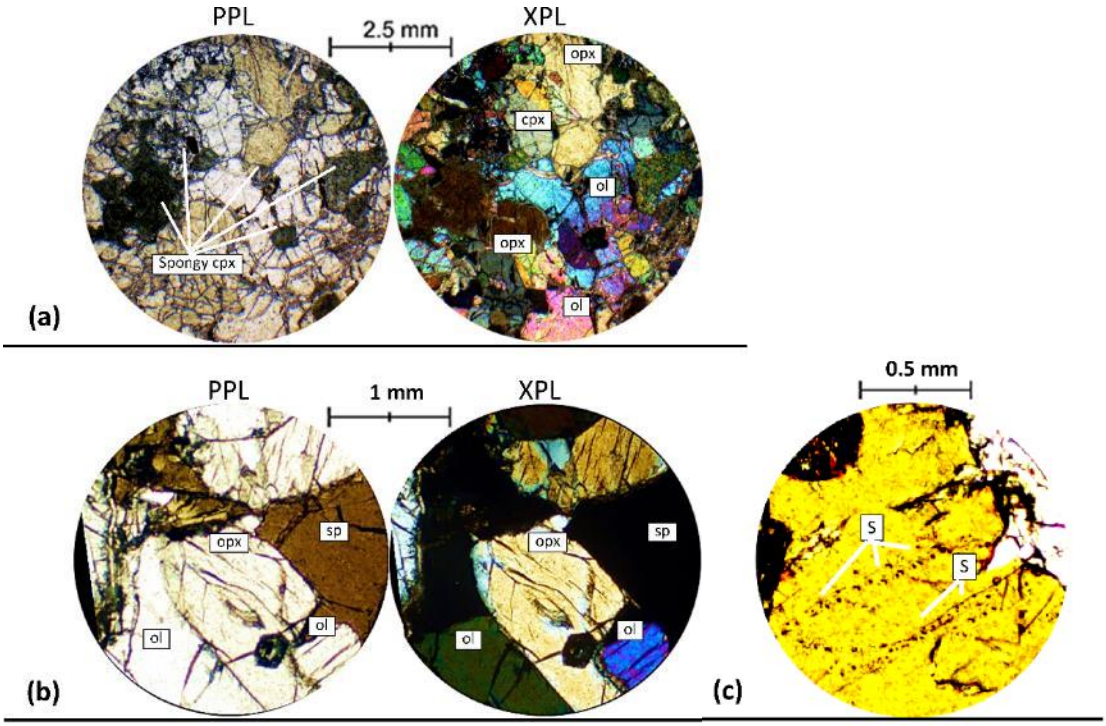

Figure 2.3 Photomicrographs of representative textures and mineralogy of the studied xenoliths. **a)** Metasomatic reactions of aggregate clinopyroxene surrounded destabilized orthopyroxene [GH-9 in plane and cross polarized light]. **b)** Typical granoblastic texture of spinel-peridotite [GH-26 in-plane and cross polarized light]. **c)** Transmitted light image of spinel showing enclosed trails of minute sulfide grains [JS-14]. cpx: clinopyroxene, opx: orthopyroxene, ol: olivine, s: sulfides.

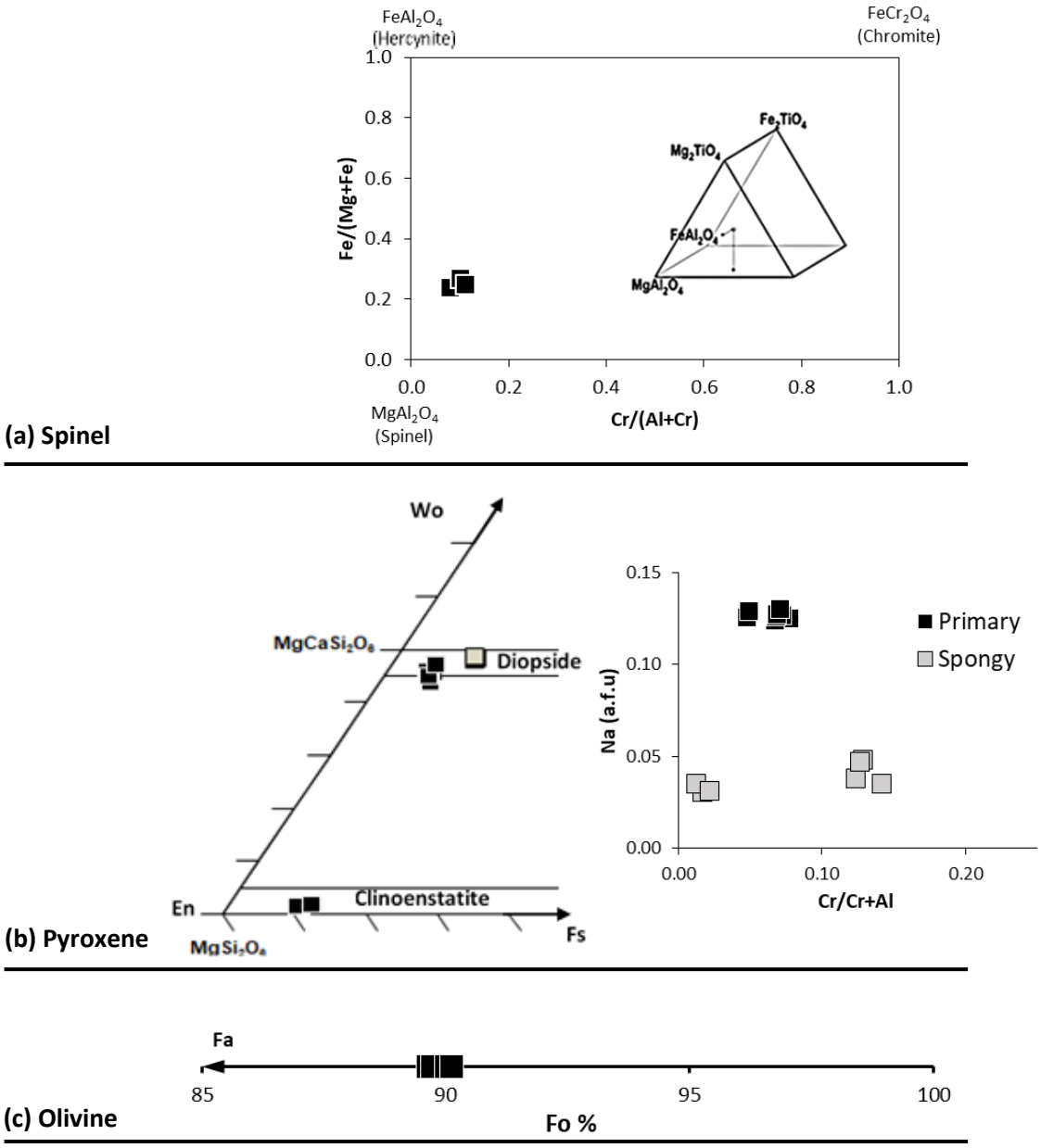

Figure 2.4 Chemical compositions of xenoliths-forming minerals. **a)** Spinel compositions projected onto the base of the spinel prism. **b)** Wollastonite (Wo)–enstatite (En)– ferrosilite (Fs) classification diagram for pyroxenes and Na vs. Cr/(Al+Cr) for clinopyroxene in atoms per formula units (a.f.u.). **c)** Olivine compositions expressed as % forsterite (Fo).

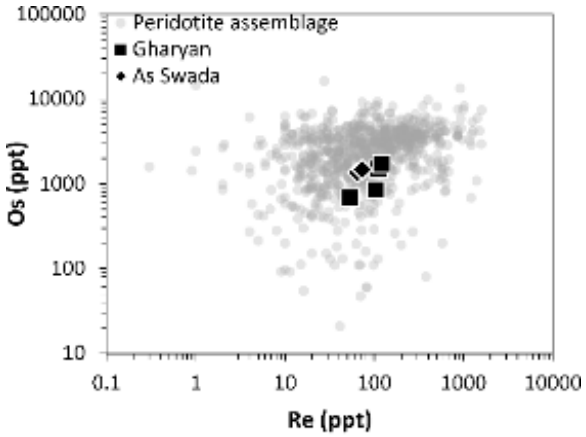

Figure 2.5 Bulk-rock Re and Os concentrations of the studied xenoliths and all available analyses of peridotite assemblage in the GEOROC database (http://georoc.mpch-mainz.gwdg.de/georoc/).

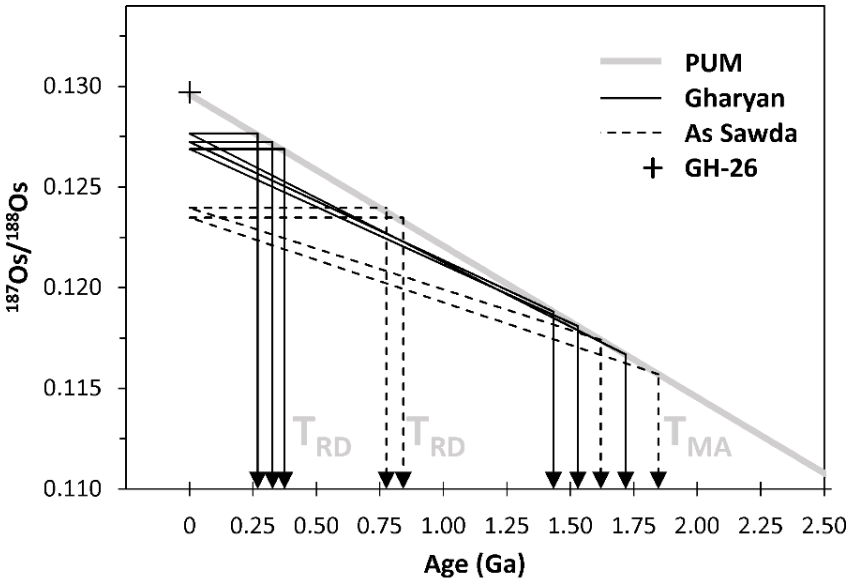

Figure 2.6 Graphical representation of the calculated T_{MA} and T_{RD} model ages of Gharyan and As Sawda xenoliths. Using the absolute age of 4.558 Ga and the most primitive initial $^{187}Os/^{188}Os$ ratio defined for early Solar System (IIIA irons meteorite $^{187}Os/^{188}Os$ = 0.09531, Smoliar et al., 1996) as starting composition for the present-day average of the primitive upper mantle PUM evolution curve ($^{187}Os/^{188}Os$ =0.1296, Meisel et al., 2001b).

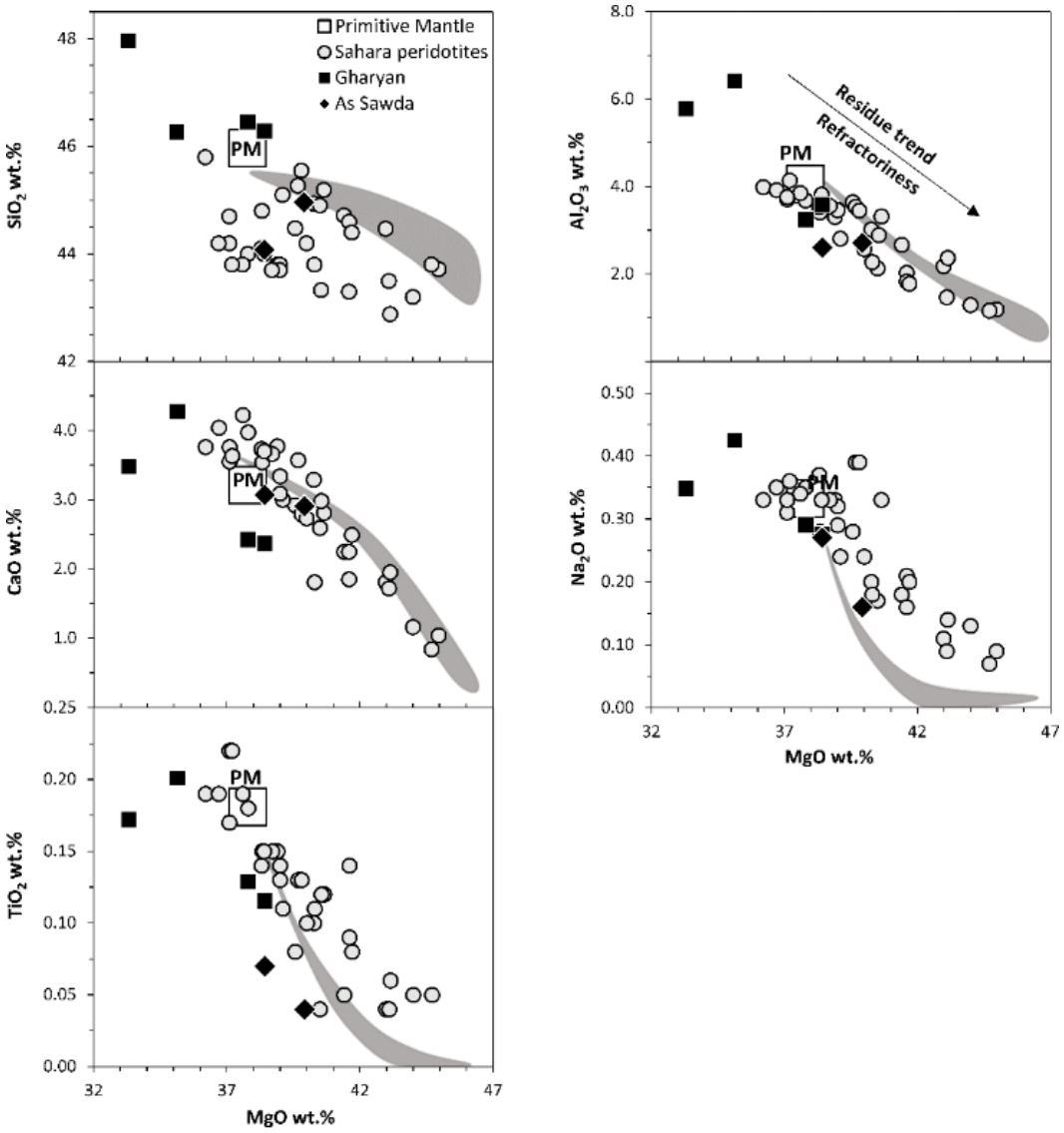

Figure 2.7 Bulk-rock compositions of Gharyan and As Sawda xenoliths compared to the composition of the primitive mantle (PM; Hofmann, 1988). Also shown are residual trends after melt extraction from a primitive mantle composition (Niu, 1997). Sahara peridotite data are from Beccaluva et al. (2008); Lucassen et al. (2008); Miller et al. (2012).

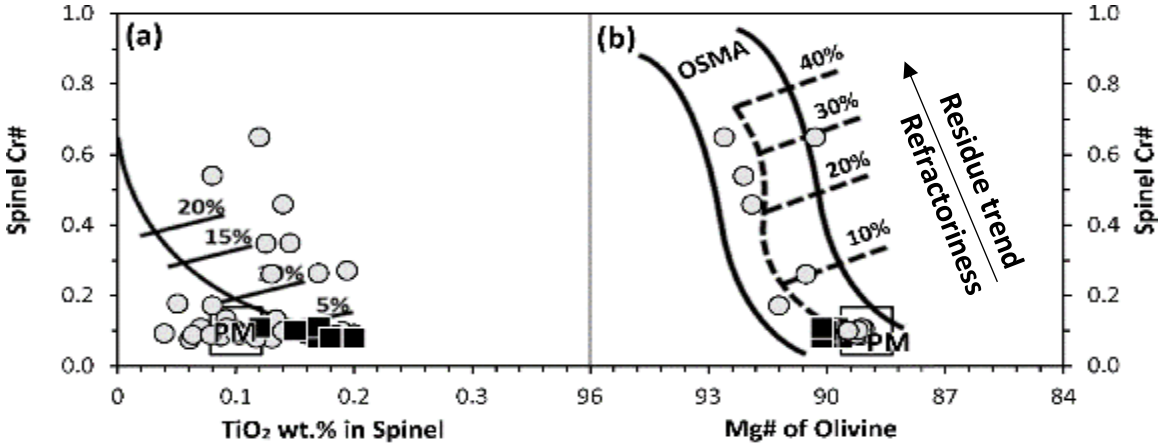

Figure 2.8 Mantle depletion trends. **a)** Cr# [Cr/(Al+Cr)] vs. TiO_2 in spinel. **b)** Olivine-Spinel Mantle Array (OSMA) of Arai (1994), Olivine Mg# [100*Mg/(Mg+Fe^{2+})]. The residual trend in the SCLM is labeled with % of melt extraction. Primitive mantle (PM) data are from Pearce et al. (2000). Symbols and data sources as in Figure 3.7.

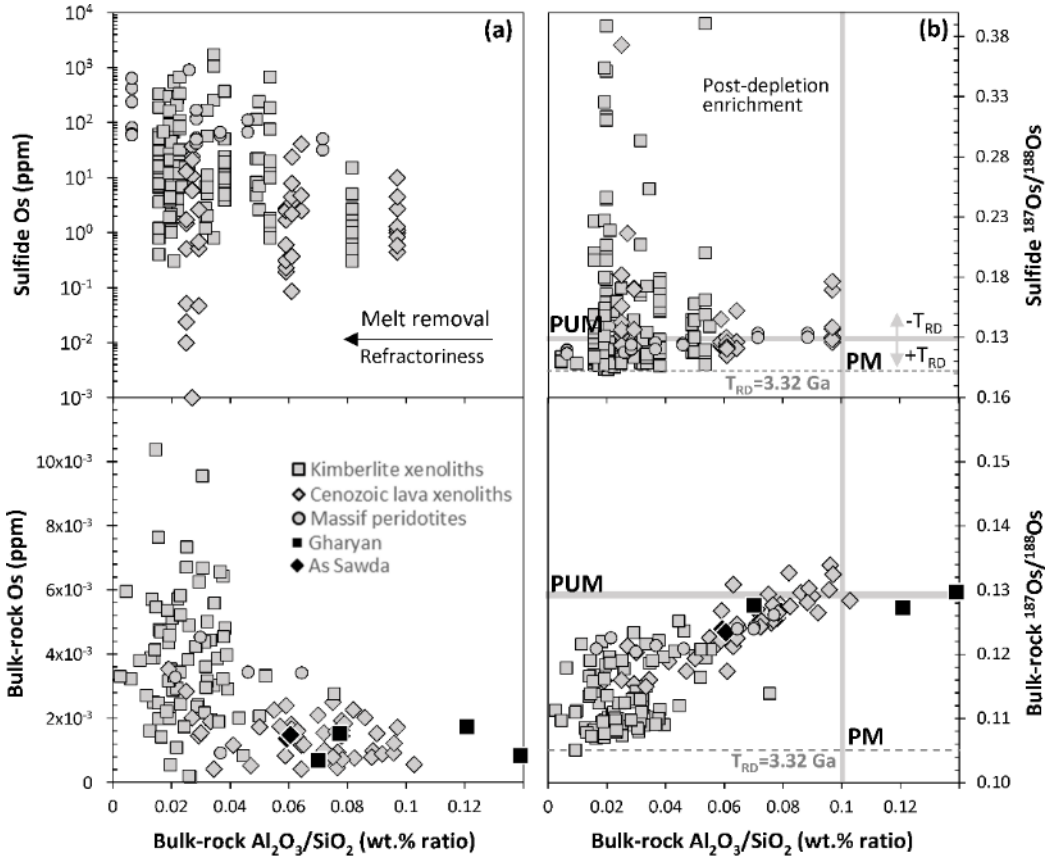

Figure 2.9 Os systematics of peridotite assemblages compiled from xenoliths in kimberlites and Cenozoic lavas and massif peridotites. **a)** Sulfide and bulk-rock Os concentrations in ppm. **b)** Sulfide and bulk-rock $^{187}Os/^{188}Os$ ratios. Primitive mantle (PM) and primitive upper mantle (PUM) parameters are $Al_2O_3/SiO_2 = 0.1$ and $^{187}Os/^{188}Os = 0.1296$, respectively (McDonough and Sun, 1995; Meisel et al., 2001b). Bulk-rock and in situ analyses are from (Bragagni et al., 2017; Griffin et al., 2004; Harvey et al., 2011, 2010; Irvine et al., 2003; Marchesi et al., 2010; Pearson et al., 2004; Wainwright, 2015).

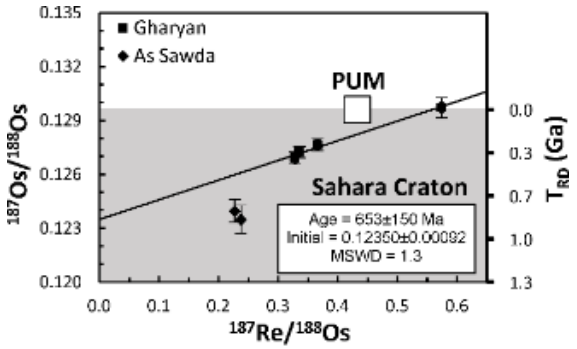

Figure 2.10 Bulk-rock $^{187}Os/^{188}Os$ and $^{187}Re/^{188}Os$ analysis of the Sahara Craton peridotites. The regression (MSWD =1.3) of Gharyan locality produces an age of 653 Ma. Age calculated using ISOPLOT model 4.15 and a value of $1.666x10^{-11}$ for the decay constant of ^{187}Re yielding ±95%-conf. on 4 points. The shaded area is the $^{187}Os/^{188}Os$ range measured in global peridotites from Meisel et al. (2001b). Isotopic ratios of the primitive upper mantle (PUM) are $^{187}Os/^{188}Os$ =0.1296 and $^{187}Re/^{188}Os$=0.433.

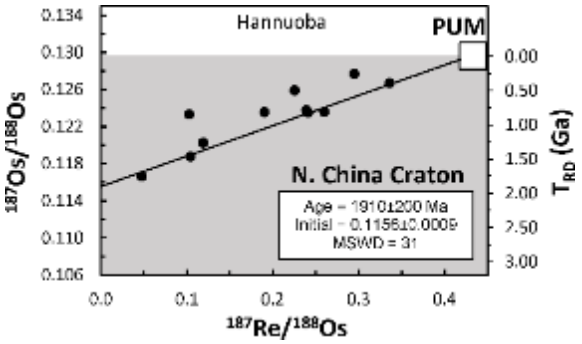

Figure 2.11 Bulk-rock $^{187}Os/^{188}Os$ and $^{187}Re/^{188}Os$ analysis of Hannuoba peridotites, North China Craton. The data are from Gao et al. (2002). The shaded area is the $^{187}Os/^{188}Os$ range measured in global peridotites from Meisel et al. (2001b). Isotopic ratios of the primitive upper mantle (PUM) are $^{187}Os/^{188}Os$ =0.1296 and $^{187}Re/^{188}Os$=0.433.

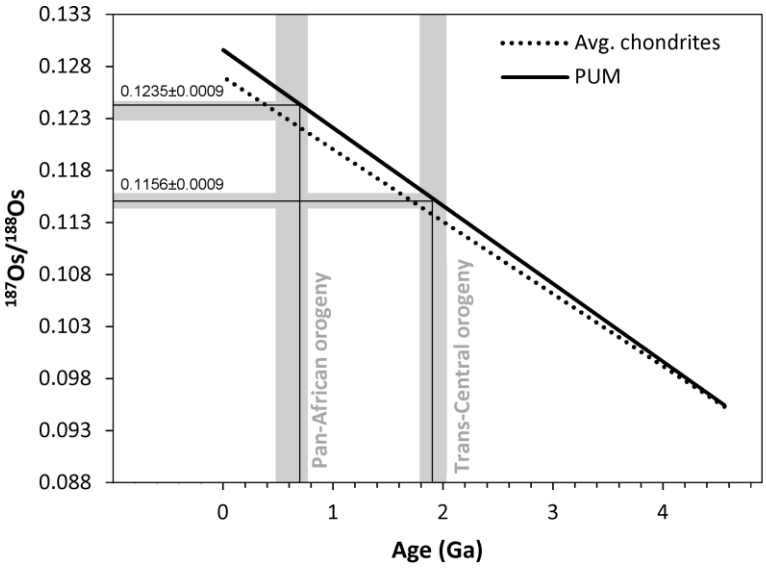

Figure 2.12 Mantle evolution of today $^{187}Os/^{188}Os$ ratio between the average chondrite composition ($^{187}Os/^{188}Os$ = 0.1270, Luck and Allègre, 1983; Walker and Morgan, 1989) and the estimate of the primitive upper mantle PUM ($^{187}Os/^{188}Os$ = 0.1296, Meisel et al., 2001b), using the absolute age of 4.558 Ga and the most primitive initial $^{187}Os/^{188}Os$ ratio defined for early Solar System (IIIA irons meteorite with initial $^{187}Os/^{188}Os$ of 0.09531, Smoliar et al., 1996). Also showing the initial ratios and ages of the Sahara and North China Craton isochrones.

Table 2.1 Bulk-rock analysis of the Sahara xenoliths.

Sample	GH-26	GH-9	GH-12	GH-13	A-4	JS-14	JS-10
Major oxides (%)							
SiO_2	46.26	46.45	46.28	47.96	45.36	44.08	44.96
TiO_2	0.20	0.13	0.12	0.17	0.14	0.07	0.04
Al_2O_3	6.43	3.25	3.58	5.79	4.78	2.61	2.27
Fe_2O_3T	7.95	8.74	9.00	8.66	7.77	8.10	7.86
MnO	0.12	0.12	0.13	0.13	0.14	0.13	0.12
MgO	35.13	37.79	38.42	33.3	36.79	38.42	39.92
CaO	4.27	2.43	2.37	3.48	3.93	3.07	2.91
Na_2O	0.42	0.29	0.28	0.35	0.28	0.27	0.16
K_2O	n.d.	0.01	0.07	0.02	0.05	0.07	0.01
LOI		1.3					
Modal composition (%)							
sp	6	2	<1	1	2	2	2
ol	38	51	47	59	63	62	61
opx	37	31	38	23	20	24	28
cpx	19	16	15	16	15	12	9

ol, olivine; opx, orthopyroxene; cpx, clinopyroxene; sp, spinel.

Table 2.2 Average microprobe analyses of orthopyroxene.

	Orthopyroxene								
Sample (Label)	GH-26^{A26X-a}	GH-26^{B26X-b}	GH-26^{B26X-c}	A-4^{B22X-r}	GH-9^{B22X-c}	GH-9^{B22X-b}	GH-12^{A42-c}	GH-12^{A42-m}	GH-12^{A42-r}
n	4	2	2	6	3	3	2	4	2
SiO_2	54.44	54.68	54.93	54.46	55.19	54.69	55.08	56.04	55.99
TiO_2	0.14	0.15	0.15	0.16	0.14	0.16	0.13	0.14	0.11
Al_2O_3	5.45	5.51	5.49	5.46	4.79	5.39	4.58	2.52	2.57
Cr_2O_3	0.31	0.32	0.30	0.36	0.27	0.36	0.31	0.19	0.22
Fe_2O_3*	0.57		0.17	0.24	0.10	0.57	0.28	0.15	
FeO	5.86	6.43	6.37	6.14	6.26	6.00	5.97	7.42	7.45
MnO	0.12	0.14	0.16	0.12	0.14	0.17	0.13	0.19	0.23
MgO	32.28	32.09	32.34	32.19	32.59	32.37	32.74	32.42	32.25
CaO	0.83	0.82	0.81	0.84	0.74	0.86	0.73	0.87	0.89
Na_2O	0.14	0.14	0.13	0.12	0.14	0.12	0.12	0.13	0.12
Total	100.15	100.27	100.86	100.08	100.37	100.68	100.08	100.09	99.82
Cations									
Si	1.88	1.89	1.88	1.88	1.90	1.88	1.90	1.94	1.95
Ti	0.004	0.004	0.004	0.004	0.004	0.004	0.003	0.004	0.003
Al	0.22	0.22	0.22	0.22	0.19	0.22	0.19	0.10	0.11
Cr	0.01	0.01	0.01	0.01	0.01	0.01	0.01	0.01	0.01
Fe^{3+}	0.015		0.004	0.006	0.003	0.015	0.007	0.004	
Fe^{2+}	0.17	0.19	0.18	0.18	0.18	0.17	0.17	0.22	0.22
Mn	0.004	0.004	0.005	0.004	0.004	0.005	0.004	0.006	0.007
Mg	1.66	1.65	1.65	1.66	1.67	1.66	1.68	1.68	1.67
Ca	0.03	0.03	0.03	0.03	0.03	0.03	0.03	0.03	0.03
Na	0.01	0.01	0.01	0.01	0.01	0.01	0.01	0.01	0.01
Tot. cat.	4	4	4	4	4	4	4	4	4
Tot. oxy.	6	6	6	6	6	6	6	6	6
$Mg/Fe^{2+}+Mg$	0.90	0.90	0.90	0.90	0.90	0.90	0.90	0.88	0.89
Cr/Cr+Al	0.04	0.04	0.04	0.04	0.04	0.04	0.04	0.05	0.05
Wo %	1.63	1.61	1.59	1.65	1.46	1.68	1.42	1.67	1.72
En %	88.39	88.25	88.19	88.37	88.63	88.12	88.91	86.70	86.71
Fs %	9.97	10.14	10.22	9.97	9.91	10.20	9.67	11.63	11.58

*Fe^{+3} estimated from charge balance. *n*: number of individual spot analyses. Wollastonite (Wo)–enstatite (En)– ferrosilite (Fs).

Table 2.3 Average microprobe analyses of olivine.

	Olivine								
Sample (Label)	GH-26^{B26X-a}	GH-26^{B26X-b}	GH-26^{B26X-c}	GH-9^{B22X-c}	GH-9^{B22X-b}	A-4^{B22X-r}	GH-12^{A16-c}	GH-12^{A16-m}	GH-12^{A16-r}
n	4	4	4	4	4	4	4	4	4
SiO_2	40.89	40.87	40.92	40.74	40.94	40.75	42.84	42.84	40.75
TiO_2	0.02	0.02	0.01			0.02			0.02
Cr_2O_3	0.02		0.01	0.01	0.03	0.02	0.01	0.01	0.02
Fe_2O_3*	0.02			0.25	0.33				
FeO	9.89	9.87	9.92	9.39	9.53	9.38	9.82	9.82	9.38
MnO	0.13	0.15	0.15	0.13	0.22	0.14	0.17	0.17	0.14
MgO	49.04	48.69	48.91	49.12	49.28	48.73	50.49	50.49	48.73
CaO	0.06	0.05	0.07	0.11	0.07	0.14	0.07	0.07	0.14
NiO	0.35	0.31	0.36	0.34	0.41	0.36	0.32	0.32	0.36
Total	100.07	99.64	99.98	99.75	100.40	99.17	103.40	103.40	99.17
Cations									
Si	1.00	1.00	1.00	1.00	1.00	1.00	1.01	1.01	1.00
Ti	0.0003	0.0003	0.0002			0.0003			0.0003
Cr	0.0003		0.0001	0.0002	0.0005	0.0004	0.0002	0.0002	0.0004
Fe^{3+}	0.0005			0.0046	0.0060				
Fe^{2+}	0.20	0.20	0.20	0.19	0.19	0.19	0.19	0.19	0.19
Mn	0.003	0.003	0.003	0.003	0.005	0.003	0.003	0.003	0.003
Mg	1.79	1.78	1.78	1.79	1.79	1.79	1.78	1.78	1.79
Ca	0.001	0.001	0.002	0.003	0.002	0.004	0.002	0.002	0.004
Ni	0.01	0.01	0.01	0.01	0.01	0.01	0.01	0.01	0.01
Tot. cat.	3	3	3	3	3	3	3	3	3
Tot. oxy.	4	4	4	4	4	4	4	4	4
Fo%	89.69	89.65	89.65	89.98	89.73	90.13	90.01	90.01	90.13

*Fe^{+3} estimated from charge balance. Fo: forsterite component = 100 x Mg/(Mg + Fe). *n*: number of individual spot analyses.

Table 2.4 Average microprobe analyses of spinel.

	Spinel											
Sample (Label)	GH-26^{B26X-a}	GH-26^{A26X-b}	GH-26^{B26X-c}	GH-12^{B23X-c}	GH-12^{B23X-m}	GH-12^{B23X-r}	A-4^{B42X-c}	A-4^{B42X-m}	A-4^{B42X-r}	GH-9^{B22X-c}	GH-9^{B22X-a}	A-4^{B22X-r}
n	4	4	4	4	4	4	4	4	4	4	4	4
TiO_2	0.18	0.17	0.21	0.20	0.15	0.18	0.15	0.12	0.12	0.17	0.20	0.12
Al_2O_3	59.60	59.72	58.91	59.47	57.38	59.84	57.38	57.51	57.33	57.17	57.06	57.04
Cr_2O_3	7.67	7.75	8.15	7.72	9.55	7.58	9.55	9.53	9.49	10.35	10.47	10.39
Fe_2O_3*	1.84	1.96	2.15	1.84	2.41	1.69	2.41	2.35	2.57	1.88	1.63	1.80
FeO	9.74	9.90	9.68	9.68	10.67	9.95	10.67	10.67	10.54	9.95	10.17	10.09
MnO	0.10	0.09	0.11	0.07	0.08	0.11	0.08	0.13	0.14	0.12	0.08	0.12
MgO	20.50	20.49	20.49	20.54	19.69	20.42	19.69	19.69	19.74	20.12	20.01	19.95
NiO	0.42	0.44	0.40	0.39	0.46	0.39	0.46	0.42	0.41	0.40	0.36	0.38
Total	99.63	100.09	99.70	99.51	99.93	99.78	99.93	100.01	99.94	99.76	99.61	99.52
Cations												
Ti	0.004	0.003	0.004	0.004	0.003	0.004	0.003	0.002	0.002	0.003	0.004	0.002
Al	1.80	1.80	1.78	1.80	1.75	1.81	1.75	1.75	1.75	1.74	1.75	1.75
Cr	0.16	0.16	0.17	0.16	0.20	0.15	0.20	0.20	0.19	0.21	0.21	0.21
Fe^{3+}	0.04	0.04	0.04	0.04	0.05	0.03	0.05	0.05	0.05	0.04	0.03	0.04
Fe^{2+}	0.21	0.21	0.21	0.21	0.23	0.21	0.23	0.23	0.23	0.22	0.22	0.22
Mn	0.002	0.002	0.002	0.002	0.002	0.002	0.002	0.003	0.003	0.003	0.002	0.003
Mg	0.78	0.78	0.79	0.79	0.76	0.78	0.76	0.76	0.76	0.78	0.77	0.77
Ni	0.01	0.01	0.01	0.01	0.01	0.01	0.01	0.01	0.01	0.01	0.01	0.01
Tot. cat.	3	3	3	3	3	3	3	3	3	3	3	3
Tot. oxy.	4	4	4	4	4	4	4	4	4	4	4	4
$Fe^{+2}/Fe^{+2}+Mg$	0.24	0.24	0.24	0.24	0.27	0.24	0.27	0.27	0.27	0.25	0.25	0.25
Cr/Cr+Al	0.08	0.08	0.08	0.08	0.10	0.08	0.10	0.10	0.10	0.11	0.11	0.11
$Mg/Fe^{+2}+Mg$	0.78	0.79	0.79	0.79	0.77	0.79	0.77	0.77	0.77	0.78	0.78	0.78

*Fe^{+3} estimated from charge balance. *n*: number of individual spot analyses.

Table 2.5 Average microprobe analyses of clinopyroxene.

	Clinopyroxene								
Sample (Label)	GH-9^{A22X-c}	GH-9^{A22X-a}	GH-26^{A26-a}	GH-26^{A26-b}	GH-12^{B22X-c}	A-4^{B22X-m}	GH-12^{B22X-r}	GH-9^{A22X-b}	GH-26^{A26-c}
n	3	3	3	4	3	3	3	3	8
SiO_2	51.47	51.71	53.66	53.44	52.10	51.86	51.92	51.37	52.62
TiO_2	0.62	0.59	0.42	0.42	0.47	0.50	0.54	0.61	0.47
Al_2O_3	7.54	7.44	4.61	4.67	6.58	6.66	6.86	7.54	3.07
Cr_2O_3	0.59	0.58	0.57	0.54	0.70	0.73	0.70	0.63	0.64
Fe_2O_3*	2.27	1.89	1.65	1.63	1.91	2.33	2.11	2.14	1.18
FeO	1.17	1.66	2.43	2.49	1.38	1.19	1.14	1.45	2.65
MnO	0.08	0.08	0.15	0.12	0.08	0.06	0.09	0.08	0.08
MgO	15.19	15.10	15.91	15.81	15.40	15.31	15.18	15.15	15.21
CaO	19.66	19.59	19.71	19.57	19.95	19.87	19.90	19.47	22.75
Na_2O	1.85	1.85	1.80	1.81	1.78	1.82	1.89	1.83	1.83
Total	100.44	100.50	100.91	100.52	100.35	100.33	100.35	100.27	100.50
Cations									
Si	1.85	1.86	1.92	1.92	1.87	1.87	1.87	1.85	1.92
Ti	0.02	0.02	0.01	0.01	0.01	0.01	0.01	0.02	0.01
Al	0.32	0.32	0.19	0.20	0.28	0.28	0.29	0.32	0.13
Cr	0.02	0.02	0.02	0.02	0.02	0.02	0.02	0.02	0.02
Fe^{3+}	0.06	0.05	0.04	0.04	0.05	0.06	0.06	0.06	0.03
Fe^{2+}	0.04	0.05	0.07	0.08	0.04	0.04	0.03	0.04	0.08
Mn	0.002	0.002	0.005	0.004	0.002	0.002	0.003	0.002	0.04
Mg	0.81	0.81	0.85	0.85	0.83	0.82	0.81	0.81	0.88
Ca	0.76	0.75	0.76	0.75	0.77	0.77	0.77	0.75	0.89
Na	0.129	0.125	0.129	0.125	0.127	0.124	0.126	0.127	0.123
Tot. cat.	4	4	4	4	4	4	4	4	4
Tot. oxy.	6	6	6	6	6	6	6	6	6
Cr/Cr+Al	0.05	0.05	0.08	0.07	0.07	0.07	0.06	0.05	0.12
Mg/Fe^{2+}+Mg	0.96	0.94	0.92	0.92	0.95	0.96	0.96	0.95	0.92
Wo %	45.34	45.27	43.79	43.73	45.50	45.38	45.79	45.02	47.09
En %	48.76	48.55	49.17	49.17	48.87	48.68	48.62	48.77	46.71
Fs %	5.90	6.18	7.04	7.10	5.63	5.94	5.60	6.20	6.20

*Fe^{+3} estimated from charge balance. *n*: number of individual spot analyses. Wollastonite (Wo)–enstatite (En)– ferrosilite (Fs).

Table 2.6 Representative microprobe analyses of spongy clinopyroxene.

	Spongy Clinopyroxene						
Sample (Label)	GH-26^{A26}	GH-26^{A27}	GH-26^{A28}	GH-26^{A29}	A-4$^{B22X\text{-}m}$	A-4$^{B22X\text{-}m}$	A-4$^{B22X\text{-}m}$
SiO_2	52.62	52.96	52.75	52.92	53.39	53.09	53.56
TiO_2	0.47	0.44	0.45	0.47	0.09	0.30	0.13
Al_2O_3	3.07	2.74	3.46	3.54	1.54	2.25	1.74
Cr_2O_3	0.64	0.67	0.76	0.76	0.04	0.04	0.06
Fe_2O_3*	1.18	1.05	1.27	0.88	0.63	0.49	0.53
FeO	2.65	2.80	2.40	2.79	6.26	6.43	6.23
MnO	0.13	0.11	0.11	0.14	0.06	0.05	0.06
MgO	16.21	16.71	16.65	16.55	14.30	14.03	14.27
CaO	22.75	22.41	21.93	21.97	23.52	23.40	23.72
Na_2O	0.54	0.50	0.69	0.67	0.43	0.49	0.44
total	100.27	100.38	100.46	100.70	100.26	100.57	100.73
cations							
Si	1.92	1.92	1.91	1.91	1.97	1.95	1.97
Ti	0.01	0.01	0.01	0.01	0.00	0.01	0.00
Al	0.13	0.12	0.15	0.15	0.07	0.10	0.08
Cr	0.02	0.02	0.02	0.02	0.00	0.00	0.00
Fe^{3+}	0.03	0.03	0.03	0.02	0.02	0.01	0.01
Fe^{2+}	0.08	0.09	0.07	0.08	0.19	0.20	0.19
Mn	0.004	0.003	0.003	0.004	0.002	0.002	0.002
Mg	0.88	0.90	0.90	0.89	0.79	0.77	0.78
Ca	0.89	0.87	0.85	0.85	0.93	0.92	0.93
Na	0.038	0.035	0.048	0.047	0.031	0.035	0.031
tot. cat.	4	4	4	4	4	4	4
tot. oxy.	6	6	6	6	6	6	6
Cr/Cr+Al	0.12	0.14	0.13	0.13	0.02	0.01	0.02
Mg/Fe^{2+}+Mg	0.92	0.91	0.93	0.91	0.80	0.80	0.80
Wo %	47.09	46.05	45.74	45.87	48.21	48.43	48.56
En %	46.71	47.78	48.33	48.08	40.79	40.41	40.64
Fs %	6.20	6.17	5.93	6.05	11.00	11.17	10.80

Wollastonite (Wo)–enstatite (En)– ferrosilite (Fs).

Table 2.7 Bulk-rock Re-Os isotope measurements.

Sample	Locality	Os (ppt)	$^{187}Os/^{188}Os$	Re (ppt)	$^{187}Re/^{188}Os$	T_{MA} (Ma)	T_{RD} (Ma)
GH-26	Gharyan	843.6±1.18	0.12971±0.00057	103.65±2.06	0.57416	46*	-15*
GH-9	Gharyan	686.51±1.15	0.12766±0.00034	53.75±2.06	0.36602	1717	268
GH-12	Gharyan	1511.78±1.35	0.12689±0.00033	112.07±2.18	0.32796	1529	374
GH-13	Gharyan	1737.05±1.30	0.12724±0.00032	120.83±2.01	0.33524	1433	326
JS-14	As Sawda	1363.23±1.20	0.12397±0.00063	64.26±2.00	0.22708	1619	775
JS-10	As Sawda	1479.14±1.30	0.12349±0.00078	72.9±2.00	0.23735	1846	841

Model ages are calculated using the primitive upper mantle (PUM) of Meisel et al. (2001b).
*Sample GH-26 has a similar PUM evolution trajectory that exceeds the present time $^{187}Os/^{188}O$ (PUM) by a fraction of 0.0001.

CHAPTER 3

The Chronologic Link between Orogeny-Modified Lithosphere and Postorogenic Lavas: An application of Pyroxenite-Os Hyperbola

3.1 Introduction

Orogenic terrains are the most prominent features on a continent's surface. Typically, orogenic belts are linear or arcuate features stimulated by deformations accompanying collisional processes. Depending on the intensity of compressional tectonics, the crustal interiors can be modified by far-field stresses that lead to hot ductile belts and crustal magmatism, and metamorphism (Liégeois et al., 2013). Due to the subcrustal mantle's rheological properties (rigid mantle lithosphere), it is more likely for major orogenic movements to modify the whole lithosphere rather than just the crust. However, during the continental amalgamations (opening and closing oceans), whether the sub-continental lithospheric mantle (SCLM) is reworked or progressed by physical separation from the oceanic convection is challenging to ascertain (Carlson et al., 2005; Rollinson, 2010; Servali and Korenaga, 2018).

The volcanic activities that follow an orogenic cycle are generally defined as postorogenic or postcollisional volcanism. Geochemical studies vary in inferring the nature of the mantle involved in these lavas' petrogenesis. Studies using isotopes such as Sr, Nd, and Pb often differ in defining the mantle's physical identity. Plumes, asthenosphere, and enriched lithospheric mantle are all mantle types that have been suggested to be involved in continental basaltic volcanism. The diverse isotopic signatures found in the postorogenic lavas seem to require input from at least one old, isotopically-enriched source region that many authors identified as a hybrid SCLM (e.g.,

Mayer et al., 2014; Pilet et al., 2008). Therefore, the SCLM has come to be viewed as one of the mantle types with chemical characteristics suitable for the petrogenesis of postorogenic lavas.

In general, the SCLM is depleted and buoyant in isolation from the convection effects. However, post-depletion enrichment is the prevailing feature in SCLM, whether on- or off-craton settings. The changes are evident in peridotite assemblages, either cryptically or modally (e.g., Downes, 2002; Gibson et al., 2008). The timing and triggers of these enriching overprints are still not definitive. Another subordinate magmatic process in the uppermost mantle exists and is seen in orogenic peridotites and massifs. The least deformed are sufficiently well preserved to allow observations of structural relationships among the mantle assemblages. Cumulates such as pyroxenites are the dominant mantle assemblages. The secondary nature of the cumulate assemblages can be inferred from their modes of occurrence as layers and veins in cross-cutting relations hosted by peridotitic country rock (e.g., Bodinier et al., 1987; Mukasa et al., 1991; McPherson et al., 1996). Pyroxenites comprise around 10% of ultramafic lithologies exposed at the surface (Harvey et al., 2016). Several hypotheses have been proposed for mantle pyroxenites, mostly discussed as high-pressure cumulates that segregate from asthenosphere-derived melt percolating the lithosphere (Takahashi, 1992; Pearson et al., 1993; Becker, 1996; Garrido and Bodinier, 1999).

Isotopic systems that can trace chronologic and petrogenetic aspects of the SCLM are invaluable tools. The Re-Os system is one such tool. Unlike the other isotopic systems, the efficiency emanates from the Os siderophile nature and the distinct $^{187}Os/^{188}Os$ ratio in pyroxenites. However, suppose the SCLM has a direct relationship

with assemblages exhumed in orogenic terranes. In that case, that relationship should be reflected in the petrogenesis of postorogenic volcanism by carrying signatures of mineralogic and isotopic changes in the SCLM since the time of continental collisions. Therefore, in analogy with the pyroxenite-Os hyperbola, Os sampled by postorogenic induced melt is assessed isotopically and chronologically in the context of SCLM secondary lithologies.

3.2 Postorogenic lavas

The Earth's orogenic cycles can be as early as Archaean to Paleoproterozoic time, such as N China blocks' amalgamation (2000-1800 Ma, Zhao, 2001), or throughout younger and successive cycles, whereas some orogenies could be sporadic but synchronous. For instance, in the circum-Mediterranean region, the age of orogenic belts extends from ~600 Ma (Pan African) to ages as young as 200-300 Ma, represented by the Hercynian or the Variscan orogeny (Figure 3.1). With chronological overlap, the Appalachian orogeny in N America is usually seen as equivalent to the Hercynian orogeny in Europe. However, small and sparse lava fields that mainly erupted in the Cenozoic time exist in almost every continent. A characteristic of these fields is that they are surrounded by orogenic belts that possess crustal magmatism and metamorphism, with absolute ages clustering around the time of the continental collisions. Henceforth, a compilation of whole-rock analyses of Cenozoic volcanism emplaced within the regions shown in Figure 3.1 is presented in Figure 3.2. For the consistency with the physiography of terrestrial surface, plots of incompatible elements (HFS or LIL elements) and Pb isotopes vs. wt.% MgO are grouped into lavas associated with massif uplifts and oceanic

bulges and extrusives that erupted through extensional stresses and reactivation of ancient structural dislocations.

The HFS and LIL elements of the extension-related lavas have positive correlations with MgO wt.% (Figure 3.2a). The compiled dataset consists of alkaline and tholeiitic compositions with Al_2O_3/SiO_2 wt.% ratio ranges from 0.16 to 0.4. The decrease of Zr and Nb concentrations decreasing MgO wt.% does not comply with fractional crystallization, although some subsets from individual volcanic fields show low-pressure fractional crystallization trends stemming from parental compositions. The Zr and Nb depletion and other incompatible trace elements are distinctive features in the tholeiites. The lavas with little MgO have low Pb isotopic ratios. In this respect, the spectrum from alkaline to tholeiitic compositions cannot be justified by any igneous process other than mixing, showing two end-members enriched in HFS and LIL elements and another depleted and less radiogenic in Pb.

Compositions of Canary Islands, Hoggar, Massif Central, and Bohemian lavas are predominantly alkaline with scarce tholeiitic compositions and Al_2O_3/SiO_2 (wt.% ratio) 0.14-0.5 (Figure 3.2b). Their localities are characterized by contemporaneous basement uplifts and seismic low-velocity anomalies. The trace element systematics and Pb isotopes of basalts at the continental swells of Massif Central, Bohemian Massif, and Hoggar agree with the Canary Islands hotspot's data, suggesting the involvement of a deeper mantle component (plume-induced lavas, Lustrino and Wilson, 2007). Though Zr and Nb's negative correlations with MgO might suggest liquid-line-of-descent trends involving fractional removal of crystallizing olivine, clinopyroxene, and plagioclase, fractional crystallization alone would not affect Pb isotopic ratios of lavas.

3.3 Data

About 210 samples of Cenozoic basalts with Re-Os analyses acquired from the literature, including eight new samples from the Sahara, are presented in Figure 3.3 (localities and analytical procedure of the new samples are provided in the APPENDIX-A). The Os and Re concentrations are very variable. They extend to values up to 0.667 and 2.548 ppb, respectively. The Re abundances tend to be higher than Os in most samples where the Re/Os ratio is >1. The variability between Re and Os per sample can be as high as three orders of magnitude difference, ranging from 10^{-1} to 10^{2} ppb. There is no consistency or correlation between Re and Os in terms of magmatic series or sample locality. Also, no apparent variations can relate Re and Os with major elements such as Al_2O_3, SiO_2, or MgO. Although the latter's spectrum extends to more than 20 wt.% in compositions such as nephelinites and melilites, the Re and Os data do not show strong consistency or correlation. Instead, the Os concentrations become less variable and confined < 0.1 ppb, and the Re/Os ratio is the highest when MgO is relatively low (MgO < 10 wt.%, Figure 3.3).

3.4 Discussion

3.4.1 Os systematics in the mantle and induced melt

Unlike the lithophile elements, the Os partitioning among the mantle-forming minerals is unique. The siderophile chemical affinity imposes a vast amount of mantle-Os budget to partition in non-silicates, such as sulfides (e.g., pyrrhotite, pentlandite, and chalcopyrite) and oxides (e.g., chromite). Although the non-silicate phase such as sulfides has modal abundance estimated in a system dominated by silicate and alumina minerals such as the mantle to be less than one vol% (Harvey et al., 2016), Os concentrations can

be up to three orders of magnitude in ppb and ppm levels (Griffin et al., 2004; Aulbach et al., 2016). The contrast is remarkably high with the alumina and silicate phases 1000 times less than sulfides in sub-ppb levels (Burton et al., 2000; Harvey et al., 2010, 2011). Texturally, sulfides are immiscible micron- and micrometer-scale grains and blebs that are either interstitial or partially or entirely enclosed within the mantle silicate and alumina minerals (Lorand, 1989; Burton et al., 2000; Harvey et al., 2010, 2011). Showing the Os nugget nature and concentration levels, compilations of whole-rock Al_2O_3/SiO_2 (wt.% ratio) representing the mantle-forming minerals are used in a bivariate relation with *in-situ* analyses of Os-hosted sulfides and are presented in Figure 3.4.

As a primary SCLM lithology, peridotites have a record of melt removal, reflecting on the composition and proportions of the forming minerals. The Al_2O_3/SiO_2 (wt.% ratio) decreases from lherzolitic to harzburgitic assemblages. As a siderophile element, the high $K_d^{Os}{}_{\text{sulfide/silicate}}$ of 10^5–10^6 wields Os to be partitioned in sulfides (Harvey et al., 2016). Sulfide-Os inversely increases with bulk Al_2O_3/SiO_2 ratio. The Os concentrations' difference is up to four orders of magnitude for a single population within the same sample or less primeval compositions (10^3-10^6 ppb, Figure 3.4a). However, concentration levels as low as 10^0 ppb contradict the Os compatibility nature and become more pronounced in the most refractory or depleted compositions. These low-Os sulfides are commonly ascribed as post-depletion enrichment or populations introduced by "metasomatism" (Griffin et al., 2004; Wang et al., 2009; Harvey et al., 2010; Alard et al., 2011). On the other hand, sulfide-Os concentrations tend to be relatively lower in pyroxenites (10^1-10^3 ppb, Figure 3.4b). Given the abundance of their constituents cumulate minerals, the Al_2O_3/SiO_2 (wt.% ratio) exceeds the estimate of the Primitive

Mantle (PM) composition (> 0.098, Figure 3.4b). The ratio encompasses the entire spectrum measured in the postorogenic lavas Al_2O_3/SiO_2 (wt.% ratio). As a silicate melt, pyroxenites appear to exert chemical controls on the source bulk composition that are not feasible in the presence of peridotitic compositions.

The major elements of pyroxenites are different from peridotites concerning their PM depletion. Exceeding the $(Al_2O_3/SiO_2)_{PM}$ ratio shows that pyroxenites are mantle-melt derived assemblages and secondary in origin. However, for the time-integrated depletion, the upper limit estimated for the PM is used to mark the unradiogenic Os in the compiled data ($^{187}Os/^{188}Os \leq 0.1296 \pm 8$, Meisel et al., 2001b, Figure 3.5). As a representation of Os partitioned in the assemblage-forming silicate and alumina minerals, the Os of whole-rock analyses (onward named silicate-Os) has levels as low as 10^{-2} ppb. The silicate-Os creates a contrast of fewer than eight orders of magnitude with the Os partitioned in sulfides (>10^6 ppb, Figure 3.5a), which is the typical concentration levels that are measured *in-situ* for individual silicate and alumina minerals (e.g., Burton et al., 2000; Harvey et al., 2011). The unradiogenic Os exists in both sulfides and silicates, whether the assemblage is peridotitic or pyroxenitic. The former's sulfide-Os can be very radiogenic, preferably with those having relatively lower Os concentrations, which is a prominent feature of the most depleted peridotitic assemblages (Figure 3.4a), indicating that the radiogenic Os is a post-depletion enrichment "metasomatism-sulfides." In contrast, pyroxenites have the most radiogenic silicate-Os measured in mantle assemblages. The isotopic ratios can be as high as 13 in cratonic settings (Harris et al., 2018) and relatively restricted in pyroxenite-hosted sulfides (Figure 3.5b). However, the Os isotope data for pyroxenite-hosted sulfides are limited. The reported ratios are either

unradiogenic ($^{187}Os/^{188}Os$= 0.1174, Wang et al., 2009) or marginally evolved to 0.1446 (Luguet et al., 2008).

By contrast, Os sampled by the postorogenic induced melt have isotopic ratios corrected for ^{187}Os due to the decay of ^{187}Re since the eruptions time (initial ratios). Thus, the isotopic composition represents the source or host at the moment of melting (time=0). The compiled data ranges from unradiogenic ratios (0.113) to ratios as high as 1.256 in disagreement with peridotites silicate-Os (Figure 3.5c). The isotopic growth of the peridotite silicate-Os agrees with the compositional depletion and the assemblage-forming minerals (Al_2O_3/SiO_2 wt.% ratio < 0.098, Figure 3.4a). Apart from the metasomatism-sulfides, almost all silicate-Os are unradiogenic (> 95% of the compiled data), showing that the time-integrated depletion remains intact within the Os partitioned in the silicate system. In agreement with the pyroxenite's bulk Al_2O_3/SiO_2 wt.% ratio (Figure 3.4b), Os sampled by postorogenic lavas has the same systematics as pyroxenite-Os in terms of concentrations and isotopic ratios (Figure 3.5c). However, as a highly compatible element, the $^{187}Os/^{188}Os$ ratio variability becomes significantly lower with an increased Os concentration in the induced melt, mostly unradiogenic. It is an inverse relationship defining a mixing end-member with a high Os content and low ^{187}Re-^{187}Os decay or growth rate.

3.4.2 Non-equilibrium Re phase

As a function of time, whether in silicates or sulfides, the Re content regulates Os isotopic growth. Therefore, considering the consistency of major elements and Os systematics between the postorogenic melt and pyroxenites (Figures 3.4 and 3.5), Re is coupled with Os as a ratio and correlated with Os isotopic ratios (Figure 3.6).

Similar to major elements, the Re/Os ratio of cumulated assemblages exceeds the $(Re/Os)_{PM}$ ratio ($\geq 0.08 \pm 0.05$, Figure 3.6a). On the one hand, the ratio directly correlates with the evolved $^{187}Os/^{188}Os$ ratio from unradiogenic to radiogenic compositions. It is consistent with the pyroxenites secondary nature, disclosing a re-equilibration between Re and Os among the forming minerals. On the other hand, despite the Os contrast between sulfides and silicates, the Re/Os ratios of pyroxenite-forming silicates and sulfides are indistinguishable. The ratio proximity shows that sulfides and silicates are in chemical equilibrium ($Re/Os < 10^0$, Figure 3.6a). However, a subset of the compiled data does not comply with $^{187}Os/^{188}Os$ ratios' long-term evolution. It is significantly elevated to two orders of magnitudes higher than the most evolved silicate-Os ($Re/Os \geq 10^4$ and $^{187}Os/^{188}Os \leq 0.2$, Figure 3.6a). It reveals an excess Re from a non-equilibrium mineral. Those assemblages are heterogeneous. They are amphibole-bearing pyroxenites with 5-42% of amphibole by volume (Tilhac et al., 2020).

As a dry assemblage in origin, the presence of hydrous overprints in pyroxenites can easily skew the Re budget without affecting the $^{187}Os/^{188}Os$ ratio's time-integrated growth. It shows that the hydrous minerals in the mantle can contrast the dry silicates-Re upon melting. Again, the Re/Os ratio of postorogenic induced melt is within the limits of pyroxenite assemblages (Figure 3.6b). It has a steady increase consistent with the Os isotopic growth from unradiogenic to radiogenic compositions. Additionally, coupling Re with Os reveals another mixing end-member analogous to the pyroxenite assemblages' non-equilibrium phase ($Re/Os \geq 10^2$ and $^{187}Os/^{188}Os \leq 0.2$, Figure 3.6b). The ratio variability is up to four orders of magnitude, discounting the $Re/Os < 10^0$ (Figure 3.6b). It

shows that Re and the Os have no affiliation in the induced melt, indicating the presence of an independent Re hydrous phase in the source lithology.

As the bulk-K_d governing the mantle's relation to the induced melt, experimental studies consistently show the incongruent melting and disappearance of hydrous phases from dry assemblages a few degrees above the solidus (Frost, 2006). Furthermore, the mantle assemblages from the orogenic peridotites and massifs display that disseminated hydrous silicates such as phlogopite, pargasite, or hornblendite veins are incompatible elements repositories with MgO up to 20 wt. % (e.g., McPherson et al., 1996; Fabriès et al., 2001; Bodinier et al., 2004). The compositional characteristics of hydrous silicates are consistent with the alkaline lava's incompatible elements' increased concentrations and high MgO wt.% (Figure 3.2), particularly in compositions such as nephelinites and melilites.

3.4.3 Pyroxenite-Os hyperbola and melt errorchrons

The postorogenic induced melt is not accordant with source lithology having the bulk peridotitic compositions. Instead, the melt is in chemical and isotopic equilibrium with pyroxenites' major elements and Os isotopes (Figures 3.4 and 3.5). As indicated by the various isotopic compositions, the induced melts can sample the variability and extreme mantle compositions (mixture), especially when the melting domain is larger than the mantle heterogeneity scale (e.g., Liu et al., 2008). For Os, the heterogeneity is within a micrometer scale. The difference can be six or seven orders of magnitude in Os content, depending on whether Os is partitioned in a non-silicate or silicate system (Figure 3.5). Given the pyroxenites secondary nature in the mantle, the ^{187}Os time-integrated growth since sulfide-silicate equilibration due to the decay of ^{187}Re are

recorded by the Os sampled by the postorogenic lavas at the moment of melting (Time =0). Consequently, different pyroxenites $^{187}Os/^{188}Os$ ratios are used to produce the mixing hyperbola in two independent components to constrain the time-integrated growth of Os sampled by the induced melt (equation and parameters details are provided in Appendix-B).

The selected $^{187}Os/^{188}Os$ ratios are within the ranges measured in pyroxenites-forming minerals and sulfides, which can be interchangeable with provisions to the limits. In the example shown in Figure 3.7a, the selected ratio is higher in silicate-Os (7.5) than in sulfides (0.13). The Os content ratio controls the hyperbola orientation and shape (e.g., $Os_{silicate}/Os_{sulfide}$). On a linear scale, the hyperbola is angular down when the Os contrast between the two components is six orders of magnitudes ($Os_C/Os_D = 10^{-6}$, Figure 3.7a). The hyperbola equation is transformable into a straight line when the x-coordinate is reciprocals of Os concentrations (1/Os ppb^{-1}, Figure 3.7b). As a result, the selected $^{187}Os/^{188}Os$ ratio of silicate-Os are anchored by the selected sulfide-Os' isotopic ratio.

The Os sampled by the postorogenic induced melt is consistent with the pyroxenite's hyperbola (Figure 3.7c), showing a simple mixing line between silicates and sulfides. Accordingly, the $^{187}Re–^{187}Os$ isotope evolution since pyroxenites sulfide-silicate equilibration is recorded by the induced melt (time=0). Nonetheless, the isotope ^{188}Os is non-radiogenic Os. The naturally occurring abundance of ^{188}Os is 13.29 compositional % (Shirey and Walker, 1998) and contingent on Os absolute abundance. On the other hand, the radiogenic ^{187}Os are governed by the present concentration of the parent isotope ^{187}Re that has decayed over time (t). Both are normalized by the non-radiogenic ^{188}Os

[1/(Os*0.1329)= $1/^{188}Os$] in isochron dating, which can be in six or seven orders of magnitude difference in Os content. In this perspective, the time-integrated growth of ^{187}Os since sulfide-silicate equilibration is equivalent to the induced melt $^{187}Os/^{188}Os$ ratios at the moment of melting (time=0, Figure 3.7d), which is the time-dependent slope obtained by the law of radioactivity $t= 1/\lambda \ln(slope+1)$, where λ is the decay constant ($1.666*10^{11}$ yr^{-1}, Smoliar et al., 1996).

Consequently, the radiometrics of the pyroxenites Os phases defined in Figure 3.7d are measured in the postorogenic melt within their respective locations and presented in Figure 3.8. The results show that the postorogenic lavas retain ages corresponding to typical orogenies from their pertaining regions, as shown in Figure 3.1. The lavas mixing lines are consistent with the pyroxenite-Os hyperbola, where sulfide-Os' isotopic ratios anchor silicates-Os (Figure 3.7b). Besides, lavas' $^{178}Re/^{188}Os$ ratios that differed from the orogeny errorchrons are consistent with the excess Re phase in source lithology (Figure 3.6). Nevertheless, recording orogenic ages in lavas as young as Cenozoic in age is consistent with the pyroxenite isochronous relations measured in orogenic belts (*Sm-Nd system*: Medaris et al., 1995; Santos et al., 2002; Ackerman et al., 2009; Borghini et al., 2013; *Lu-Hf system*: Ackerman et al., 2016; *Re-Os system*: Meisel et al., 2001a; Ackerman et al., 2013). These findings indicate that the source lithology of postorogenic lavas is thermally equilibrated during continental collisions. For instance, the sulfide-silicate mixing line of the Canary Islands created an errorchron with the typical Hercynian and Appalachian age (Figure 3.8e). Although the Canary Islands are considered an oceanic hotspot, independent geophysical and geochemical studies revealed the existence of a cold and old SCLM beneath and as far as 250 km to the west

of the islands (Whitmarsh and Party, 1998; Widom et al., 1999; Miller et al., 2015). From a chronologic perspective, the modern oceans are younger than the Earth's major orogenies (< 200 Ma, Müller et al., 2008). Remnants and traces of the SCLM within the Earth's modern oceans are common (e.g., Kamenetsky et al., 2001; Bonadiman et al., 2005; Class and Roex, 2006). Thus, the Canary Islands are interpreted as plume-induced lavas with a SCLM mixture.

3.4.4 Os systematics in subduction-related lavas

Another example of a pyroxenite-Os hyperbola is applied to Re-Os data from NW Turkey, where postcollisional lavas transition into subduction settings. This transition is an arc activity in the Cenozoic time. The extension-related lavas at the edge of the Eurasian plate transition, with some spatial and temporal overlap, into subduction-related lavas toward the south (Figure 3.9). The latter is typical calc-alkaline lavas with a Nb-Ta subduction anomaly (Aldanmaz et al., 2000, 2015). However, Os sampled by extension-related lavas has a simple pyroxenite-Os hyperbola (Figure 3.7c). The lavas' radiometrics show slight or no excessive Re in the source lithology that could affect the $^{187}Re/^{188}Os$ ratio of the pyroxenites hyperbola. The sulfide-silicate mixing line yield an age of 254 Ma. The age agrees with the Late-Hercynian absolute ages measured further north in the Strandja Massif (290-220 Ma; Okay et al., 2001).

The extension-related volcanism is most likely enforced by the back-arc extension that happened to be on a continental margin. Rhenium and Os's contrast in the arcs is immensely high, possessing absolute concentrations in the ranges of 10^{0} and 10^{-3} ppb, respectively (Aldanmaz et al., 2015). This contrast shows no affiliation between Re and Os in the subduction setting, whereas the $^{187}Os/^{188}Os$ ratio is as low as 0.13. The

substantial involvement of Re phases in the subduction could be related to hydrous phases such as glaucophane from the slab (dehydration). The ^{187}Re–^{187}Os isotope evolution of the subduction-related lavas yields a period bounded by the oldest known K-Ar age for the arcs (37.3±0.6 Ma, Ercan et al., 1995). However, only the Eurasian plate-Os ($^{187}Os/^{188}Os = 0.1131$) could yield this exact age. The arcs $^{187}Os/^{188}Os$ ratios are corrected for the eruption time, causing a systematic age regression from 37 Ma to ~ 2 Ma. Allocating the radioactive decay of ^{187}Re to subducted slap Re and the non-radiogenic ^{188}Os to the continental margin creates the 37 Ma mixing line. As a result, the Eurasian plate appears to be extended beneath the accreted terrain (Sakarya, Figure 3.9), acting as a part of the mantle wedge for the north-dipping subduction. The systematic age regression in the subduction-related lavas shows that Re is increasingly added as time progresses. The buoyant hydrous flux continuously ascends, carrying the Os from the orogeny-modified lithosphere at the Eurasian plate.

3.5 Conclusion

The systematics of Os sampled by the postorogenic lavas shows concordance with the pyroxenites-Os hyperbola. The latter has the most radiogenic Os measured in mantle assemblages due to radioactive decay of Re and the inverse correlation of Re/Os ratio with Os. The high variability of the Re/Os ratio and obscurity of $^{187}Os/^{188}Os$ ratio measured in postorogenic lavas is due to Os siderophile nature and its partitioning in the mantle silicate and non-silicate systems. The Re anomalous concentrations and their disagreement with $^{187}Os/^{188}Os$ ratio are subject to an independent non-equilibrium phase (hydrous silicates). Similarly, Re and Os have no affiliation to volcanic arcs, thus they appear to have not relation to a subducted slab.

The petrogenesis of postorogenic lavas agrees with the mantle cumulate assemblages exhumed in the orogenic terrains as a source lithology, unraveling a chronologic link to mineralogic and isotopic changes associated with the continental collisions. The occurrences of cumulated assemblages as layers and veins in orogenic peridotites indicate secondary magmatic processes in the uppermost mantle. Separating a melt from a convective mantle with a lengthy history of melt removal (opening and closing oceans) and re-equilibration of the Re/Os ratio among the cumulate-forming minerals in the SCLM play a key role in understanding the elevated alumina/silica ratios $(Al_2O_3/SiO_2)_{PM}$ >0.1 and Os systematics of the postorogenic lavas. Created by Os sampled by young Cenozoic lavas, the errorchrons between two mixing end-members represented by pyroxenites sulfide- and silicate-Os reciprocals ($1/^{188}Os$) are consistent with absolute ages measured in crustal rocks. The time-integrated growth reveals synchronous modification and coupling between the continental crust and mantle lithosphere of particular importance to the SCLM rheological properties and continental amalgamations timeline.

References

van Acken, D., Becker, H., Walker, R.J., McDonough, W.F., Wombacher, F., Ash, R.D., and Piccoli, P.M., 2010, Formation of pyroxenite layers in the Totalp ultramafic massif (Swiss Alps) – Insights from highly siderophile elements and Os isotopes: Geochimica et Cosmochimica Acta, v. 74, p. 661–683, doi:10.1016/j.gca.2009.10.007.

Ackerman, L., Bizimis, M., Haluzová, E., Sláma, J., Svojtka, M., Hirajima, T., and Erban, V., 2016, Re-Os and Lu-Hf isotopic constraints on the formation and age of mantle pyroxenites from the Bohemian Massif: Lithos, v. 256–257, p. 197–210, doi:10.1016/j.lithos.2016.03.023.

Ackerman, L., Jelínek, E., Medaris, G., Ježek, J., Siebel, W., and Strnad, L., 2009, Geochemistry of Fe-rich peridotites and associated pyroxenites from Horní Bory, Bohemian Massif: Insights into subduction-related melt-rock reactions: Chemical Geology, v. 259, p. 152–167, doi:10.1016/j.chemgeo.2008.10.042.

Ackerman, L., Pitcher, L., Strnad, L., Puchtel, I.S., Jelínek, E., Walker, R.J., and Rohovec, J., 2013, Highly siderophile element geochemistry of peridotites and pyroxenites from Horní Bory, Bohemian Massif: Implications for HSE behaviour in subduction-related upper mantle: Geochimica et Cosmochimica Acta, doi:10.1016/j.gca.2012.09.050.

Alard, O., Lorand, J.P., Reisberg, L., Bodinier, J.L., Dautria, J.M., and O'reilly, S.Y., 2011, Volatile-rich metasomatism in montferrier xenoliths (Southern France): Implications for the abundances of chalcophile and highly siderophile elements in the subcontinental mantle: Journal of Petrology, doi:10.1093/petrology/egr038.

Aldanmaz, E., Pearce, J.A., Thirlwall, M.F., and Mitchell, J.G., 2000, Petrogenetic evolution of late Cenozoic, post-collision volcanism in western Anatolia, Turkey: Journal of Volcanology and Geothermal Research, v. 102, p. 67–95, doi:10.1016/S0377-0273(00)00182-7.

Aldanmaz, E., Pickard, M., Meisel, T., Altunkaynak, Ş., Sayıt, K., Şen, P., Hanan, B.B., and Furman, T., 2015, Source components and magmatic processes in the genesis of Miocene to Quaternary lavas in western Turkey: constraints from HSE distribution and Hf–Pb–Os isotopes: Contributions to Mineralogy and Petrology, v. 170, p. 23, doi:10.1007/s00410-015-1176-x.

Artemieva, I.M., Thybo, H., and Kaban, M.K., 2006, Deep Europe today: geophysical synthesis of the upper mantle structure and lithospheric processes over 3.5 Ga: Geological Society, London, Memoirs, v. 32, p. 11–41, doi:10.1144/GSL.MEM.2006.032.01.02.

Aulbach, S., Mungall, J.E., and Pearson, D.G.G., 2016, Distribution and Processing of Highly Siderophile Elements in Cratonic Mantle Lithosphere: Reviews in Mineralogy and Geochemistry, v. 81, p. 239–304, doi:10.2138/rmg.2016.81.5.

Azzouzi, M.E.L., Maury, R.C., Bellon, H., Youbi, N., Cotten, J., and Kharbouch, F., 2010, Petrology and K-Ar chronology of the Neogene-Quaternary Middle Atlas

basaltic province, Morocco: Bulletin de la Societe Geologique de France, v. 181, p. 243–257, doi:10.2113/gssgfbull.181.3.243.

Becker, H., 1996, Crustal trace element and isotopic signatures in garnet pyroxenites from garnet peridotite massifs from Lower Austria: J. Petrology, v. 37, p. 272–286, doi:10.1093/petrology/37.4.785.

Blusztajn, J., and Hegner, E., 2002, Osmium isotopic systematics of melilitites from the Tertiary Central European Volcanic Province in SW Germany: Chemical Geology, v. 189, p. 91–103, doi:10.1016/S0009-2541(02)00143-2.

Bodinier, J.L., Guiraud, M., Fabriés, J., Dostal, J., and Dupuy, C., 1987, Petrogenesis of layered pyroxenites from the Lherz, Freychinéde and Prades ultramafic bodies (Ariége, French Pyrénées): Geochimica et Cosmochimica Acta, v. 51, p. 279–290, doi:10.1016/0016-7037(87)90240-7.

Bodinier, J.L., Menzies, M.A., Shimizu, N., Frey, F.A., and McPherson, E., 2004, Silicate, Hydrous and Carbonate Metasomatism at Lherz, France: Contemporaneous Derivatives of Silicate Melt-Harzburgite Reaction: Journal of Petrology, v. 45, p. 299–320, doi:10.1093/petrology/egg107.

Bonadiman, C., Beccaluva, L., Coltorti, M., and Siena, F., 2005, Kimberlite-like metasomatism and “garnet signature” in spinel-peridotite xenoliths from Sal, Cape Verde Archipelago: Relics of a subcontinental mantle domain within the Atlantic oceanic lithosphere? Journal of Petrology, doi:10.1093/petrology/egi061.

Borghini, G., Rampone, E., Zanetti, A., Class, C., Cipriani, A., Hofmann, A.W., and Goldstein, S.L., 2013, Meter-scale Nd isotopic heterogeneity in pyroxenite-bearing ligurian peridotites encompasses global-scale upper mantle variability: Geology, v. 41, p. 1055–1058, doi:10.1130/G34438.1.

Bosch, D., Maury, R.C., El Azzouzi, M., Bollinger, C., Bellon, H., and Verdoux, P., 2014, Lithospheric origin for Neogene-Quaternary Middle Atlas lavas (Morocco): Clues from trace elements and Sr-Nd-Pb-Hf isotopes: Lithos, v. 205, p. 247–265, doi:10.1016/j.lithos.2014.07.009.

Burton, K.W., Schiano, P., Birck, J.L., Allègre, C.J., Rehkämper, M., Halliday, A.N., and Dawson, J.B., 2000, The distribution and behaviour of rhenium and osmium amongst mantle minerals and the age of the lithospheric mantle beneath Tanzania: Earth and Planetary Science Letters, v. 183, p. 93–106, doi:10.1016/S0012-821X(00)00259-4.

Carlson, R., and Nowell, G., 2001, Olivine-poor sources for mantle-derived magmas: Os and Hf isotopic evidence from potassic magmas of the Colorado Plateau: Geochemistry, Geophysics, Geosystems, v. 2, p. 2000gc000128, doi:10.1029/2000gc000128.

Carlson, R.W., Pearson, D.G., and James, D.E., 2005, Physical, chemical, and chronological characteristics of continental mantle: Reviews of Geophysics, v. 43, doi:https://doi.org/10.1029/2004RG000156.

Chen, Y., Su, B., and Chu, Z., 2017, Modification of an ancient subcontinental lithospheric mantle by continental subduction: Insight from the Maowu garnet

peridotites in the Dabie UHP belt, eastern China: Lithos, doi:10.1016/j.lithos.2017.01.025.

Class, C., and Roex, A.P. le, 2006, Continental material in the shallow oceanic mantle—How does it get there? Geology, v. 34, p. 129–132, doi:10.1130/G21943.1.

Dautria, J.M., Liotard, J.M., Bosch, D., and Alard, O., 2010, 160 Ma of sporadic basaltic activity on the Languedoc volcanic line (Southern France): A peculiar case of lithosphere-asthenosphere interplay: Lithos, v. 120, p. 202–222, doi:10.1016/j.lithos.2010.04.009.

Davies, D.R., and Rawlinson, N., 2014, On the origin of recent intraplate volcanism in Australia: Geology, v. 42, p. 1031–1034, doi:10.1130/G36093.1.

Day, J.M.D., Pearson, D.G., Macpherson, C.G., Lowry, D., and Carracedo, J.C., 2010, Evidence for distinct proportions of subducted oceanic crust and lithosphere in HIMU-type mantle beneath El Hierro and La Palma, Canary Islands: Geochimica et Cosmochimica Acta, v. 74, p. 6565–6589, doi:10.1016/j.gca.2010.08.021.

Downes, H., 2002, Formation and Modification of the Shallow Sub-continental Lithospheric Mantle: a Review of Geochemical Evidence from Ultramafic Xenolith Suites and Tectonically Emplaced Ultramafic Massifs of Western and Central Europe: Journal of Petrology, doi:10.1093/petrology/42.1.233.

Duggen, S., Hoernle, K.A., Hauff, F., Klugel, A., Bouabdellah, M., and Thirlwall, M.F., 2009, Flow of Canary mantle plume material through a subcontinental lithospheric corridor beneath Africa to the Mediterranean: Geology, v. 37, p. 283–286, doi:10.1130/G25426A.1.

Ercan, T., Satir, M., Steinitz, G., Dora, A., Sarifakioğlu, E., Adls, C., Walter, H.-J., and Yıldırım, T., 1995, Biga yarımadası ile Gökçeada , Bozcaada ve Tavşan adalarındaki (KB Anadolu) Tersiyer Volkanizmasının Özellikleri: Mta, v. 117, p. 55–86.

Fabriès, J., Lorand, J.P., and Guiraund, M., 2001, Petrogenesis of the amphibole-rich veins from the Lherz orogenic Iherzolite Massif (Eastern Pyrenees, France): A case study for the origin of orthopyroxene-bearing amphibole pyroxenites in the lithospheric mantle: Contributions to Mineralogy and Petrology, v. 140, p. 383–403, doi:10.1007/s004100000132.

Fezaa, N., Liégeois, J.P., Abdallah, N., Cherfouh, E.H., De Waele, B., Bruguier, O., and Ouabadi, A., 2010, Late Ediacaran geological evolution (575-555 Ma) of the Djanet Terrane, Eastern Hoggar, Algeria, evidence for a Murzukian intracontinental episode: Precambrian Research, v. 180, p. 299–327, doi:10.1016/j.precamres.2010.05.011.

Fitton, J.G., James, D., and Leeman, W.P., 1991, Basic magmatism associated with Late Cenozoic extension in the western United States: Compositional variations in space and time: Journal of Geophysical Research: Solid Earth, v. 96, p. 13693–13711, doi:10.1029/91JB00372.

France, L., Chazot, G., Kornprobst, J., Dallai, L., Vannucci, R., Grégoire, M., Bertrand, H., and Boivin, P., 2015, Mantle refertilization and magmatism in old orogenic

regions: The role of late-orogenic pyroxenites: Lithos, v. 232, p. 49–75, doi:10.1016/j.lithos.2015.05.017.

Frost, D.J., 2006, The Stability of Hydrous Mantle Phases: Reviews in Mineralogy and Geochemistry, v. 62, p. 243–271, doi:10.2138/rmg.2006.62.11.

Garrido, C.J., and Bodinier, J.-L., 1999, Diversity of Mafic Rocks in the Ronda Peridotite: Evidence for Pervasive Melt-Rock Reaction during Heating of Subcontinental Lithosphere by Upwelling Asthenosphere: Journal of Petrology, v. 40, p. 729–754, doi:10.1093/petroj/40.5.729.

Gibson, S.A., Malarkey, J., and Day, J.A., 2008, Melt Depletion and Enrichment beneath the Western Kaapvaal Craton: Evidence from Finsch Peridotite Xenoliths: Journal of Petrology, v. 49, p. 1817–1852, doi:10.1093/petrology/egn048.

Globig, J., Fernàndez, M., Torne, M., Vergés, J., Robert, A., and Faccenna, C., 2016, New insights into the crust and lithospheric mantle structure of Africa from elevation, geoid, and thermal analysis: Journal of Geophysical Research: Solid Earth, v. 121, p. 5389–5424, doi:10.1002/2016JB012972.

Griffin, W.L., Graham, S., O'Reilly, S.Y., and Pearson, N.J., 2004, Lithosphere evolution beneath the Kaapvaal Craton: Re-Os systematics of sulfides in mantle-derived peridotites, *in* Chemical Geology, doi:10.1016/j.chemgeo.2004.04.007.

Gysi, A.P., Jagoutz, O., Schmidt, M.W., and Targuisti, K., 2011, Petrogenesis of pyroxenites and melt infiltrations in the ultramafic complex of Beni Bousera, Northern Morocco: Journal of Petrology, v. 52, p. 1679–1735.

Haase, K.M., and Renno, A.D., 2008, Variation of magma generation and mantle sources during continental rifting observed in Cenozoic lavas from the Eger Rift, Central Europe: Chemical Geology, v. 257, p. 195–205, doi:10.1016/j.chemgeo.2008.09.003.

Harris, G.A., Pearson, D.G., Liu, J., Hardman, M.F., Snyder, D.B., and Kelsch, D., 2018, Mantle composition, age and geotherm beneath the Darby kimberlite field, west central Rae Craton: Mineralogy and Petrology, v. 112, p. 57–70.

Harvey, J., Dale, C.W., Gannoun, A., and Burton, K.W., 2011, Osmium mass balance in peridotite and the effects of mantle-derived sulphides on basalt petrogenesis: Geochimica et Cosmochimica Acta, doi:10.1016/j.gca.2011.07.001.

Harvey, J., Gannoun, A., Burton, K.W., Schiano, P., Rogers, N.W., and Alard, O., 2010, Unravelling the effects of melt depletion and secondary infiltration on mantle Re-Os isotopes beneath the French Massif Central: Geochimica et Cosmochimica Acta, v. 74, p. 293–320, doi:10.1016/j.gca.2009.09.031.

Harvey, J., Warren, J.M., and Shirey, S.B., 2016, Mantle Sulfides and their Role in Re–Os and Pb Isotope Geochronology: Reviews in Mineralogy and Geochemistry, v. 81, p. 579–649, doi:10.2138/rmg.2016.81.10.

Hofmann, A.W., 1988, Chemical differentiation of the Earth: the relationship between mantle, continental crust, and oceanic crust: Earth and Planetary Science Letters, doi:10.1016/0012-821X(88)90132-X.

Ireland, T.R., 1998, Development of the early Paleozoic Pacific margin of Gondwana from detrital-zircon ages across the Delamerian orogen Ireland T.R., Flottmann T., Fanning C.M., Gibson G.M. & Preiss W.V., Geology, 1988, 26/3 (243–246): Journal of African Earth Sciences, v. 27, p. XII–XII, doi:10.1016/S0899-5362(98)90636-4.

Jiang, L., and Zhi, X., 2010, Re-Os isotope geochemistry of basalts from Hannuoba, North China: Evidence for Re volatile loss and crust-mantle interaction: Acta Petrologica Sinica, v. 26, p. 1265–1276.

Jung, S., Pfänder, J.A., Brauns, M., and Maas, R., 2011, Crustal contamination and mantle source characteristics in continental intra-plate volcanic rocks: Pb, Hf and Os isotopes from central European volcanic province basalts: Geochimica et Cosmochimica Acta, v. 75, p. 2664–2683, doi:10.1016/j.gca.2011.02.017.

Jung, S., Pfänder, J.A., Brügmann, G., and Stracke, A., 2005, Sources of primitive alkaline volcanic rocks from the Central European Volcanic Province (Rhön, Germany) inferred from Hf, Os and Pb isotopes: Contributions to Mineralogy and Petrology, v. 150, p. 546–559, doi:10.1007/s00410-005-0029-4.

Kamenetsky, V.S., Maas, R., Sushchevskaya, N.M., Norman, M.D., Cartwright, I., and Peyve, A.A., 2001, Remnants of Gondwanan continental lithosphere in oceanic upper mantle: Evidence from the South Atlantic Ridge: Geology, doi:10.1130/0091-7613(2001)029<0243:ROGCLI>2.0.CO;2.

Karlstrom, K.E., and Daniel, C.G., 1993, Restoration of Laramide right-lateral strike slip in northern New Mexico by using Proterozoic piercing points: tectonic implications from the Proterozoic to the Cenozoic: Geology, v. 21, p. 1139–1142, doi:10.1130/0091-7613(1993)021<1139:ROLRLS>2.3.CO;2.

Kumar, N., Reisberg, L., and Zindler, A., 1996, A major and trace element and strontium, neodymium, and osmium isotopic study of a thick pyroxenite layer from the Beni Bousera Ultramafic Complex of northern Morocco: Geochimica et Cosmochimica Acta, v. 60, p. 1429–1444, doi:10.1016/0016-7037(95)00443-2.

Levander, A., Schmandt, B., Miller, M.S., Liu, K., Karlstrom, K.E., Crow, R.S., Lee, C.T.A., and Humphreys, E.D., 2011, Continuing Colorado plateau uplift by delamination-style convective lithospheric downwelling: Nature, v. 472, p. 461–465, doi:10.1038/nature10001.

Liégeois, J.P., Abdelsalam, M.G., Ennih, N., and Ouabadi, A., 2013, Metacraton: Nature, genesis and behavior: Gondwana Research, v. 23, p. 220–237, doi:10.1016/j.gr.2012.02.016.

Liew, T.C., and Hofmann, A.W., 1988, of the Hercynian Fold Belt of central Europe : Indications from a Nd and Sr isotopic study: Contributions to Mineralogy and Petrology, v. 98, p. 129–138.

Liu, R.X., Chen, W.J., Sun, J.Z., and Li, D.M., 1992, The K–Ar age and tectonic environment of Cenozoic volcanic rocks in China: The Age and Geochemistry of Cenozoic Volcanic Rock in China, p. 1–43.

Liu, C.-Z., Snow, J.E., Hellebrand, E., Brügmann, G., von der Handt, A., Büchl, A., and Hofmann, A.W., 2008, Ancient, highly heterogeneous mantle beneath Gakkel ridge, Arctic Ocean: Nature, v. 452, p. 311–316, doi:10.1038/nature06688.

Lorand, J., 1989, The Cu□ Fe□ Ni sulfide component of the amphibole-rich veins from the Lherz and Freychinède spinel peridotite massifs (Northeastern Pyrenees, France): A comparison with mantle-derived megacrysts from alkali basalts: Lithos, v. 23, p. 281–298.

Luguet, A., Pearson, D.G., Nowell, G.M., Dreher, S.T., Coggon, J.A., Spetsius, Z.V., and Parman, S.W., 2008, Enriched Pt-Re-Os isotope systematics in plume lavas explained by metasomatic sulfides: Science, doi:10.1126/science.1149868.

Lustrino, M., and Wilson, M., 2007, The circum-Mediterranean anorogenic Cenozoic igneous province: Earth-Science Reviews, v. 81, p. 1–65, doi:10.1016/j.earscirev.2006.09.002.

Marcantonio, F., Zindler, A., Elliott, T., and Staudigel, H., 1995, Os isotope systematics of La Palma, Canary Islands: Evidence for recycled crust in the mantle source of HIMU ocean islands: Earth and Planetary Science Letters, v. 133, p. 397–410, doi:10.1016/0012-821X(95)00092-Q.

Mayer, B., Jung, S., Romer, R.L., Pfänder, J.A., Klügel, A., Pack, A., and Gröner, E., 2014, Amphibole in alkaline basalts from intraplate settings: Implications for the petrogenesis of alkaline lavas from the metasomatised lithospheric mantle: Contributions to Mineralogy and Petrology, v. 167, p. 1–22, doi:10.1007/s00410-014-0989-3.

McBride, J.S., D., LambertD., Nicholls, I. a., and Price, R.C., 2001, Osmium Isotopic Evidence for Crust – Mantle Interaction in the Genesis of Continental Intraplate Basalts from the Newer Volcanics Province , Southeastern Australia: Journal of Petrology, v. 42, p. 1197–1218, doi:10.1093/petrology/42.6.1197.

McDonough, W.F., McCulloch, M.T., and Sun, S.S., 1985, Isotopic and geochemical systematics in Tertiary-Recent basalts from southeastern Australia and implications for the evolution of the sub-continental lithosphere: Geochimica et Cosmochimica Acta, v. 49, p. 2051–2067, doi:10.1016/0016-7037(85)90063-8.

McDonough, W.F., and Sun, S.-S., 1995, The composition of the Earth: Chemical geology, v. 120, p. 223–253.

McPherson, E., Thirlwall, M.F., Parkinson, I.J., Menzies, M. a., Bodinier, J.L., Woodland, A., and Bussod, G., 1996, Geochemistry of metasomatism adjacent to amphibole-bearing veins in the Lherz peridotite massif.: Chemical Geology, v. 134, p. 135–157, doi:10.1016/S0009-2541(96)00084-8.

Medaris, L.G., Beard, B.L., Johnson, C.M., Valley, J.W., Spicuzza, M.J., Jelínek, E., and Mísâr, Z., 1995, Garnet pyroxenite and eclogite in the Bohemian Massif: geochemical evidence for Variscan recycling of subducted lithosphere: Geologische Rundschau, doi:10.1007/BF00284516.

Meisel, T., Moser, J., and Wegscheider, W., 2001a, Recognizing heterogeneous distribution of platinum group elements (PGE) in geological materials by means

of the Re-Os isotope system: Fresenius' Journal of Analytical Chemistry, v. 370, p. 566–572, doi:10.1007/s002160100791.

Meisel, T., Walker, R.J., Irving, A.J., and Lorand, J.P., 2001b, Osmium isotopic compositions of mantle xenoliths: A global perspective: Geochimica et Cosmochimica Acta, doi:10.1016/S0016-7037(00)00566-4.

Miller, M.S., O'Driscoll, L.J., Butcher, A.J., and Thomas, C., 2015, Imaging Canary Island hotspot material beneath the lithosphere of Morocco and southern Spain: Earth and Planetary Science Letters, v. 431, p. 186–194, doi:10.1016/j.epsl.2015.09.026.

Montero, P., Haissen, F., Mouttaqi, A., Molina, J.F., Errami, A., Sadki, O., Cambeses, A., and Bea, F., 2016, Contrasting SHRIMP U–Pb zircon ages of two carbonatite complexes from the peri-cratonic terranes of the Reguibat Shield: Implications for the lateral extension of the West African Craton: Gondwana Research, v. 38, p. 238–250, doi:10.1016/j.gr.2015.12.005.

Mukasa, S.B., Shervais, J.W., Wilshire, H.G., and Nielson, J.E., 1991, Intrinsic Nd, Pb, and Sr Isotopic Heterogeneities Exhibited by the Lherz Alpine Peridotite Massif, French Pyrenees: Journal of Petrology, v. Special_Vo, p. 117–134, doi:10.1093/petrology/Special_Volume.2.117.

Müller, R.D., Sdrolias, M., Gaina, C., and Roest, W.R., 2008, Age, spreading rates, and spreading asymmetry of the world's ocean crust: Geochemistry, Geophysics, Geosystems, doi:10.1029/2007GC001743.

Nasir, S.J., Everard, J.L., McClenaghan, M.P., Bombardieri, D., and Worthing, M.A., 2010, The petrology of high pressure xenoliths and associated Cenozoic basalts from Northeastern Tasmania: Lithos, v. 118, p. 35–49, doi:10.1016/j.lithos.2010.03.012.

Okay, A.L., Satır, M., Tüysüz, O., Akyüz, S., and Chen, F., 2001, The tectonics of the Strandja Massif: late-Variscan and mid-Mesozoic deformation and metamorphism in the northern Aegean: International Journal of Earth Sciences, v. 90, p. 217–233.

Oostingh, K.F., Jourdan, F., Merle, R., and Chiaradia, M., 2016, Spatio-temporal geochemical evolution of the SE Australian upper mantle deciphered from the Sr, Nd and Pb isotope compositions of Cenozoic intraplate volcanic rocks: Journal of Petrology, v. 57, p. 1509–1530, doi:10.1093/petrology/egw048.

Pearson, D.G., Davies, G.R., and Nixon, P.H., 1993, Geochemical constraints on the petrogenesis of diamond facies pyroxenites from the Beni Bousera Peridotite Massif, North Morocco: Journal of Petrology, v. 34, p. 125–172, doi:10.1093/petrology/34.1.125.

Pearson, D.G., and Nowell, G.M., 2004, Re-Os and Lu-Hf Isotope Constraints on the Origin and Age of Pyroxenites from the Beni Bousera Peridotite Massif: Implications for Mixed Peridotite-Pyroxenite Mantle Sources: Journal of Petrology, v. 45, p. 439–455, doi:10.1093/petrology/egg102.

Pfänder, J.A., Jung, S., Klügel, A., Münker, C., Romer, R.L., Sperner, B., and Rohrmüller, J., 2018, Recurrent local melting of metasomatised lithospheric mantle in response to continental rifting: Constraints from basanites and nephelinites/melilitites from SE Germany: Journal of Petrology, doi:10.1093/petrology/egy041.

Pilet, S., Baker, M.B., and Stolper, E.M., 2008, Metasomatized lithosphere and the origin of alkaline lavas.: Science (New York, N.Y.), v. 320, p. 916–919, doi:10.1126/science.1156563.

Radivojević, M., Toljić, M., Turki, S.M., Bojić, Z., Šarić, K., and Cvetković, V., 2015, Neogene to Quaternary basalts of the Jabal Eghei (Nuqay) area (south Libya): Two distinct volcanic events or continuous volcanism with gradual shift in magma composition? Journal of Volcanology and Geothermal Research, v. 293, p. 57–74, doi:10.1016/j.jvolgeores.2015.02.003.

Reisberg, L.C., Allègre, C.J., and Luck, J.-M., 1991, The Re-Os systematics of the Ronda Ultramafic Complex of southern Spain: Earth and Planetary Science Letters, v. 105, p. 196–213, doi:10.1016/0012-821X(91)90131-Z.

Rollinson, H., 2010, Coupled evolution of Archean continental crust and subcontinental lithospheric mantle: Geology, v. 38, p. 1083–1086, doi:10.1130/G31159.1.

Romer, R.L., and Kroner, U., 2016, Phanerozoic tin and tungsten mineralization—Tectonic controls on the distribution of enriched protoliths and heat sources for crustal melting: Gondwana Research, v. 31, p. 60–95, doi:10.1016/j.gr.2015.11.002.

Roy-Barman, M., Luck, J.-M., Allègre, C.J., and Allbgre, C.J., 1996, Os isotopes in orogenic lherzolite massifs and mantle heterogeneities: Chemical Geology, v. 130, p. 55–64, doi:10.1016/0009-2541(96)00002-2.

Santos, J.F., Schärer, U., Ibarguchi, J.I.G., and Girardeau, J., 2002, Genesis of pyroxenite-rich peridotite at Cabo Ortegal (NW Spain): Geochemical and Pb-Sr-Nd isotope data: Journal of Petrology, v. 43, p. 17–43, doi:10.1093/petrology/43.1.17.

Servali, A., and Korenaga, J., 2018, Oceanic origin of continental mantle lithosphere: Geology, v. 46, p. 1047–1050, doi:10.1130/G45180.1.

Shirey, S.B., and Walker, R.J., 1998, The Re-Os isotope system in cosmochemistry and high-temperature geochemistry: Annual Review of Earth and Planetary Sciences, v. 26, p. 423–500, doi:10.1146/annurev.earth.26.1.423.

Smoliar, M.I., Walker, R.J., Morgan, J.W., 1996. Re-Os ages of group IIA, IIIA, IVA, and IVB iron meteorites. Science (80-.). 271, 1099–1102. https://doi.org/10.1126/science.271.5252.1099

Svojtka, M., Ackerman, L., Medaris Jr, L.G., Hegner, E., Valley, J.W., Hirajima, T., Jelínek, E., and Hrstka, T., 2016, Petrological, geochemical and Sr–Nd–O isotopic constraints on the origin of garnet and spinel pyroxenites from the Moldanubian Zone of the Bohemian Massif: Journal of Petrology, v. 57, p. 897–920.

Takahashi, N., 1992, Evidence for melt segregation towards fractures in the Horoman mantle peridotite complex: Nature, v. 359, p. 52–55, doi:10.1038/359052a0.

Tilhac, R., Oliveira, B., Griffin, W.L., O'Reilly, S.Y., Schaefer, B.F., Alard, O., Ceuleneer, G., Afonso, J.C., and Grégoire, M., 2020, Reworking of old continental lithosphere: Unradiogenic Os and decoupled HfNd isotopes in sub-arc mantle pyroxenites: Lithos, v. 354, p. 105346.

Ulrych, J., Krmíček, L., Tomek, Č., Lloyd, F.E., Ladenberger, A., Ackerman, L., and Balogh, K., 2016, Petrogenesis of Miocene alkaline volcanic suites from western Bohemia: whole rock geochemistry and Sr–Nd–Pb isotopic signatures: Chemie der Erde - Geochemistry, v. 76, p. 77–93, doi:10.1016/j.chemer.2015.11.003.

Ulrych, J., Lloyd, F.E., Balogh, K., and Hegner, E., 2010, Jelínek, E., Řanda, Z., & Novák, J. K. . Geochemical characteristics of the high-and low-Ti basaltic rocks from the uplifted shoulder of the Ohře (Eger) Chemie der Erde-Geochemistry, .: v. 70 SRC-, p. 319–333.

Wang, K.L., O'Reilly, S.Y., Griffin, W.L., Pearson, N.J., and Zhang, M., 2009, Sulfides in mantle peridotites from Penghu Islands, Taiwan: Melt percolation, PGE fractionation, and the lithospheric evolution of the South China block: Geochimica et Cosmochimica Acta, doi:10.1016/j.gca.2009.04.030.

Whitmarsh, R.B., and Party, L.S., 1998, Drilling reveals transition from continental breakup to early magmatic crust.: American Geophysical Union, v. 79 SRC-, p. 173–181.

Widom, E., Hoernle, K. a, Shirey, S.B., and Schmincke, H.-U., 1999, Os Isotope Systematics in the Canary Islands and Madeira: Lithospheric Contamination and Mantle Plume Signatures: Journal of Petrology, v. 40, p. 279–296, doi:10.1093/petroj/40.2.279.

Windley, B.F., Maruyama, S., and Xiao, W.J., 2010, Delamination/thinning of sub-continental lithospheric mantle under Eastern China: The role of water and multiple subduction.: American Journal of Science, v. 310 SRC-, p. 1250–1293.

Xu, Y.G., Chung, S.L., Ma, J., and Shi, L., 2004, Contrasting Cenozoic lithospheric evolution and architecture in the western and eastern Sino-Korean Craton: Constraints from geochemistry of basalts and mantle xenoliths.: The Journal of Geology, v. 112 SRC-, p. 593–605.

Xu, Y.-G., Ma, J.-L., Frey, F.A., Feigenson, M.D., and Liu, J.-F., 2005, Role of lithosphere–asthenosphere interaction in the genesis of Quaternary alkali and tholeiitic basalts from Datong, western North China Craton: Chemical Geology, v. 224, p. 247–271, doi:10.1016/j.chemgeo.2005.08.004.

Yang, J.H., Zhang, M., and Wu, F.Y., 2018, Mesozoic decratonization of the North China Craton by lithospheric delamination: Evidence from Sr-Nd-Hf-Os isotopes of mantle xenoliths of Cenozoic alkaline basalts in Yangyuan, Hebei Province, China: Journal of Asian Earth Sciences, doi:10.1016/j.jseaes.2017.09.002.

Zhao, G., 2001, Palaeoproterozoic assembly of the North China craton: Geological Magazine, v. 138, p. 87–91.

Zhao, G., Cawood, P.A., Wilde, S.A., Sun, M., and Lu, L., 2000, Metamorphism of basement rocks in the Central Zone of the North China Craton: implications for Paleoproterozoic tectonic evolution.: Precambrian Research, v. 103 SRC-, p. 55–88.

Zhao, G., Wilde, S.A., Cawood, P.A., and Sun, M., 2001, Archean blocks and their boundaries in the North China Craton: lithological, geochemical, structural and P-T path constraints and tectonic evolution.: Precambrian Research, v. 107 SRC-, p. 45–73.

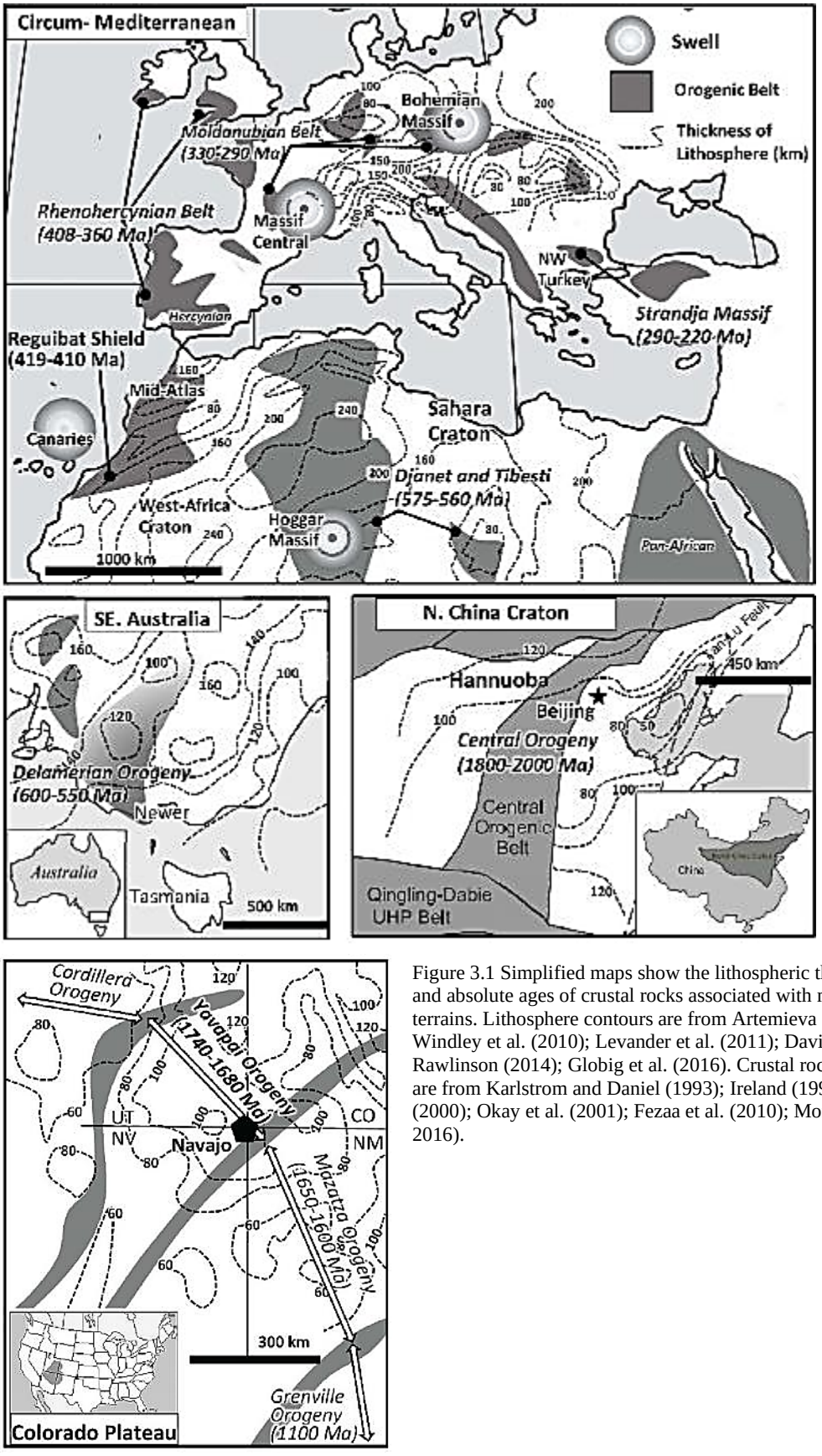

Figure 3.1 Simplified maps show the lithospheric thickness (km) and absolute ages of crustal rocks associated with major orogenic terrains. Lithosphere contours are from Artemieva et al. (2006); Windley et al. (2010); Levander et al. (2011); Davies and Rawlinson (2014); Globig et al. (2016). Crustal rocks' absolute ages are from Karlstrom and Daniel (1993); Ireland (1998); Zhao et al. (2000); Okay et al. (2001); Fezaa et al. (2010); Montero et al. 2016).

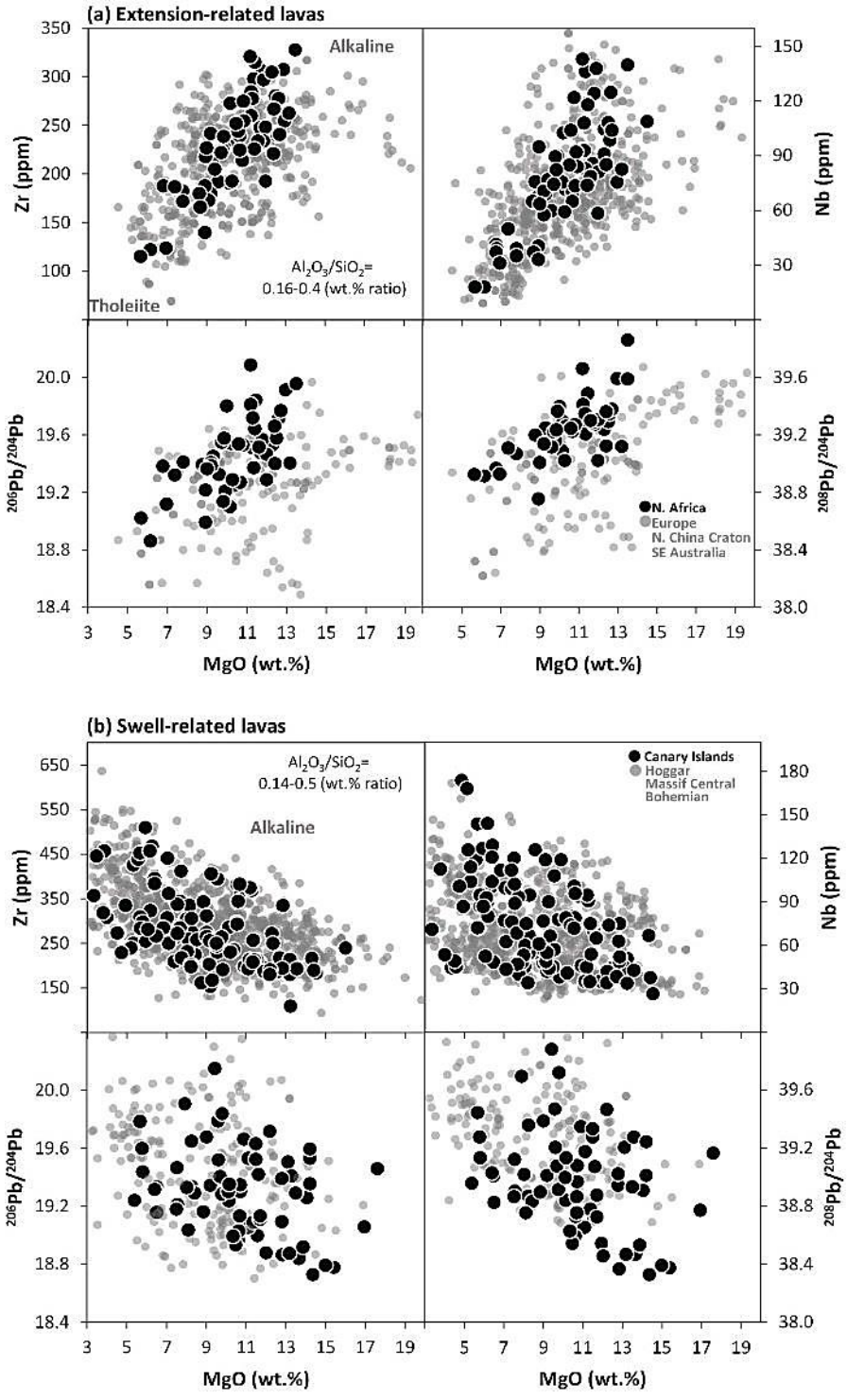

Figure 3.2 Global compilation of Cenozoic basaltic lavas grouped into **a)** Extension-related lavas [*N Africa*: Mid Atlas, Sahara Craton; *Europe*: Germany, Pannonian Basin, Calatrava-central Iberia, N. Italy-Veneto Province, NW Turkey-Çanakkale and Thrace Provinces; *SE. Australia*: Newer and Tasmania; *N China Craton*: Hannuoba, Datong, Yangyuan, Yinxian, Fanshi, and Fangzhen]. **b)** Swell-related lavas [*Canary Islands-Hoggar*, *Massif Central*, *Bohemian*]. Data sources of the circum-Mediterranean are from Lustrino and Wilson, (2007) and additional data from Azzouzi et al. (2010); Bosch et al. (2014); Duggen et al. (2009); Haase and Renno (2008); Radivojević et al. (2015); Pfänder et al. (2018); and Ulrych et al. (2016, 2010). SE Australia data are from McDonough et al. (1985) and Nasir et al. (2010). N China Craton dada are from Xu et al. (2005, 2004) and references therein.

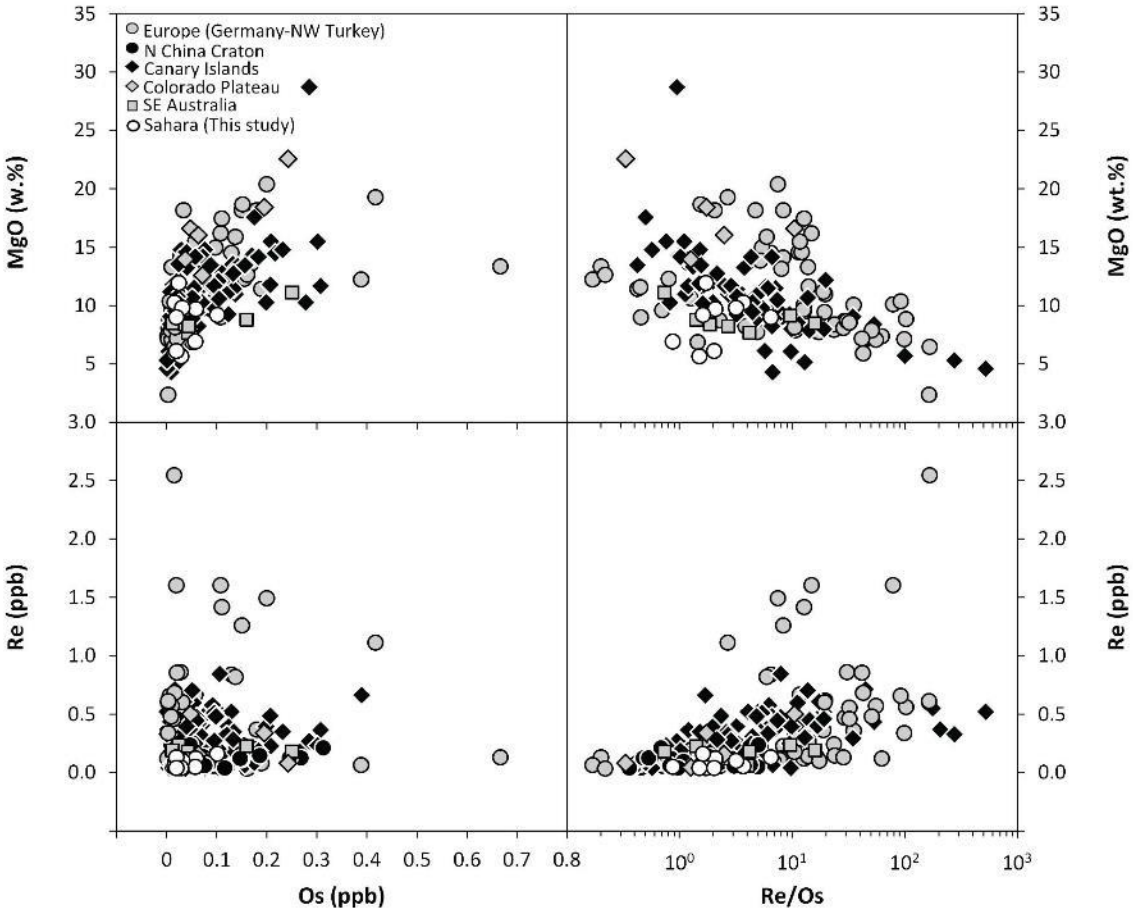

Figure 3.3 Re and Os sampled by Cenozoic basaltic lavas. Data localities are *Germany* (Blusztajn and Hegner, 2002; Jung et al., 2005, 2011), *N China Craton* (Liu et al., 1992; Jiang and Zhi, 2010), *SE Australia* (McBride et al., 2001), *NW Turkey* (Aldanmaz et al., 2015), *Colorado Plateau* (Carlson and Nowell, 2001), and *Canary Islands* (Marcantonio et al., 1995; Widom et al., 1999; Day et al., 2010), and Sahara (This study).

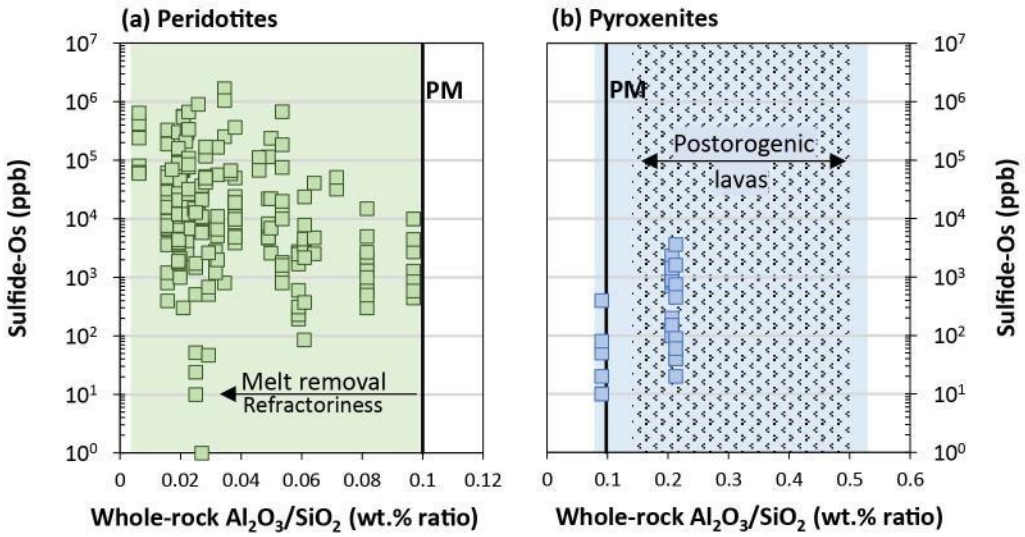

Figure 3.4 Whole-rock Al_2O_3/SiO_2 (wt.% ratio) of mantle assemblages and *in-situ* Os content of sulfides. As a reference, the compositional ratio Al_2O_3/SiO_2= 0.1 of the Primitive Mantle from McDonough and Sun (1995) is denoted in the plots. **a)** Peridotites [whole-rock and Os data are from chapter 2 and references therein]. **b)** Pyroxenites [whole-rock and Os data are from Reisberg et al. (1991); Roy-Barman et al. (1996); Kumar et al. (1996); Meisel et al. (2001a); Pearson and Nowell (2004); van Acken et al. (2010); Gysi et al. (2011); Ackerman et al. (2013, 2016); France et al. (2015); Svojtka et al. (2016); Chen et al. (2017); Yang et al. (2018); Tilhac et al. (2020)].

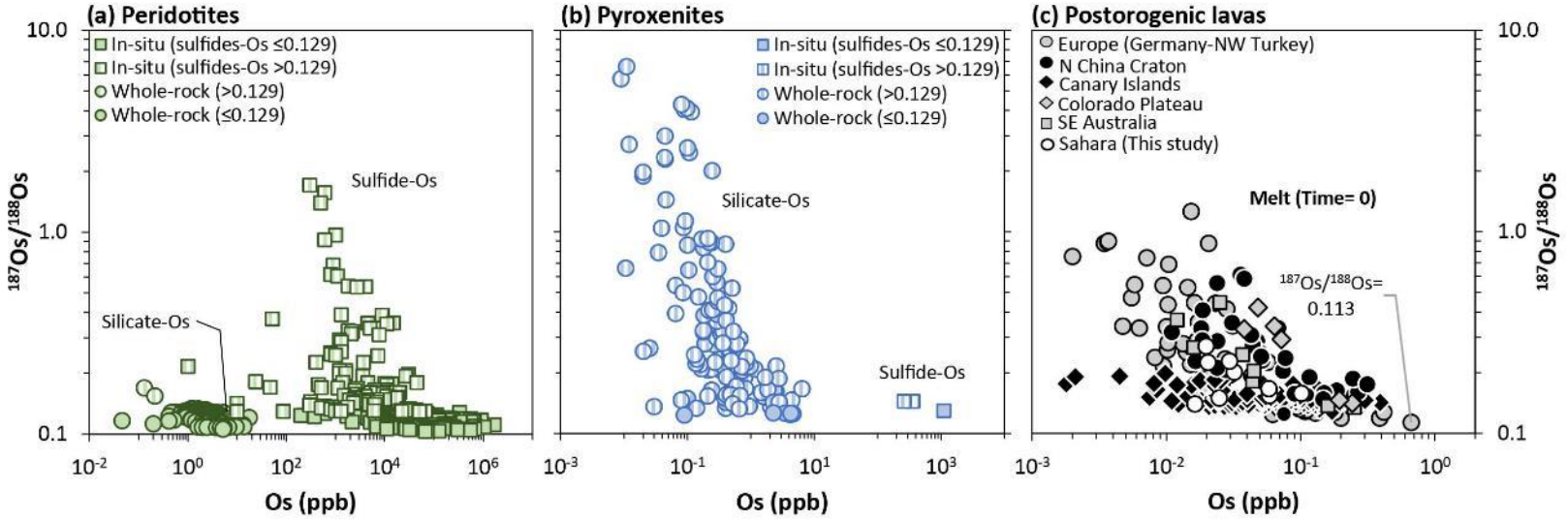

Figure 3.5 The isotopic ratios of Os measured in **a)** Peridotites, **b)** Pyroxenite, and **c)** Postorogenic lavas**.**

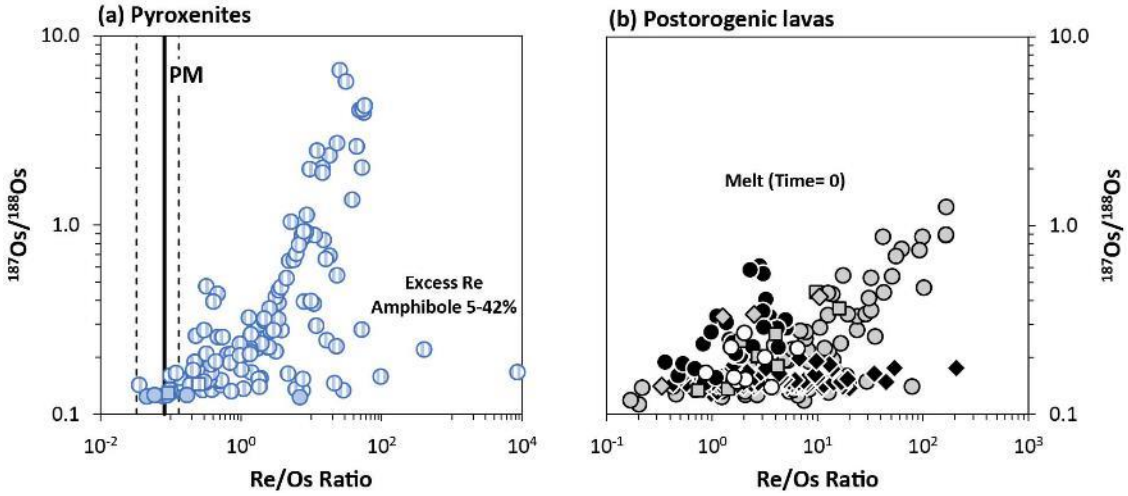

Figure 3.6 Coupling the Re/Os ratio with $^{187}Os/^{188}Os$ ratio in **a)** Pyroxenites [solid and dashed lines are the Primitive Mantle Re/Os ratio and associated uncertainties from McDonough and Sun (1995)] and **b)** Postorogenic lavas. (symbols as in Figure 3.5).

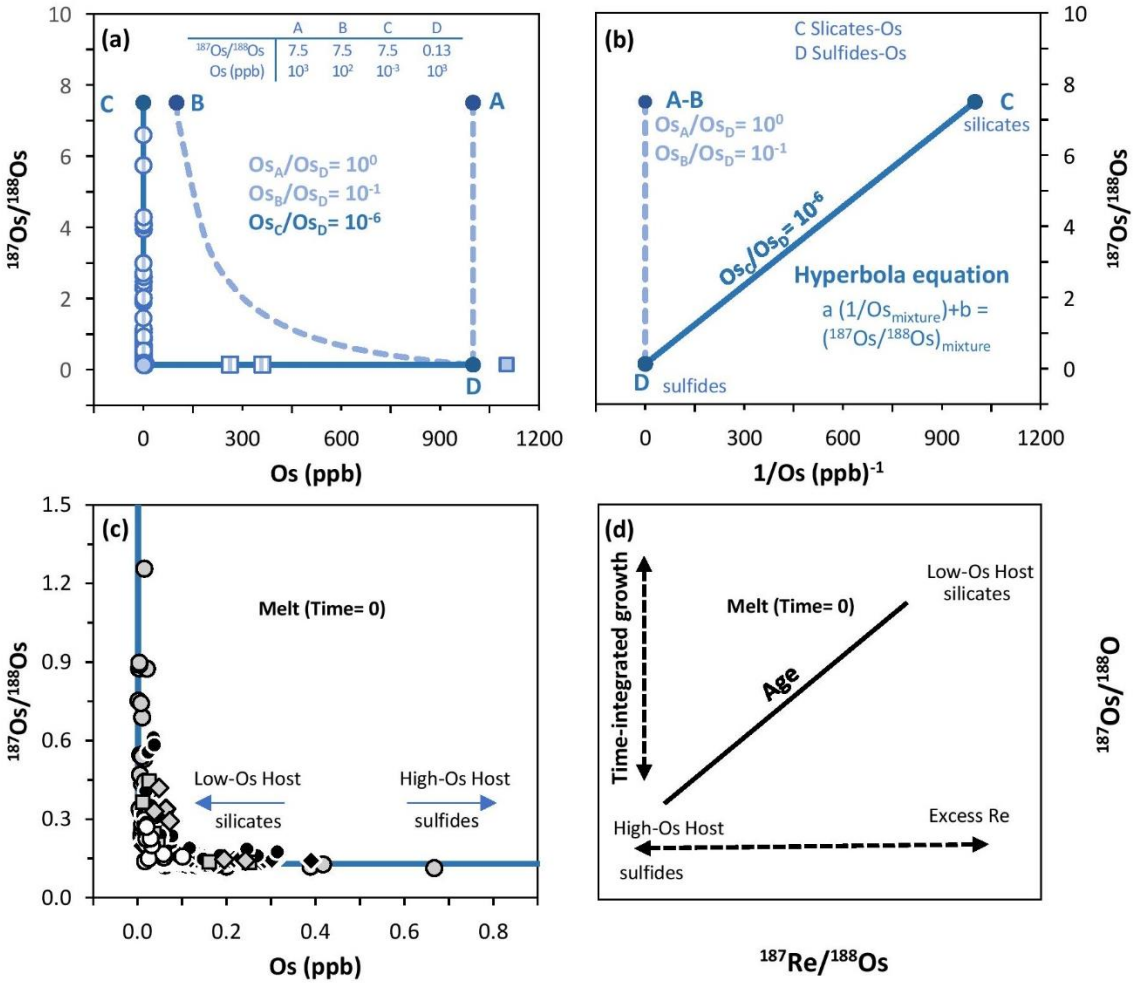

Figure 3.7 Pyroxenite-Os hyperbola and Os systematics of postorogenic lavas. **a)** Effects of $Os_{silicate}/Os_{sulfide}$ ratio on the shape of pyroxenite hyperbola. **b)** Transforming the hyperbola equation into a straight light using Os reciprocals as an x-coordinate variable. The slope is equivalent to the parameter (a) of the equation (details of the hyperbola parameters are in APPENDIX-B). **c)** The integration of the pyroxenite-Os hyperbola with Os sampled by postorogenic lavas. **d)** Coupling ^{187}Re with non-radiogenic ^{188}Os reciprocals in sulfides and silicates and the excess Re end-members observed in Figure 3.6.

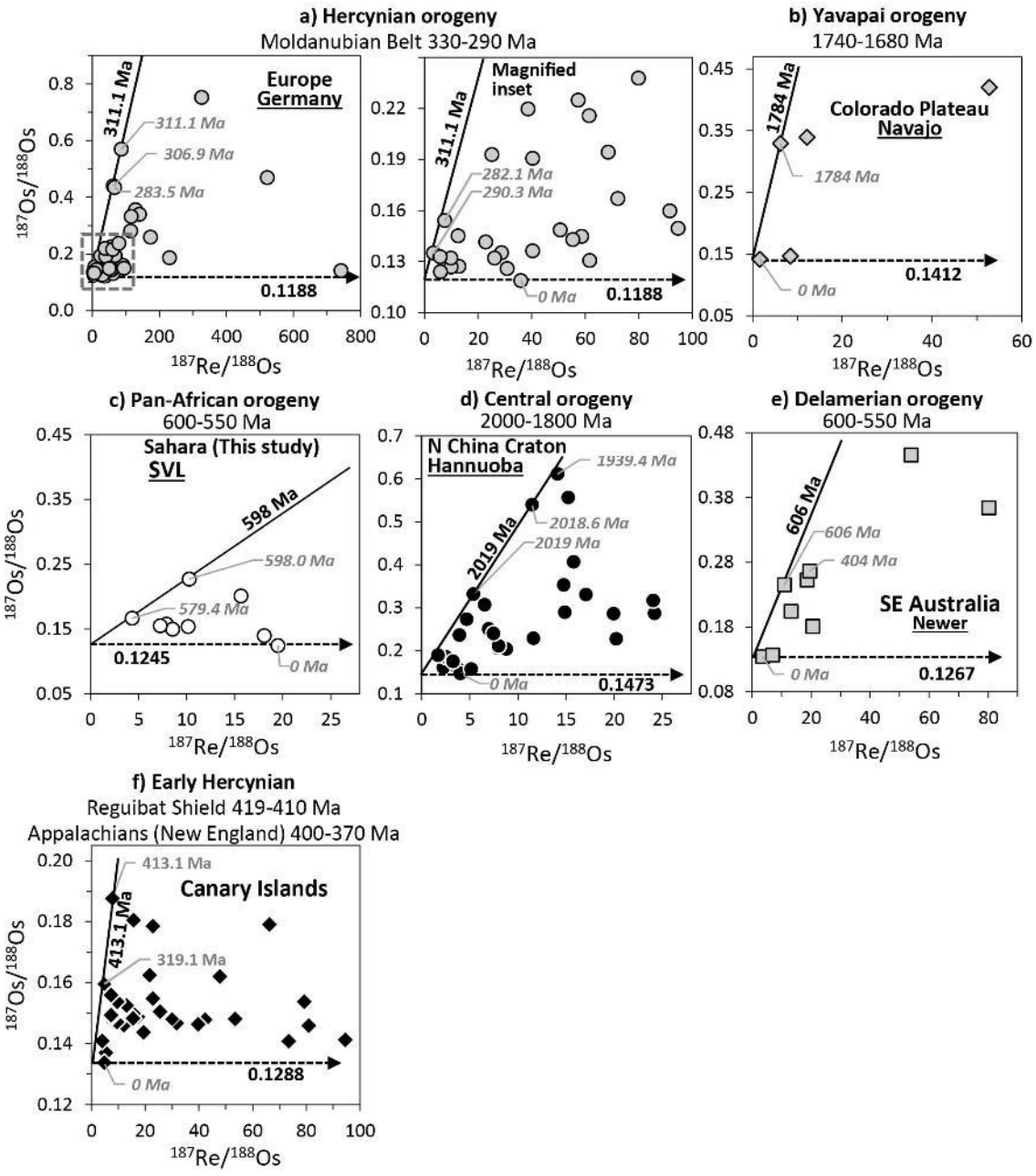

Figure 3.8 The $^{187}Os/^{188}Os$ and $^{187}Re/^{188}Os$ ratios of the postorogenic lavas. **a)** Germany (Moldanubian orogeny, Liew and Hofmann, 1988). **b)** Colorado Plateau (Yavapai orogeny, Karlstrom and Daniel, 1993). **c)** Sahara (Pan-African orogeny**,** Fezaa et al., 2010). **d)** N China Craton (Central orogeny, Zhao et al., 2000, 2001). **e)** SE Australia (Delamerian orogeny, Ireland, 1998). **f)** Canary Islands (Hercynian/Appalachian orogeny, Montero et al., 2016; Romer and Kroner, 2016).

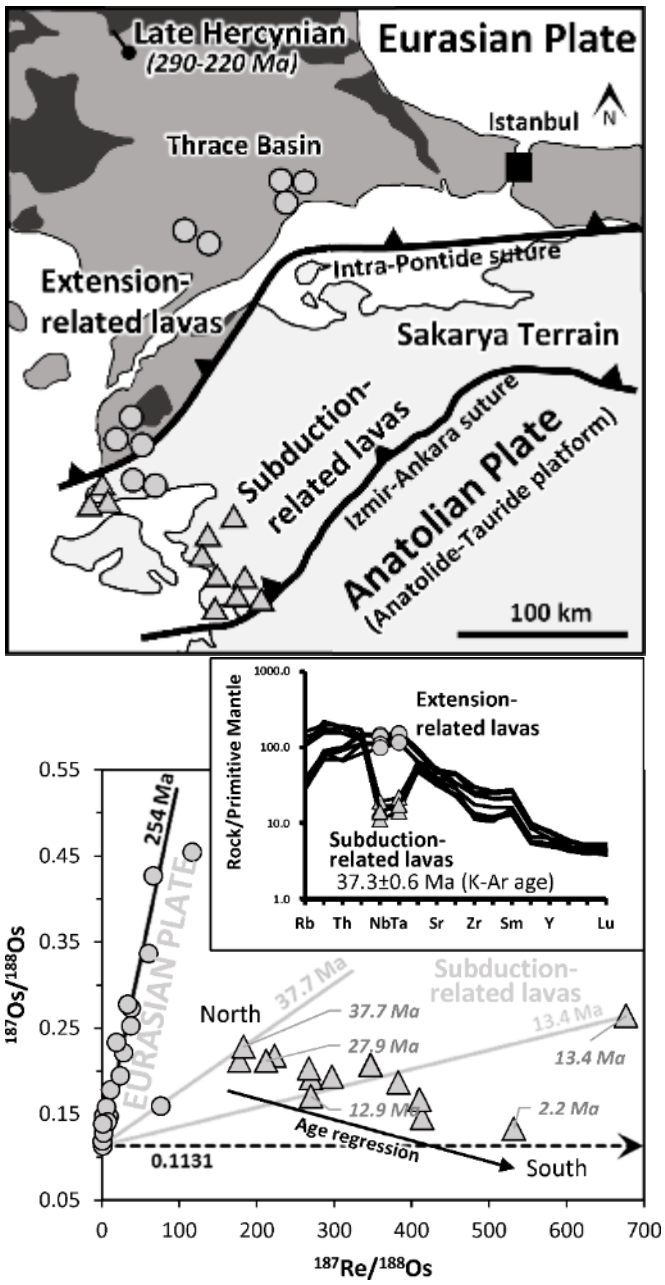

Figure 3.9 The $^{187}Os/^{188}Os$ and $^{187}Re/^{188}Os$ ratios of extension- and subduction-related lavas from NW Turkey. The sample locations, analyses, and ages are from Okay et al. (2001) and Aldanmaz et al. (2000, 2015).

CONCLUSIONS

Plate Tectonics has resulted in the opening and closing ancient oceans through the Earth's history and we observe evidence of the past amalgamations embodied by the suture zones and mountain belts. The compositional modification that the SCLM might gain through time can be inferred from the tectonically exhumed mantle assemblages in massifs and orogenic belts. For instance, the provenance of cumulate assemblages such as pyroxenites indicates secondary melt segregation in the SCLM associated with continental collisions. The postorogenic lavas are compositionally and isotopically in equilibrium with source lithology dominated by pyroxenites. The Os sampled by postorogenic lavas reveals isotopic growth trajectories chronologically synchronized with orogenies and crustal modifications (chapter 3). In addition, physical modifications gained during compressional tectonics might impose some constraints on the mantle's nature involved in the postorogenic lavas' petrogenesis. In chapter 1, for instance, the REE’s and trace elements systematics are spatially distinct amid the SVL, showing that input from an asthenospheric mantle is feasible in intracontinental settings.

The isochronous relations measured in the SCLM primary lithologies could be owed to the provenance of the SCLM as an oceanic convective mantle (peridotites, chapter 2). Although the isochron forming and non-forming assemblages are subchondritic or depleted in the present (Time =0), the isochrons' initial ratios show that the assemblages are primitive at the time of continental collisions. Within the precision of the data, thus, the melt removal and depletion are instantaneous. These are the attributes of a mantle in a constant upwelling and melt removal. At the present, such mantle exists at the Earth’s spreading centers. Physical separation from convection and accretion onto

non-convective mantle (SCLM) is consistent with opening and closing oceans as a continental amalgamation/break-up mechanism.

APPENDIX-A

Analyses of Re and Os were performed on new eight basaltic samples collected from discrete lava fields from the Sahara, North Africa. The results are shown in the following table:

Sample	Locality	Type	Age (Ma)	MgO (wt.%)	Os (ppb)	$^{187}Os/^{188}Os_{(m)}$	$^{187}Os/^{188}Os_{(i)}$	Re (ppb)	$^{187}Re/^{188}Os$	Re (ppb)
A28	Gharyan	Tholeiite	55	9.11	0.10138±55	0.16476±83	0.15753	0.16401±106	7.8859	0.16401
A27	Gharyan	Tholeiite	55	6.83	0.05791±52	0.17041±54	0.16644	0.05063±106	4.3222	0.05063
B26	Gharyan	Alkaline	11	9.66	0.05865±56	0.15545±49	0.15358	0.12220±124	10.1701	0.12220
C31	Gharyan	Tholeiite	5	5.61	0.02961±55	0.22790±147	0.22727	0.04477±147	10.2616	0.04477
C31†					0.02037±54	0.23010±167	0.22426	0.13201±107	31.9068	0.13201
A30	Gharyan	Tholeiite	5	6.04	0.03211±57	0.20395±90	0.20109	0.10201±114	15.6376	0.10201
JS-1A	As Sawda	Alkaline	10	10.28	0.01632±58	0.14294±267	0.13963	0.05990±113	18.0774	0.05990
JS-1A*					0.02482±52	0.15124±142	0.14967	0.04282±124	8.5463	0.04282
AH-15	Waw Namus	Alkaline	5	12.41	0.11193±64	0.15546±53	0.15486	0.16669±124	7.2575	0.16669
AH-16	Waw Namus	Alkaline	5	13.19	0.07512±58	0.12615±23	0.12452	0.30300±113	19.5072	0.30300

† Full procedural repeat. * Duplicates. m: measured, i: initial.

The volcanic fields, namely Gharyan (A28, A27, B26, C31, and A30), As Sawda (JS-1A and JS-1), and Waw Namus (AH-15 and AH-16), are episodic outpourings of basaltic lavas in the Cenozoic time. They are confined to an NW-SE trend (N140°E) that stretches from the Mediterranean coast in the north to Tibesti (Libya-Chad border). Major and trace elements of the collected samples are discussed in CHAPTER 2.

The sample preparation and analytical procedures to measure Re and Os isotopes followed those detailed in Carlson et al. (1999) and were performed at the Department of Terrestrial Magnetism (DTM), Washington DC. The sample preparation procedure included Carius tube digestions of approximately 2 g of the basalt powders, respectively, using ^{185}Re-^{190}Os spikes with $^{185}Re/^{190}Os = 6$ for the lavas. The digestions were followed by Os extraction and Re purification on anion exchange columns. Osmium was loaded onto Pt filaments with $Ba(NO_3)_2$ as an activator and analyzed as negative ions using a

Thermo-Fisher Triton thermal ionization mass spectrometer (TIMS). Re fractions were analyzed using a Nu-Plasma ICP- mass spectrometer.

All runs were corrected for their oxide compositions and mass fractionation using the $^{192}Os/^{188}Os$ ratio of 3.083. As part of the analysis and between each sample batch, runs from the in-house Os isotope reference material "J-M Os" yielded $^{187}Os/^{188}Os$ ratio 0.17383 ± 0.0002 (2σ std. dev., n=4). This value characterizes the sample analysis's external precision within 0.9 ‰ of the recommended value (0.17399). In-run precision for $^{187}Re/^{185}Re$ was better than 0.2%. Correction for blank Os contribution in the lavas, because the bulk Os concentration is low, the average proportion of blank Os was 2.55%, ranging from 1.03 to 6.65%. Re concentrations were corrected using a Re blank of 2 pg. The average proportions of Re in the blank to Re in the basaltic lavas were 1.27%.

Reference:

Carlson, R.W., Pearson, D.G., Boyd, F.R., Shirey, S.B., Irvine, G., Menzies, A.H., Gurney, J.J., 1999. Re–Os systematics of lithospheric peridotites: implications for lithosphere formation and preservation, in: Proceedings of the 7th International Kimberlite Conference. Red Roof Design Cape Town, pp. 99–108.

APPENDIX-B

The pyroxenite-Os hyperbola

The $^{187}Os/^{188}Os$ ratios and Os concentrations of pyroxenite-forming silicates and sulfides used in the example shown in Figure 3.7a are presented in the following table:

	A	B	C	D
$^{187}Os/^{188}Os$	7.5	7.5	7.5	0.13
Os (ppb)	10^3	10^2	10^{-3}	10^3

Using equations that relate the isotope composition to its concentration in a two-component mixture by Faure (1977), the $Os_{mixture}$ is a mix in varying proportions from 0 to 1 (f), defined as the weight or volume ratio:

$$Os_{mixture} = Os_{silicates}(f) + Os_{sulfides}(1-f) \quad \text{(Eq. A1)}$$

The $(^{187}Os/^{188}Os)_{mixture}$ for each $Os_{mixture}$ (f = 0 to 1) is a straight-line equation obtained from:

$$(^{187}Os/^{188}Os)_{mixture} = a\,(1/Os_{mixture}) + b \quad \text{(Eq. A2)}$$

where the parameters a and b are:

$$a = \frac{Os_{silicates} Os_{sulfides}\left[(^{187}Os/^{188}Os)_{sulfides} - (^{187}Os/^{188}Os)_{silicates}\right]}{Os_{silicates} - Os_{sulfides}} \quad \text{(Eq. A3)}$$

$$b = \frac{Os_{silicates}(^{187}Os/^{188}Os)_{silicates} - Os_{sulfides}(^{187}Os/^{188}Os)_{sulfides}}{Os_{silicates} - Os_{sulfides}} \quad \text{(Eq. A4)}$$

Reference:

Faure, G 1977, Principles of isotope geology, Smith and Wyllie intermediate geology series, Wiley.

VITA

Ashraf Gafeer received Master of Arts in Geology at University of Garyounis, August 2007 and Thesis title: “Geochemistry of Gharyan volcanic field, NW Libya.” Before he received Bachelor of Arts (May 2004) in Geology, University of Garyounis, Benghazi, Libya.

Ashraf worked as a Graduate Teaching Assistant, Department of Geological Sciences, University of Missouri in the academic year 2016-2017. Also, as part of his academic employment, he worked as Research Assistant, Department of Earth Sciences, University of Garyounis during the years 2007-20010.